

Doctoral School in Environmental Engineering

Hydrological controls on the triggering of shallow landslides: from local to landscape scale

Cristiano Lanni



UNIVERSITÀ DEGLI STUDI DI TRENTO

Dipartimento di Ingegneria Civile
e Ambientale

2012

Doctoral thesis in Environmental Engineering, XXIV cycle

Faculty of Engineering, University of Trento

Academic year 2011/2012

Supervisors: **Riccardo Rigon, University of Trento**

Jeffrey J. McDonnell, Oregon State University

University of Trento

Trento, Italy

February 2012

This thesis is dedicated to my mother, who taught me that even the largest task can be accomplished if it is done one step at a time.

It is also dedicated to my father, who taught me that the best kind of knowledge is that which is learned to be put into practice.

Acknowledgements

This research would not have been possible without the support of many people.

Above all, I wish to express my gratitude to my supervisors, Prof. Riccardo Rigon and Prof. Jeff McDonnell. They gave me the opportunity to study hydrology from two different and complementary perspectives, namely, experiment and modelling. Thanks Riccardo and thanks Jeff, especially because you have endured my stubbornness. I am aware...

I am particularly grateful to Prof. Stuart Lane for his precious suggestions that helped me to create a solid framework for this Thesis.

I wish to thank Prof. Tim Burt, Prof. Marco Borga, Dr. Jonathan Godt, Prof. Greg Hancock, Dr. Luisa Hopp, Dr. Mark Reid, Prof. John Selker, Prof. Jan Seibert, and Prof. Alessandro Tarantino for their helpful discussions along the way.

I am also grateful to Emanuele Cordano, Davide Giacomelli, Luke Pangle, and Jurriaan Spaaks for sharing some of their expert knowledge with me.

I am deeply and forever indebted to my parents for their support throughout my entire life.

I am grateful for time spent with friends (Daniele, Miriam, Alessia, Alfio, Cristian, Guglielmo, Laura, Marco), and for our memorable trips into the mountains. I would also like to acknowledge Jeff B., Lori, and Falah that helped me to have good times in Oregon.

Last but not least, I wish to thank Ilaria (pl) for always being ready to help me when I was in need. This work would not have been possible without her special support. 1221

Contents

1. Introduction	1
1.1 General introduction and problem statement	1
1.2 Motivation and Thesis objectives	4
1.3 Thesis outline	7
2. Literature review	9
2.1 Introduction	9
2.2 General landslide features	9
2.3 Water-induced shallow landslide processes	10
2.3.1 Rainfall infiltration in saturated/unsaturated soil	12
2.3.2 Shear strength and infinite slope stability model of saturated/unsaturated soil	15
2.4 Modelling shallow landslide occurrence at the catchment scale	19
2.4.1 Statistical approach	19
2.4.2 Physically-based models	20
2.5 Digital terrain modeling in hydrology: capabilities and limitation	23
2.6 Hydrological connectivity: Concepts and modeling	26
2.7 Summary of literature review	29
3. A smoothed dynamic topographic index to describe the relative role of upslope and downslope topography on water flow paths and storage dynamics	31
3.1 Introduction	31
3.2 Materials and methods	32
3.2.1 Study Site	32
3.2.2 The 2-dimensional Boussinesq (BEq) model	33
3.2.3 The setting of the terrain-based indices	34
3.2.4 Performance Criteria	39
3.3 Results	41
3.3.1 The role of the diffusive term	41
3.3.2 The performance of the terrain indices	43
3.3.2.1 Binary maps analysis (APPROACH I)	43
3.3.2.2 Spearman Rank analysis (APPROACH II)	46
3.3.2.4 Connectivity analysis	47

3.4	Discussion	49
3.4.1	On the relative role of upslope and downslope topography for describing water flowpath, connectivity and storage dynamics	49
3.4.2	On the need for hydrological smearing	49
3.5	Concluding remarks	52
4.	Simulated effect of soil depth and bedrock topography on near-surface hydrologic response and shallow landslide triggering	55
4.1	Introduction	55
4.2	The Panola trench hillslope	56
4.3	Methods	57
4.3.1	The hydrological response model and the hillslope stability model	57
4.3.2	Hydrological and mechanical characterization	60
4.3.3	Virtual experiment design	61
4.4	Results	63
4.4.1	The role of bedrock topography on pore pressure development and integrated hydrological response	63
4.4.2	Relation between hillslope gradient and spatio-temporal extent of transient saturation at the soil-bedrock interface	64
4.4.3	When does slope angle affect the dynamics of subsurface flow and pore pressure development?	66
4.4.4	Linking subsurface hydrology and landslide triggering	68
4.5	Discussion	70
4.5.1	On the relation between bedrock topography and the development of positive pore pressure	71
4.5.2	On the interaction of subsurface topography, hillslope hydrology and landslide triggering	72
4.5.3	Issues in modeling slope stability	74
4.5.4	Implications for catchment-scale shallow landslide models	76
4.6	Conclusions	76
5.	Modelling catchment-scale shallow landslide occurrence by means of a subsurface flow path connectivity index	79
5.1	Introduction	79
5.2	Materials and methods	80
5.2.1	The hydrological model	80

5.2.2	The coupled hydrological-slope stability model	85
5.2.3	Intensity-Duration-Frequency relationship for extreme rainfall events	86
5.2.4	Study sites and model application	87
5.3	Results and discussion	90
5.3.1	Assessment of shallow landslide susceptibility	91
5.3.2	Derivation of local rainfall thresholds for shallow landslide initiation	92
5.4	Summary and Conclusions	93
Appendix 5.A:	Simplified unsaturated vertical infiltration model vs one-dimensional Richards' equation solver	94
Appendix 5B:	Computation of the connectivity time as a time of subsurface hydrological connectivity	95
6.	Conclusions and Future directions	97
6.1	Conclusions and future directions	97
6.2	Final considerations	100
 <i>APPENDIX: A combined laboratory and numerical study to assess the role of hillslope boundary conditions on pore-water pressure dynamics</i>		 103
A.1	<i>Introduction</i>	103
A.2	<i>Material and methods</i>	104
A.2.1	<i>Little Panola: the experimental laboratory hillslope</i>	104
A.2.2	<i>Laboratory instrumentation and data collection</i>	106
A.2.3	<i>Set-up of Experiments</i>	107
A.3	<i>Results</i>	109
A.3.1	<i>Laboratory results</i>	109
A.3.2	<i>Virtual experiments</i>	111
	A.3.2.1 <i>Base case scenario</i>	112
	A.3.2.2 <i>Variation of boundary conditions</i>	114
A.4	<i>Discussion</i>	116
A.5	<i>Conclusions</i>	117
Bibliography		119

List of Figures

- 1.1 Number of fatalities (left) and cost of damage (right) caused by landslides 1903 to 2004. Source: EM-DAT – The OFDA/CRED International Disaster database
- 1.2 Landslide triggers in Italy. (Source: CNR-GNDCI AVI Database of areas affected by landslides and floods in Italy)
- 2.1 Shallow landslide schematic representation. Taken from Sidle and Ochiai, 2006
- 2.2 Shallow landslide within the context of landslide risk
- 2.3 Typical soil-water retention curve showing approximate locations of residual water content θ_r , saturated water content θ_s , and air entry value ψ_b
- 2.4 Shear strength surface in space of net normal stress, suction stress, and shear stress
- 2.5 Projection of shear strength surface shown in Fig. 2.3 on shear stress-net normal stress plane.
- 2.6 Schematic representation of the force balance on a rigid block on an inclined plane
- 2.7 Sketch of an elementary drainage area: (top) planar view and (bottom) longitudinal section
- 2.8 Diagrams of the development of soil moisture patterns (top 30 cm) showing the different degrees of connectivity between February (dry state) and September (wet state) 1996 at the Tarrawarra catchment. Contours show surface topography at 1 m intervals
- 2.9 Map of the location of above median soil moisture (blue, a) and subsurface saturation (green, b) for 5 storms in 2002 at the Panola hillslope Georgia, USA, identifying the disparity between subsurface saturation and surface soil moisture. Yellow dots in (a) represent soil moisture measurement locations; red dots in (b) show the positions of maximum rise wells for water table detection. Taken from Tromp Van Meerveld and McDonnell (2005)
- 3.1 Maps of topographic drainage directions (a), local slope $\tan\beta$ (b), and upslope contributing area A (c) of the Salei catchment. The upslope contributing area is mapped as the natural logarithm of the area in m^2
- 3.2 An example of time-variable upslope contributing area. Regardless of their steady-state upslope contributing area A, during a rainfall event the effective (time-variable) upslope contributing area, $A_f(t)$, of a point f located upslope may be larger than the effective (time-variable) upslope contributing area, $A_b(t)$, of a point b located downslope along the same flow path
- 3.3 Value of DWI for a point i and three values of d (2, 5, 10m). The numbers inside cells are elevations (expressed in meters), arrows represent topographic drainage directions, and dl

- (2m) is the DEM resolution
- 3.4 The direction of BEq-derived water table gradient $\nabla(z_b+h)$ against the direction of the topographic surface gradient $\nabla(z_b)$. Directions are coded with numbers ranging from 1 (east direction) to 8 (south-east direction), going counterclockwise. The percentages in the left and bottom inside margins of the plots represent the percentage of points characterized by a given value of water table drainage direction and topographic surface drainage direction, respectively
- 3.5 2-dimensional transect of Salei catchment and simulated water-table level by BEq model. The red line in panel (a) shows the position of the transect reported in panel (b). Low water storage deficit is observed near topographic hollows at the foot slope and where the irregular downslope topography prevents the free water drainage
- 3.6 Spatial patterns of the traditional “non dispersive” topographic index TWI (a), dynamic topographic index TWI_d (b), traditional “dispersive” topographic index TWI^{mf} (c), smoothed dynamic topographic index TWI_d^* (d), and BEq-derived water table levels (e). The maps show in gray the points lower than the 75th percentile and in black the points higher than the 75th percentile of the individual cumulative distribution functions
- 3.7 On the left, temporal evolution of Spearman’s rank correlation coefficient ρ between simulated water table level and traditional non-dispersive topographic index, TWI (blue), dynamic topographic index, TWI_d (red), smoothed dynamic topographic index, TWI_d^* (black), and dynamic index where the DWI is used to describe the local drainage, TWI^{DWI}_d (green). On the right, the role played by the low-pass filter on the terrain indices performance
- 3.8 Bar plots showing the ability of the different terrain indices to reproduce connected “wetter” areas. The rightmost bars-block represent the number of isolated “wetter” clusters provided by the five (TWI , TWI^* , TWI^{mf} , TWI_d , TWI_d^*) terrain indices (bars) and the BEq model (dashed line). The first, second, third and fourth bars-blocks represent the 1st quantile, 2nd quantile, mean, and 3rd quantile values of the individual cumulative distribution functions of the “wetter” cluster sizes
- 3.9 Conceptual representation of the threshold effect on the value of upslope contributing area at the hillslope/channel transition of digitized watersheds. The point inside the topographic hollow shows a value of upslope contributing area A much higher than a point located one pixel upslope
- 4.1 Irregular bedrock surface vs regular ground surface at the Panola hillslope (a), and soil depth variability (b)
- 4.2 Flow chart of the cellular automata model. The stress is propagated until no new unstable locations are generated. The final FS configuration gives an estimation of the most likely hillslope portion to be affected by landslide activation
- 4.3 Patterns of transient saturation at the soil-bedrock interface of the original 13° Panola

hillslope for distinct time steps in the hillslope hydrograph (shaded right-hand side of the figure) for several hours during the *long-rainfall* event. The blue zones represent the patches of transient saturation (perched water table), the yellow, grey and brown colors identify variably unsaturated soil conditions. Flow is concentrated in the mid-slope which exhibits the highest pore pressure values

- 4.4 Maps of pore pressure at the soil bedrock interface of the original 13° Panola hillslope (first row), and the modified 20° and 30° Panola hillslopes (second and third rows, respectively) for the long-rainfall event. Maps of pore-pressure are quite similar during the first stage of rainfall (the maps of 1st hour and 4th hour are showed in the first and second columns, respectively), while the overall inclination significantly affects the dynamic of pore pressure in the second stage of rainfall (the maps of 9th hour and 10th hour are showed in the third and fourth columns, respectively) when lateral flow becomes relevant
- 4.5 Saturated area and pressure head response for the *long-rainfall* event. (a) Temporal evolution of saturated area at the soil-bedrock interface of the original 13° and modified 20° and 30° Panola hillslopes during the *long-rainfall* event. (b) Dynamics of the mean value of positive pressure head versus percentage of saturated area at the soil-bedrock interface for the three analyzed Panola hillslope angles. (c) Temporal evolution of the variance σ_{ψ}^2 of the values of pressure head recorded at the soil-bedrock interface for the three slope angles investigated
- 4.6 Maps of pore-pressure at the soil-bedrock interface of the modified 30°-Panola hillslope during the *short-rainfall* (top) and *long-rainfall* (bottom) events. Patterns of pore pressure are similar when the same value of cumulative rainfall has been achieved
- 4.7 Temporal patterns of unstable locations generated by the cellular automaton (CA) model for four different values of λ (0.2, 0.4, 0.6, and 0.8 on the first, second, third and fourth row, respectively). The *long-rainfall* event case (I=6.25 mm/h, D=9h) is here shown. In red are the points classified unstable by the infinite slope stability model (Equation 4.5). The black points are the ones that become unstable when the driving forces of the destabilized locations are redistributed to the neighboring cells (Equation 4.6). Rapid failure propagation is observed for high values of λ ($\lambda=0.6$ and $\lambda=0.8$) during the second stage of rainfall event (i.e., after 5 hours from rainfall beginning)
- 4.8 Cumulative rainfall against % of unstable area provided by the CA model for all the rainfall events analyzed. Instability spread very quickly when a cumulative rainfall of 30-35 mm was exceeded
- 4.9 A comparison between the hydrological behavior of the “irregular” Panola hillslope and a “regular” planar hillslope. Both slopes received an input of 6.25 mmh⁻¹ over 9 hours. Panels (a) and (c) show the pressure head lines (at the 9th rainfall-hour) at the soil-bedrock interface of the irregular and regular slopes, respectively. A saturated wedge expands

- upslope from the hillslope toe in the planar case (d). Roughness at the bedrock topography of the Panola hillslope (b) induce localized increase in pressure head (by preventing the free downslope drainage) resulting in complex patterns of instability (Figure 4.7). The vertical dimensions in panels (b) and (d) are exaggerated differently
- 5.1 A flow chart depicting the coupled saturated/unsaturated hydrological model developed in this Chapter
- 5.2 The concept of hydrological connectivity. Lateral subsurface flow occurs at point (x,y) when this becomes hydrologically connected with its own upslope contributing area $A(x,y)$ (b)
- 5.3 $\theta_i(z)$ and $\psi_i(z)$ are, respectively, the initial water content and the initial suction head vertical profiles. $\theta_{wt}(z)$ and $\psi_{wt}(z)$ represents the linear water content and suction head vertical profiles associated with zero-suction head at the soil-bedrock interface
- 5.4 Catchments case study. The map shows the location of the three catchments, and the landslide distribution (polygons inside the catchments)
- 5.5 Patterns of Return period T_R (years) of the critical rainfalls for shallow landslide triggering (i.e., $FS \leq 1$) and associated levels of landslide susceptibility
- 5.6 Modelled local rainfall intensity-duration (I-dc) thresholds for shallow landslide initiation at the three investigated catchments, and experimental I-d that triggered debris flow in some alpine catchments (of the Dolomities) similar to our study area
- 5.A1 The balls in the three dimensional space represent the differences between t_{wt} computed with HYDRUS-1D and t_{wt} computed with the simplified infiltration model (presented in Section 5.2.1) for 50 scenarios obtained by combining different values of soil thickness, rainfall intensity, and initial pore pressure profile
- A.1 (a) The geometry of the real Panola hillslope, (b) the topography of Little Panola, and (c) the 11:1 scale model of the Panola hillslope
- A.2 The rainfall simulator mounted on Little Panola (a). Two independent rainfall systems (b) allowed to reproduce a 22 mmh^{-1} and a 47 mmh^{-1} constant rainfall intensity event
- A.3 Location of pore-water pressure transducers at the “soil/bedrock interface” of Little Panola
- A.4 Bedrock topography at different slope inclination on a representative upslope transect across the hillslope (left). Map of contributing area based on bedrock topography for the three slope angle analyzed (right)
- A.5 Experimental pore-water pressure measurements at the soil-bedrock interface of the 6° -configuration of Little Panola
- A.6 Experimental pore-water pressure measurements at the soil-bedrock interface of the 23° -configuration of Little Panola
- A.7 Temporal evolution of experimental versus simulated values of pore-water pressure at different points. Pore-water pressures are measured at the soil/bedrock interface of Little

Panola

- A.8 Experimental and simulated values of pore-water pressure at different locations and at different times from the onset of rainfall along the transect A-A'. Pore-water pressures are measured at the soil/bedrock interface
- A.9 Numerical experiments exploring the effect of the downslope boundary condition and the shape of the subsurface topography on pore-water pressure dynamics at the soil/bedrock interface of Little Panola
- A.10 Effect of a free-face at the footslope in distorting unsaturated downslope flow (a and b). Influence of depressions in the bedrock surface (c), and the backwater effect at the bank of a stream (d)

List of Tables

- 2.1 Landslide classification (Varnes, 1978)
- 2.2 A list of the major efforts of the last 30 years to produce more realistic terrain indices from digital elevation models
- 3.1 The six terrain-based indices defined in this study and their major features
- 3.2 An overview of the applied similarity coefficients (Approach I) and their theoretical range. The case of the traditional dispersive TWI index is here reported
- 3.3 Similarity coefficients between reclassified binary maps of wetness indices (TWI, TWI^{mf}, TWI_d, TWI_d^{*}) and simulated water table depth (or storage deficit) by BEq model with $z_k=75$ th percentile of the individual cumulative distribution functions. Values in bold represent the best index at a given rainfall-hour
- 3.4 Similarity coefficients between reclassified binary maps of wetness indices (TWI, TWI^{mf}, TWI_d, TWI_d^{*}) and simulated water table depth (or storage deficit) by BEq model with $z_k=25$ th percentile of the individual cumulative distribution functions. Values in bold represent the best index at a given rainfall-hour
- 4.1 Average soil thickness $\overline{\Delta z}$ and hydrological parameters of the soil and saprolite bedrock layers of Panola Hillslope (from Hopp and McDonnell, 2009)
- 4.2 The hillslope angles and rainfall event features used in the virtual experiments. I = rainfall intensity; D = rainfall duration.
- 5.1 Hydraulic and mechanical soil-parameters relative to the three investigated catchments
- 5.2 Percentages of slope-stability categories in terms of catchment area and observed landslide area in each range of critical rainfall frequency (i.e., return period TR) or level of shallow landslide susceptibility
- A.1 Physical and hydrological parameters of the sandy soil used in Little Panola
- A.2 Laboratory experimental conditions

Abstract

This research tries to fill a gap between two very different scales of enquiry: the *local* (i.e. hillslope) scale, where detailed investigations are possible but difficult to generalize over large areas, and the *landscape* (i.e., catchment) scale, where representation of the physics is minimised, the resolution in space and time is maximised, and the focus is upon predicting emergent properties rather than system details. Specifically, this Thesis focused on an aspect of the geosciences that is of critical current concern: the representation of the interface between hydrological response and geomorphic processes, notable mass movements. At present there remains a great difficulty at this interface: detailed geotechnical and hydrological studies of mass movements reveal exceptionally complex interlinkages between water and the surface sediment mass, notably dynamically at the onset and during mass release; but these kinds of studies are only possible with a very detailed description of the three-dimensional structure of the porous media and its hydrological and mechanical response during (and after) rainfall events. Such analyses are feasible but tend to result in analyses that are restricted in terms of geographical generalisation. On the other hand, approaches that apply to larger spatial scales tend to over-simplify the representation of critical failure processes, such as in the assumptions that infinite slope stability analysis can be applied to failures that are finite in their slope length, or that upslope contributing area can always act as a surrogate for the hydrologic response at a point in the watershed.

The innovative element in this research lies on the assessment of rainfall-induced shallow landslide occurrence over large spatial scales, whilst accepting that shallow landslides triggering may be influenced by processes that operate over much smaller scales. Specifically, this Thesis focuses upon connection by subsurface flow pathways. New model approaches that incorporate connectivity are required to address the findings of field hydrologists. Thus, this Thesis starts from the understanding of small-scale hydrological processes to develop a large-scale topographic index-based shallow landslide model that includes the concept of subsurface hydrological connectivity.

The research aims to provide a tool for more realistic assessments of when shallow landslides may occur and where landsliding may occur at the catchment scale to support decision makers in developing more accurate land-use maps and landslide hazard mitigation plans and procedures.

Chapter 1

Introduction

1.1 General introduction and problem statement

Landslides represent a major threat to human life, property and constructed facilities, infrastructure and natural environment in most mountainous and hilly regions of the world. A landslide is defined as "the movement of a mass of rock, debris, or earth down a slope" (Cruden, 1991). Failure of a slope occurs when the force that is pulling the slope downward (gravity) exceeds the strength of the earth materials that compose the slope. Landslides can move slowly (millimeters per year), or can move quickly and disastrously, as is the case with shallow landslides.

The term shallow landslide is used to describe movements by which material is displaced over a discrete slip surface close to the land surface. Shallow landslides are particularly important in terms of natural hazard, as they often translate into rapidly moving debris flows (Iverson et al., 1997) that may affect human life and properties (Olshansky, 1990; Schuster, 1996; Sidle and Ochiai, 2006; Keefer and Larsen, 2007).

In the last century, Europe has experienced the second highest number of fatalities and the highest economic losses caused by landslides compared to other continents (Figure 1.1): **16,000 people have lost their lives** because of landslides and the material losses amounted to over \$1700 million in Europe during the 20th century.

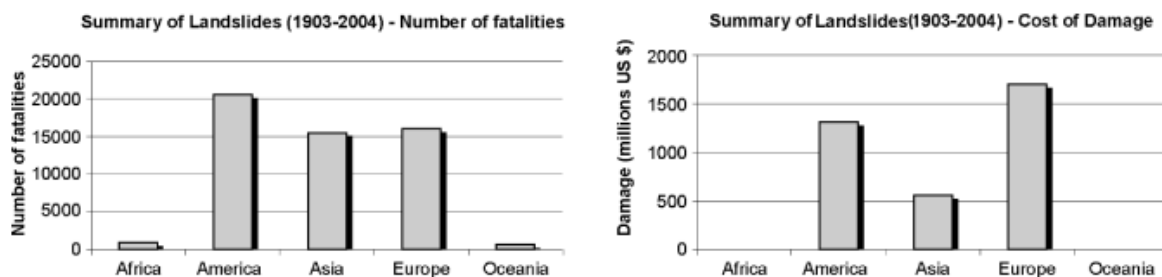


Figure 1.1. Number of fatalities (left) and cost of damage (right) caused by landslides 1903 to 2004. Source: EM-DAT – The OFDA/CRED International Disaster database.

Within Europe, Italy has been the country that has suffered the greatest human and economic losses due to landslides. In Italy, while about **500 people have been killed by landslides** over the past 25 years, the total number of persons impacted is 50 times that number.

Shallow landslides may be triggered by different factors, either natural or related to human activities. Among natural factors, rainfall is certainly one of the most frequent causes of landslides occurrence. Intense storms with high-intensity, long-duration rainfall have great potential to trigger rapidly moving landslides and have been documented as one of the major cause for shallow landslide triggering (Anderson and Sitar 1995; Iverson et al. 1997; Montgomery and Dietrich, 1994; Van Asch et al., 1996; Terlien, 1998; Ng and Shi, 1998; Iverson, 2000; Sidle and Onda, 2004; Malet et al., 2005). Significant examples are provided by multiple shallow phenomena periodically occurring in New Zealand (Crozier, 2005), Washington (Baum et al., 2005), California (Godt et al., 2008), Brazil (Ahrendt and Zuquette, 2003), Japan (Matsushi et al., 2006), Italy (Del Prete et al., 1998). In Italy, about 70% of landslides are triggered by precipitation and rainfall infiltration in a mantle of colluvial soils (Figure 2.1).

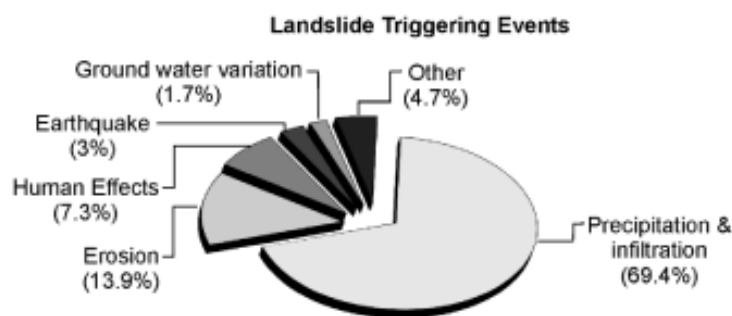


Figure 1.2. Landslide triggers in Italy. (Source: CNR-GNDCI AVI Database of areas affected by landslides and floods in Italy)

Rainfall infiltration reduces the soil-shear strength by decreasing the positive effect on stability due to negative pore pressure (Bishop, 1959; de Campos et al., 1994; Godt et al., 2009) or by increasing the positive pore pressure values (e.g., Terzaghi, 1943). The failure surfaces may form within the weathered material (e.g., Lu and Godt 2008; Hawke and McConchie, 2009), but often correspond to the point of contact between the soil and the less permeable bedrock, where a temporary perched water table could develop (e.g., Dietrich et al., 2007; Baum et al., 2010).

In the literature, two approaches have been proposed to evaluate the dependence of landslide occurrence on rainfall events. The first approach is based on the definition of empirical intensity-duration thresholds for landslide activation (Caine, 1980; Reichenbach et al., 1998; Corominas, 2000; Aleotti, 2004; Berti and Simoni 2005; Wiczorek and Glade, 2005;

Guzzetti et al., 2008). An empirical threshold defines the rainfall, soil moisture, or hydrological conditions that, when reached or exceeded, are likely to trigger landslides (Reichenbach et al., 1998). Rainfall intensity-duration thresholds for the possible occurrence of landslides are defined through the statistical analysis of past rainfall events that have resulted in slope failures, and can be classified based on the geographical extent for which they are determined (i.e., global, national, regional, or local thresholds), and the type of rainfall information used to establish the threshold (Guzzetti et al., 2007, 2008).

The second approach to evaluate the dependence of landslide occurrence on rainfall events relies on the use of mathematical models based on physical laws to understand the physical processes controlling slope instability (Montgomery and Dietrich, 1994; Wilson and Wieckzorek, 1995; Wu and Sidle, 1995; Iverson, 2000; Borga et al., 2002; Crosta and Frattini, 2003; Simoni et al. 2008). The mathematical models employed span a broad spectrum from relatively simple “pipe and pot” models to parsimonious topographic-index based models to complex, three-dimensional (3D), variably-saturated flow models based on Richards’ equation.

Process-based models rely upon the understanding of the physical laws controlling slope instability. 3D finite element Richards’ equation solvers provide a complete description of the pore pressure fields in saturated/unsaturated soil. However, the 3D Richards’ equation is highly non-linear and requires the solution of extremely large systems of equations even for small problems (Paniconi et al., 2003). Moreover, the parameterization and calibration of these models is often cumbersome due to the small amount and low accuracy of the available data (Hilberts, 2006).

Topographic wetness index-based models have gained wide use to describe the hydrological control on the triggering of rainfall-induced shallow landslide for the assessment of landslide hazard at regional scale (Montgomery and Dietrich, 1994; Wu and Sidle, 1995; Borga et al., 2002; Iida, 1999; Rosso et al., 2006; Claessens et al., 2007; Casadei et al., 2003). SHALSTAB (Montgomery & Dietrich, 1994) is an example of such a models, where the water table thickness above the soil-bedrock interface is calculated from a steady-state mass balance and it is expressed as a function of the traditional topographic index TWI (O’Loughlin, 1986) given by the ratio between specific upslope contributing area A/b (i.e., upslope contributing area, A , per unit contour length, b) and local slope angle $\tan\beta$ ($TWI=A/b\cdot\tan\beta$).

Borga et al. (2002) relaxed the hydrological steady-state assumption in topographic index-based shallow landslide models by using a modified version of the quasi-dynamic wetness index developed by Barling et al. (1994). This allowed them to obtain information on the rainfall duration needed to cause slope instability under the assumption that lateral subsurface flow in the saturated zone (i.e., below the water table) occurs simultaneously at any point across the catchment (Grayson et al., 1997). Subsequently, several other models

(that will be widely discussed in Chapter 2) were added to the list of models capable of assessing landslide susceptibility over large areas.

1.2 Motivation and Thesis objectives

Despite the considerable progress in recent decades, catchment-scale shallow landslide models still consider runoff generation and contributing area variability as a continuum. The details of subsurface hydrological processes remain rudimentary in the numerical structure of most slope stability models and there are still many unanswered questions in the dynamics of pore-water pressure generation related to landslide initiation (e.g., Iverson et al., 2000). Almost all such models assume that the soil-bedrock interface is a simple topographic surface paralleling the soil surface. As a result, none of the slope stability models used to assess landslide susceptibility and hazard at the catchment scale have yet included an important new conceptual element derived from the hillslope hydrology literature: **the filling and spilling of water perched at the soil-bedrock interface**. Indeed the importance of moisture dynamics at the soil-bedrock interface has been widely acknowledged in hillslope hydrology (e.g., Weiler et al., 2005). Recent hydrological analyses by several groups in several different hydrogeological settings (e.g., Spence and Woo, 2003; Buttle et al., 2004) have shown that filling and spilling of microtopographic depressions in the bedrock topographic surface control the development and **connectivity** of patches of positive pore pressure, and that hydrological connectivity (the condition by which disparate regions on the hillslope are linked via subsurface water flow, Stieglitz et al. 2003) is a necessary condition for lateral subsurface flow to occur at a point (e.g., Tromp van Meerveld and McDonnell, 2006b, Graham et al., 2010; Spence, 2010).

For the hillslope hydrologist, these patches and their downslope connectivity, form the precondition for resultant subsurface stormflow (Tromp van Meerveld and McDonnell, 2006a). This behavior is now viewed as dominant subsurface stormflow delivery mechanism whereby the existence of a threshold relationship between rainfall amount and hillslope outflow appears to be a common property of hillslope drainage (see review in Weiler et al., 2005). For the slope stability modeler, these patches appear to be a key, unstudied part of the landslide initiation process with potential **first order hydrologic control on where a slip surface might be found**.

Lack of, or only intermittent, connectivity of subsurface flow systems invalidates the assumptions built into the TWI theory (i.e., the variable – and continuum - contributing area concept originally proposed by Hewlett and Hibbert, 1967). However, until now catchment-scale shallow landslide models have failed to include a connectivity component for subsurface flow paths.

Physically based, distributed models (e.g., GEOtop by Rigon et al., 2006 and Simoni et al., 2008) which solve for both the vertical and lateral flux of water across the landscape would

implicitly account for hydrological connectivity. However, these models are commonly applied at grid-resolution coarser than those that are likely to control connectivity and landslide occurrence (Lane et al., 2009). The reasons for such coarser resolution are twofold. Firstly, physically-based numerical models are exceptionally demanding in terms of parameterization (Merritt et al., 2003). The information demand for model calibration often exceed available data, and the models are rarely parsimonious with respect to the data available to determine them. The second reason lies on the computational difficulty of running such models with time steps that are small enough to capture the dynamics of shallow landsliding coupled to the need to understand the landsliding process over potentially large spatial extents. It is therefore required to make simplifying assumptions related to hydrologic response (Loague et al., 2006) in order to include a connectivity component in catchment-scale shallow landslide models.

This is what has been done by Lane et al. (2004) to represent surface hydrological connectivity. Lane et al. (2004) developed a network index as an index to describe the level of catchment-averaged saturation required for a saturated point in the hillslope to be hydrologically connected to the drainage network along the complete hydrological flow path that connects the point to the drainage network. The network index of a point is the lowest value of the topographic index along the flow path that connects it to the drainage network by surface overland flow. On its own, TWI does not describe connectivity, but Lane et al. (2004) argued that the spatial arrangement of TWI provide a measure for overland flow connectivity as locally deep water tables (from the ground surface) reduce the propensity to overland flow and increase the probability of water infiltration into the soil. Therefore, the network index treatment has two important hydrological effects: (a) it only allows saturated areas to connect to the hydrological network when there is full saturation along the associated flow path; and (2) overland flow associated with unconnected but saturated zones is assumed to remain within the catchment and to contribute to a reduction in the catchment-averaged saturation deficit.

By considering that connectivity of patches of transient saturation from a location to another on the hillslope depends upon the balance between processes that encourage lateral connection along a flow path and those that disconnect a flow path (e.g., bedrock depressions - Freer et al., 2002; Tromp van Meerveld and McDonnell, 2006a; Hopp and McDonnell, 2009 - and dry soil-moisture conditions - Western et al., 1999 and 2001), an approach similar to the one presented in Lane et al. (2004) should also be applicable to represent subsurface hydrological connectivity (Lanni et al. 2011).

This Thesis exactly deals with the interaction between hydrological processes, notably in terms of subsurface hydrological connectivity, and shallow landslide initiation.

In this sense, the research tries to fill a **gap between two very different spatial (and temporal) scales** of enquiry: the *local* (i.e. hillslope) scale and the *landscape* (i.e., catchment)

scale.

At the hillslope scale, detailed hydrological studies reveal exceptionally complex interlinkages between water and the surface sediment mass, notably dynamically at the onset and during mass movement; these kinds of studies are only possible with a very detailed description of the three-dimensional structure of the sediment mass and its hydrological response during events. Such analyses are feasible but tend to result in analyses that are restricted in terms of geographical generalization; at the *landscape* (i.e., catchment) scale, shallow landslide modeling tends to over-simplify the representation of hydrological processes by failing to include important controls (such as hydrological connectivity) on both pore-water pressure dynamics and, therefore, landslide triggering mechanisms.

Thus, the innovative element in this research lies on the assessment of subsurface hydrological connectivity over large spatial scales, potentially 10s or 100s of km², **whilst accepting that shallow landslide initiation and subsurface hydrological connectivity may be influenced by processes that operate over much smaller scales (≤ 10 m)**. The model aims to provide more realistic assessments of **when** shallow landslides may occur and **where** landsliding may occur at the catchment scale to **support decision makers in developing more accurate land-use maps and landslide hazard mitigation plans and procedures**. To achieve this aim, the three following interrelated objectives - that move from physical understanding, processes conceptualization, and model (re)formulation of near-surface flow dynamics and landslide triggering mechanisms – will be pursued by this Thesis:

Objective 1. Formulate a new topographic wetness index to include the relative role of upslope and downslope topography and (at least partially) overcome the limitations found in traditional topographic indices (i.e., the steady-state assumption for subsurface flow, and the hypothesis that subsurface hydraulic gradient is locally parallel to the gradient of surface topography).

Objective 2. Address the role played by bedrock topography on subsurface pore-water pressure dynamics and resulting hydrological connectivity. Specifically, it is tested the hypothesis that small-scale variability of soil depth and subsurface topography control the degree of drainage pathway connectivity. To meet the objective, the well characterized Panola hillslope hydrological research site (Freer et al., 2002) is used as a virtual laboratory to explore how soil depth, slope inclination and other factors conspire to trigger shallow landslides.

Objective 3. (Motivated by findings in the first two objectives) develop a catchment-scale topographic index-based shallow landslide model to include the concept of subsurface hydrological connectivity operating at the hillslope scale.

1.3 Thesis outline

Following this introductory chapter, this Thesis comprises of five more chapters dealing with the objectives mentioned above. In Chapter 2, a comprehensive literature review of shallow landslide processes is presented. It documents past research on hydrological processes leading to shallow landslides. The chapter covers various modeling approaches with particular emphasis on those used to assess shallow landslide occurrence at the catchment-scale. Moreover, Chapter 2 will introduce the concept of hydrological connectivity and its contribution to understanding runoff-dominated geomorphic systems.

Chapter 3 deals with Objective 1. It is shown that the new topographic wetness index is able to better reproduce spatial patterns of wetness areas as provided by a distributed, physically-based, Boussinesq Equation solver (BEq) than traditional topographic wetness indices.

Chapter 4 focuses on physical understanding of hydrological processes operating at the hillslope scale (Objective 2). The work builds upon the work of Hopp and McDonnell (2009) where they used the 3D Richards' equation solver, Hydrus 3-D (Simunek et al., 2006), to quantify patterns of pore pressure development and 3D flow in porous media. Moreover, a simplified cellular automata model is developed to simulate the spatial propagation of destabilized area after failure initiation.

Chapter 5 deals with Objective 3 presenting the new catchment-scale shallow landslide model. The model is applied to three catchments in the central Italian Alps for which a detailed landslides inventory is available.

In Chapter 6, a synthesis of the research is presented. The results obtained are summarized, and evaluated. Limitations of the methods are presented, together with suggestions for future model improvements and research needs.

Finally, an Appendix shows results of a combined laboratory and numerical study to assess the role of hillslope boundary conditions on pore-water pressure dynamics. This is an element of reflection about the limited capability of topographic-index shallow landslide models to deal with landslide mechanisms affected by hillslope boundary conditions.

Chapter 2

Literature review

2.1 Introduction

A broad understanding of various topics in hydrological and geotechnical science and modelling technology was required to complete the studies presented in this thesis and it is important to review each of them thoroughly. The first part of this Literature review (Sections 2.2 and 2.3) gives a brief description of water-induced shallow landslide processes. Particular attention is paid to transient infiltration into saturated/unsaturated soil, effective stress in unsaturated soils, shear strength of hillslope soils, and transient stability of infinite slopes. Subsequently, common approaches of modelling shallow landslides at the catchment scale are reviewed (Section 2.4).

The second part of this Chapter (Section 2.5 and 2.6) focuses on the use of digital terrain analysis in hydrological and shallow landslide modeling. Algorithms that have been developed to compute topographic indices are reviewed and discussed (Section 2.5). The concept of hydrological connectivity (i.e., the condition by which disparate regions on the hillslope are linked via subsurface water flow) is introduced in Section 2.6, and a recent attempt to include a connectivity component in topographic index-based hydrological models is also presented.

2.2 General landslide feature

The term landslide is generally used to denote a downslope movement of mass of earth, debris or rock down a slope due to the action of external forces such as rainfall, snowmelt, volcanic eruption, earthquakes, anthropogenic activities etc.

The most widely accepted landslide classification is by Varnes (Varnes, 1978 in Table 1.1). Any landslide is generally classified and described by two nouns: the first describes the materials (e.g. earth, debris or rock); and the second, the type of movement (e.g. falls, topples, slides, flows, spread etc.).

Table 2.1. Landslide classification (Varnes, 1978)

Type of movement	Type of material		
	Bedrock	Soil	
	Coarse	Fine	
Fall	Rock fall	Debris fall	Earth fall
Topple	Rock topple	Debris topple	Earth topple
Slide	Rock Slide	Debris slide	Earth Slide
		Rotational	
Spread	Rock spread	Debris spread	Earth spread
	Translational		Earth flow
Flow	Rock flow	Debris flow	Earth flow
Complex	Combination of two or more		

A landslide occurs when stresses acting on soil mass on a hillslope exceed the soil-shear strength. It has generally been recognized that these forces are functions of various parameters relating to bedrock geology, lithology, geotechnical properties, rainfall characteristics (intensity and duration), soil-moisture conditions, water table position, and land-use patterns. Additionally, in many cases human interferences are also responsible for triggering the landslides and create the same effects on a slope as a range of natural processes. Some of the common examples of human interferences leading to landslides are changes in land-cover, deforestation, cutting of slopes etc.

2.3 Water-induced shallow landslide processes

Landslides in which the sliding surface is located within the soil mantle or weathered bedrock (typically to a depth from a few decimeters to several meters) are categorized as shallow landslides. A schematic diagram of a shallow landslide is presented in Figure 2.1.

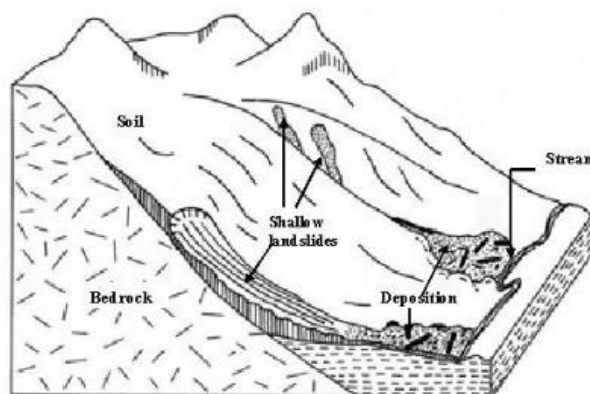


Figure 2.1. Shallow landslide schematic representation. Taken from Sidle and Ochiai, 2006.

Shallow landslides are often triggered by rainfall. Rainfall infiltration increases pore-water

pressures and therefore reduces the soil-shear strength. Analysis and prediction of stress conditions leading to landslides is largely grounded on Terzaghi's (1943) effective stress principle for saturated materials. This principle states that the controlling variable for the mechanical behavior of earth materials is effective stress, defined as the difference between total stress and positive pore water pressure. However, this definition may not be appropriate for assessing the state of stress in hillslopes nor completely describe shallow failure of hillside materials under partially saturated conditions since it neglects the effect of unsaturated soil conditions on the soil-shear strength (e.g., Rahardjo et al., 1995; Terlien, 1998; Van Asch et al., 1999; Hornbaker et al., 1997; Mitarai and Nori, 2006). Theoretical and analytical results from a variety of geologic and climatic settings have advanced the hypothesis of shallow slope failure in partially saturated materials (Morgenstern and de Matos, 1975; Wolle and Hachich, 1989; Rahardjo et al., 1996; Collins and Znidarcic, 2004). Godt et al. (2009) reported instrumental observations from a coastal bluff in the Seattle, WA area where a shallow landslide occurred in the apparent absence of positive pore water pressures under partially saturated soil conditions. When rainwater infiltrates through an unsaturated zone, the advancement of the wetted zone near the slope surface may lead to failure during periods of prolonged rainfall. If the effective cohesion of soil is zero ($c'=0$), and the slope angle (β) is greater than or equal to the effective internal friction angle of the soil (ϕ'), the unsaturated soil slope fails from a loss of apparent cohesion upon saturation of the soil by the infiltrating wetting front. In this case, failure from a reduction in the shear strength because of a rise in the ground water table or the occurrence of a perched water table is unlikely since the slope can only be stable with the shear strength due to the matric suction that fully disappears before saturation is achieved. However, if the slope angle does not exceed the effective friction angle of the soil, slopes are not susceptible to failure from the loss of matric suction since the slopes remain stable without the additional shear strength due to the matric suction; yet the slopes will fail from a reduction in the effective stress in the saturated condition that results in the reduction in the shear strength of soil. When a slope possess an effective cohesion component (c'), and the effective cohesion of the soil is adequate, even a partially saturated slope with a slope angle that is greater than the effective friction angle can remain stable in spite of a complete loss of apparent cohesion. However, even these types of slopes would fail in the saturated condition if an increase in pore pressure reduces the effective stress (Sudhakar, 1996).

Water plays a major role not only in the initiation of failure but also in the way that the earth then flows or slides and the distance that it travels. In many cases shallow landslides are fast-moving and are extremely destructive. Figure 2.2 illustrates many of the important factors culminating in the exposure of society to safety and economic consequence (road, urban area, landscape).

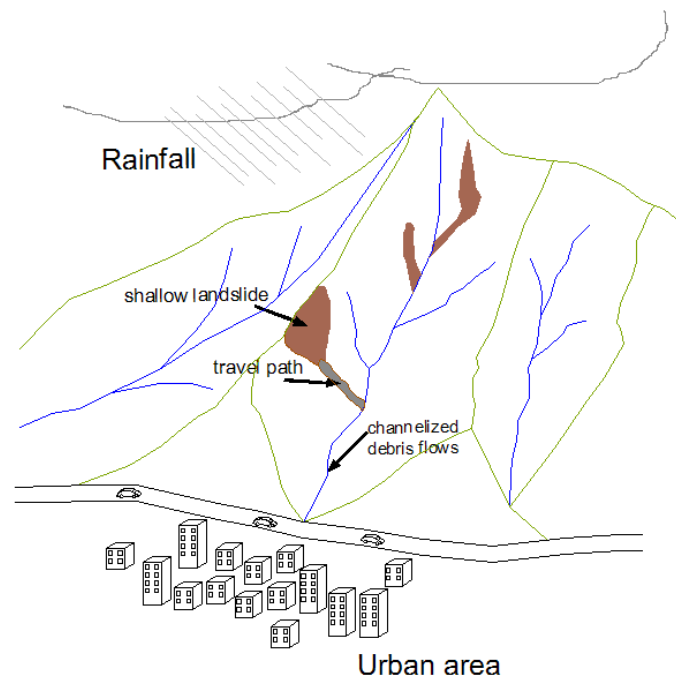


Figure 2.2. Shallow landslides within the context of Landslide Risk

The connectivity between upland landslides and stream channels is a very significant factor in the propagation and run-out potential of debris flows. For high magnitude events (i.e., exceptionally heavy rainfall events), debris stored upon hillslopes and within valley floors provides a source of generally unconsolidated sediment that can be entrained and mobilised by channelized debris flows. It follows that the accumulation of unconsolidated debris from numerous shallow landslides over time can provide a large volume of sediment capable of being mobilised in a single episodic channelized debris flow event. Thus, shallow landslides have high potential of causing damage and human losses due to the high velocities in the post-failure phase and the increase in the mobilized volumes during the downhill path. However, prediction of shallow landslide remains a difficult task due to uncertainties regarding hydro-mechanical properties and limited understanding of the underlying triggering mechanisms.

2.3.1 Rainfall infiltration in saturated/unsaturated soil

In the unsaturated zone, the fluid motion is assumed to obey the classical Richards equation (Richards, 1931). The water-mass balance equation for both unsaturated and saturated condition is:

$$-\rho \left(\frac{\partial q_x}{\partial x} + \frac{\partial q_y}{\partial y} + \frac{\partial q_z}{\partial z} \right) = \frac{\partial(\rho\theta)}{\partial t} \quad (2.1)$$

where ρ [FL^{-3}] is the density of water, q_x, q_y, q_z [LT^{-1}] are fluxes in the x, y, and z directions, respectively; t [T] is the time, and θ [L^3L^{-3}] is the volumetric water content. Darcy's law can be generalized to unsaturated fluid flow problems by considering hydraulic conductivity as a function of suction head (i.e., negative pressure head) (Buckingham, 1907):

$$q_x = -k_x(\psi) \frac{\partial H}{\partial x}; \quad q_y = -k_y(\psi) \frac{\partial H}{\partial y}; \quad q_z = -k_z(\psi) \frac{\partial H}{\partial z} \quad (2.2)$$

where ψ [L] is matric suction head, and $k(\psi)$ [LT^{-1}] is the unsaturated hydraulic conductivity function. In the absence of an osmotic pressure head, the total head H [L] in unsaturated soil is the sum of the matric suction head and the elevation head Z [L]: $H = \psi + Z$. Thus, substituting Eq. (2.2) into Eq. (2.1) with the hypothesis of constant water density leads to:

$$\frac{\partial}{\partial x} \left[k_x(\psi) \frac{\partial \psi}{\partial x} \right] + \frac{\partial}{\partial y} \left[k_y(\psi) \frac{\partial \psi}{\partial y} \right] + \frac{\partial}{\partial z} \left[k_z(\psi) \left(\frac{\partial \psi}{\partial z} + 1 \right) \right] = \frac{\partial \theta}{\partial t} \quad (2.3)$$

The term $\partial\theta/\partial t$ of Eq. (2.3) can be rewritten in terms of the matric suction head by applying the chain rule:

$$\frac{\partial \theta}{\partial t} = \frac{\partial \theta}{\partial \psi} \frac{\partial \psi}{\partial t} \quad (2.4)$$

where $\partial\theta/\partial\psi$ is the soil water capacity [L^{-1}] (i.e., the slope of the relationship between volumetric water content and suction head):

$$C(\psi) = \frac{\partial \theta}{\partial \psi} \quad (2.5)$$

Substituting Equations (2.4) and (2.5) into Eq. (2.3), a governing equation for transient unsaturated flow may be written as:

$$\frac{\partial}{\partial x} \left[k_x(\psi) \frac{\partial \psi}{\partial x} \right] + \frac{\partial}{\partial y} \left[k_y(\psi) \frac{\partial \psi}{\partial y} \right] + \frac{\partial}{\partial z} \left[k_z(\psi) \left(\frac{\partial \psi}{\partial z} + 1 \right) \right] = C(\psi) \frac{\partial \psi}{\partial t} \quad (2.6)$$

Equation (2.6) is the Richards' equation. To solve Equation (2.6) mathematical descriptions of the soil water retention curve (SWRC) $\theta(\psi)$ and hydraulic conductivity function (HCF) $k(\psi)$ are required.

SWRC illustrates the relationship between suction and water content of a soil. Some common terms such as saturated volumetric water content, θ_s [L^3L^{-3}], residual volumetric water content, θ_r [L^3L^{-3}], air-entry value, ψ_b [L], are defined in Figure 2.3.

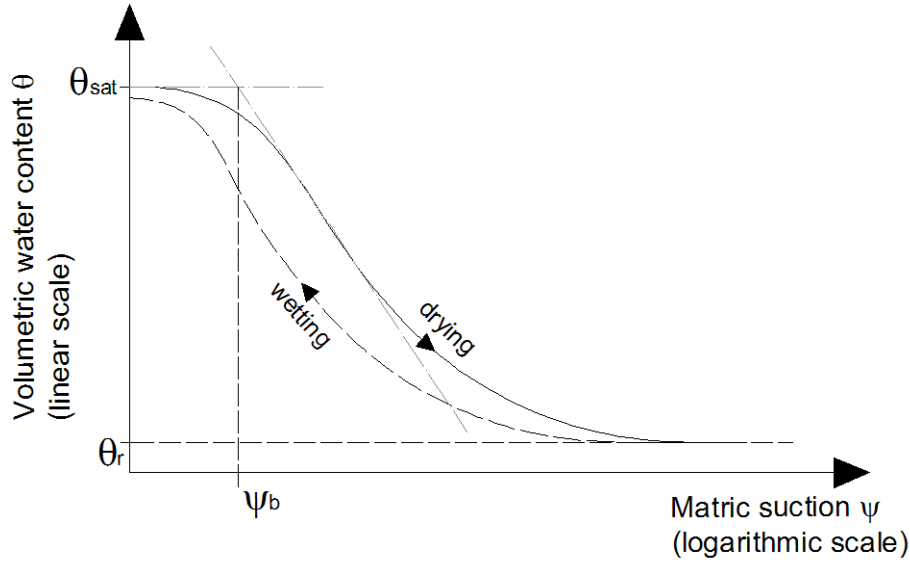


Figure 2.3. Typical soil-water retention curve showing approximate locations of residual water content θ_r , saturated water content θ_{sat} , and air entry value ψ_b .

Coefficient of permeability, volume change, pore-size distribution, particle size distribution, water content of soil at any matric suction, can be related to the SWRC directly or indirectly. A complete SWRC consists of drying and wetting curves (Fig. 2.2). The drying curve represents the water desorption of a soil when the matric suction increases while the wetting curve represents the water adsorption when matric suction decreases. A number of equations have been developed to describe the SWRC (Gardner, 1958; Brooks and Corey, 1964; van Genuchten 1980; Fredlund and Xing, 1994).

Among these, van Genuchten model (1980) historically has been widely adopted because of a higher degree of fitting to observed soil retention data. The van Genuchten equation has the following form:

$$S_e = \frac{\theta(\psi) - \theta_r}{\theta_{sat} - \theta_r} = \left[\frac{1}{1 + (\alpha\psi)^n} \right]^{1-\frac{1}{n}} \quad (2.7)$$

where S_e [-] is the relative saturation degree, θ [L^3L^{-3}] is the actual water content, ψ [L] is the matric suction head, α [L^{-1}] is a parameter that depends approximately on the water-entry value suction, n [-] is a parameter that depends on the soil pore-size distribution.

HCC illustrates the relationship between suction and hydraulic conductivity. The following Mualem model (1976) is an example of model to predict the hydraulic conductivity k of unsaturated porous media:

$$k(\psi) = K_{sat} S_e^{0.5} \left[1 - \left(1 - S_e^{\frac{n}{n-1}} \right)^{1-\frac{1}{n}} \right]^2 \quad (2.8)$$

where K_{sat} [LT^{-1}] is the saturated hydraulic conductivity.

The Richards equation may also be written in terms of volumetric water content. Following the chain rule, Darcy's law writes:

$$q_x = -k_x(\theta) \frac{\partial \psi}{\partial x} = -k_x(\theta) \frac{\partial \psi}{\partial \theta} \frac{\partial \theta}{\partial x} = -D_x \frac{\partial \theta}{\partial x} \quad (2.9a)$$

$$q_y = -k_y(\theta) \frac{\partial \psi}{\partial y} = -D_y \frac{\partial \theta}{\partial y} \quad (2.9b)$$

$$q_z = -k_z(\theta) \left(\frac{\partial \psi}{\partial z} + 1 \right) = -D_z \frac{\partial \theta}{\partial z} - k_z(\theta) \quad (2.9c)$$

where:

$$D = \frac{k(\psi)}{C(\psi)} \quad (2.10)$$

Where $D[\text{L}^2\text{T}^{-1}]$ is defined as the ratio of the hydraulic conductivity to the soil water capacity and is called hydraulic diffusivity for unsaturated soil.

Substituting Equations (2.9a), (2.9b), (2.9c) into Equation (2.6) leads to:

$$\frac{\partial}{\partial x} \left[D_x(\theta) \frac{\partial \theta}{\partial x} \right] + \frac{\partial}{\partial y} \left[D_y(\theta) \frac{\partial \theta}{\partial y} \right] + \frac{\partial}{\partial z} \left[D_z(\theta) \frac{\partial \theta}{\partial z} \right] + \frac{\partial k_z(\theta)}{\partial z} = \frac{\partial \theta}{\partial t} \quad (2.11)$$

2.3.2 Shear strength and infinite slope stability model of saturated/unsaturated soil

The shear strength of a soil is its resistance to shearing stresses. Shear strength is a measure of the soil resistance to deformation by continuous displacement of its individual soil particles. Shear failure occurs when the stresses between the particles are such that they slide or roll past each other. The Mohr-Coulomb failure criterion describes the state of stress on surfaces where failure occurs (Lambe and Whitman, 1979; Cernica, 1995). In its simplest form, the criterion may be expressed as:

$$\tau = c' + (\sigma - p_w) \cdot \tan \phi' \quad (2.12)$$

where τ [FL^{-2}] is the soil-shear strength, c' [FL^{-2}] is the effective soil cohesion, σ [FL^{-2}] is the normal stress, p_w [FL^{-2}] is the pore-water pressure and ϕ' [$^\circ$] is the effective angle of internal friction. In Equation (2.12) the term $(\sigma - p_w)$ represents the effective stress for saturated soil (Terzaghi, 1943).

Unlike a saturated soil, the shear strength of unsaturated soil involves two independent stress state variables: net normal stress, $(\sigma - p_a)$ [FL^{-2}], and matric suction, $(p_a - p_w)$ [FL^{-2}]. The shear strength of an unsaturated soil can be determined in the laboratory using modified direct

shear apparatus, as described in Gan et al. (1988), or modified triaxial apparatus, as described in Fredlund and Rahardjo (1993) and Tarantino and Tombolato (2005).

Bishop (1959) proposed the following single-valued effective stress equation for unsaturated soil:

$$\sigma' = (\sigma - p_a) + \chi(p_a - p_w) \quad (2.13)$$

Where σ' [FL^{-2}] is the effective stress for unsaturated soil, p_a [FL^{-2}] is the air-pore pressure, χ [-] is the effective stress parameter that depends on the degree of saturation or matric suction. The product $\chi(p_a - p_w)$ represents the interparticle stress due to suction (suction stress hereafter).

For saturated soil, p_a is zero, p_w is positive, χ is equal to one, and Equation (2.13) reduces to Terzaghi's classical effective stress equation $\sigma' = (\sigma - p_w)$. For completely dry soil, χ is equal to zero and the effective stress is $\sigma' = (\sigma - p_a)$. For partially saturated soil, χ is a function of the degree of saturation or matric suction.

Numerous equations which are either related to SWRC or other soil parameters were proposed to predict the effective stress parameter χ (e.g., Fredlund et al., 1978; Khalili and Khabbaz, 1998; Vilar, 2006). The validity of several forms of χ was examined by Vanapalli and Fredlund (2002) using a series of shear strength test results for statically compacted mixtures of clay, silt, and sand from Escario and Juca (1989). For matric suction ranging between 0 and 1500 kPa, the following two forms showed good fit to the experimental results:

$$\chi = \left(\frac{\theta}{\theta_{sat}} \right)^k \quad (2.14)$$

where k is a fitting parameter with experimental data, and:

$$\chi = \left(\frac{\theta - \theta_r}{\theta_{sat} - \theta_r} \right) = S_e \quad (2.15)$$

The Mohr-Coulomb failure criteria for unsaturated soil incorporating both Bishop's effective stress and suction stress concept is:

$$\tau = c' + [(\sigma - p_a) + \chi(p_a - p_w)] \tan \phi' \quad (2.16)$$

Equation (2.16) can be rearranged as:

$$\tau = c' + (\sigma - p_a) \cdot \tan \phi' + \chi(p_a - p_w) \cdot \tan \phi' = c' + c'' + \chi(p_a - p_w) \cdot \tan \phi' \quad (2.17a)$$

where:

$$c'' = \chi(p_a - p_w) \cdot \tan \phi' \quad (2.17b)$$

c' and c'' represent shear strength due to so called apparent cohesion in unsaturated soil. The apparent cohesion includes the classic cohesion c' representing shearing resistance arising from interparticle physiochemical forces such as van der Waals attraction, and a second term c'' describing shear resistance arising from capillarity effects (capillarity cohesion). Physically, capillarity cohesion describes the mobilization of suction stress $\chi(p_a - p_w)$ in terms of shearing resistance. The concept of suction stress and capillarity cohesion may be better illustrated by plotting Equation (2.17) in the three-dimensional space of Figure 2.4. Net normal stress in this regard is an independent stress state variable and suction stress is a material variable.

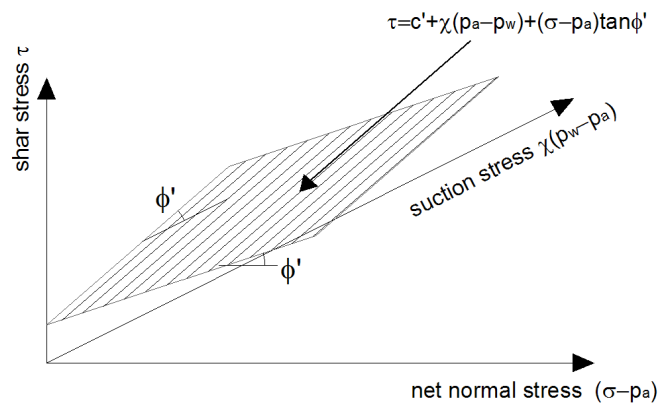


Figure 2.4. Shear strength surface in space of net normal stress, suction stress, and shear stress

In Figure 2.4 the failure surface remains planar no matter whether the soil is unsaturated or saturated. This feature makes it possible to represent the entire failure surface in a two-dimensional net normal stress-shear stress plot by plotting constant suction stress lines, leading to a series of parallel lines with different values of suction stress. Figure 2.5 shows the failure surface for two values of suction stress: one for zero suction head, the other for an arbitrary non zero value. The intersection with the normal stress axis in either case defines the tensile strength of the soil. The definition of suction stress and capillarity cohesion are logical extension of the classical Mohr-Coulomb criterion and the Terzaghi's effective stress principle. Physically, suction stress is an internal stress that results specifically from the partial saturation of the soil. Suction stress originates from the combined effects of negative pore pressure and surface tension.

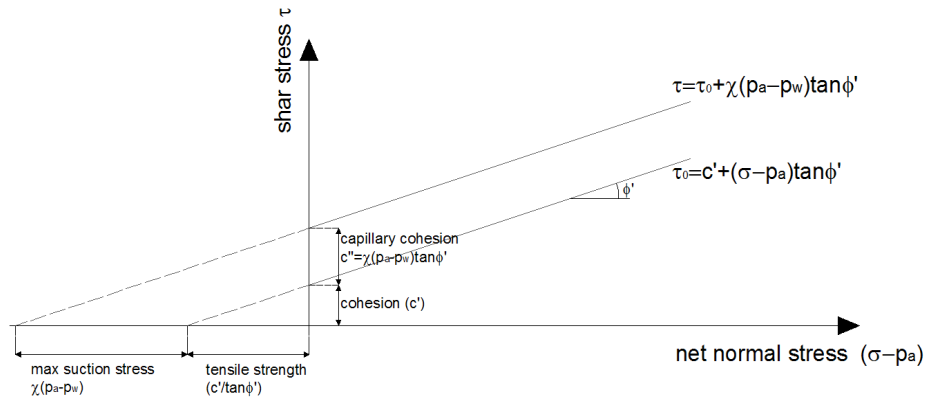


Figure 2.5. Projection of shear strength surface shown in Fig. 2.3 on shear stress-net normal stress plane.

By substituting Eq. (2.15) in Eq. (2.16) we obtain the following equation for shear strength prediction of unsaturated soil:

$$\tau = c' + [(\sigma - p_a) + \frac{\theta - \theta_r}{\theta_{sat} - \theta_r} (p_a - p_w)] \tan \phi' \quad (2.18)$$

where p_a [FL⁻²] is the pore-air pressure.

Generally, slope stability studies are based on the calculation of the factor of safety (FS). For hillslopes, it is common to define FS as the ratio of the resisting force, F_r , to the destabilizing force, F_d , (Graham, 1984):

$$FS = \frac{F_r}{F_d} \quad (2.19)$$

The slope is stable for $FS > 1$, while slope failure occurs when the critical state $FS = 1$ (such that $F_r = F_d$) is achieved. At the catchment scale, the infinite slope stability hypothesis has been widely applied in many investigations of natural slope stability (e.g., Montgomery and Dietrich, 1994; Wu and Sidle, 1995; Vanbeek et al., 2002; Borga et al., 2002; D'Odorico et al., 2005; Casadei et al., 2003; Lu and Godt, 2008) because of its relative simplicity, where the thickness of the soil mantle is much smaller than the length of the slope. The infinite-slope formulation is derived from the law of static friction for a rigid block on an inclined plane. In Figure 2.6, W represents the weight of the block, β is the plane angle, and $\tan \phi$ is the coefficient of the static friction. Therefore, the resisting force is given by the product of the normal force $N = W \cos \beta$ and the coefficient of the static friction ($F_r = W \cos \beta \tan \phi$); the destabilizing force F_d is $W \sin \beta$. The block slides if $\tan \beta > \tan \phi$.

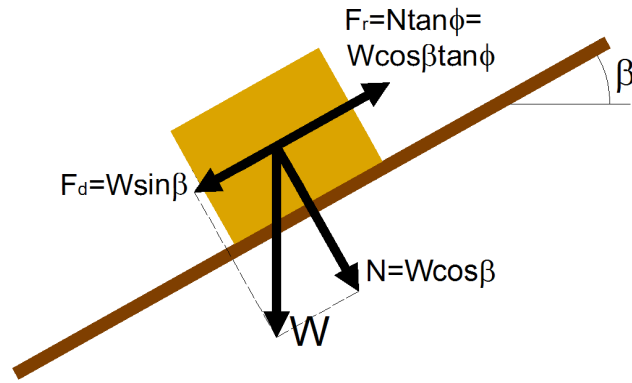


Figure 2.6. Schematic representation of the force balance on a rigid block on an inclined plane.

Generalizing for hillslope materials with effective cohesion c' [FL^{-2}], effective soil frictional angle ϕ' [$^{\circ}$], volumetric unit weight of soil γ [FL^{-3}], and slope parallel flow with a water-table thickness h [L] (above the failure surface), the factor of safety for an infinite slope reads:

$$FS = \frac{2c'}{\gamma z \sin(2\beta)} + \frac{\tan \phi'}{\tan \beta} - \frac{\gamma_w h}{\gamma z} (\tan \beta + \cot \beta) \tan \phi' \quad (2.20)$$

where γ_w [FL^{-3}] is volumetric unit weight of water.

Using the infinite slope stability model (2.20) analysis together with the shear strength of unsaturated soil given by (2.18) and the soil water retention curve (2.7), and assuming that the pore air pressure is atmospheric, the factor of safety of an infinite slope in unsaturated/saturated conditions can be written as:

$$FS = \frac{2c'}{\gamma z \sin(2\beta)} + \frac{\tan \phi'}{\tan \beta} + \frac{\gamma_w \psi}{\gamma z} (\tan \beta + \cot \beta) \tan \phi' \quad \text{for } \psi \leq 0 \quad (2.21a)$$

$$FS = \frac{2c'}{\gamma z \sin(2\beta)} + \frac{\tan \phi'}{\tan \beta} + S_e(\psi) \frac{\gamma_w \psi}{\gamma z} (\tan \beta + \cot \beta) \tan \phi' \quad \text{for } \psi > 0 \quad (2.21b)$$

where \bar{z} [L] is the vertical soil-depth.

2.4 Modelling shallow landslide occurrence at the catchment scale

Shallow landslide modeling is based on a variety of approaches and models. Statistical and physically-based approaches are widely adopted tools in catchment-scale shallow landslide modeling.

2.4.1 Statistical approach

The statistical methods are based on conceptual models. These models first require identification and mapping of a set of landslide causing (geological and geo-morphological)

factors that are directly or indirectly related to slope failures. Then, it involves an estimate of the relative contribution of these factors in generating slope failures, and classification of land surfaces into zones of different hazard or susceptibility degree (Aleotti and Chowdhury, 1999; Pathak and Nilsen, 2004). Bivariate and multivariate statistical methods are the most commonly used for these predictions. The bivariate statistical analysis is a method that describes the relationship between two variables. In landslide modeling, the bivariate method links each landslide causing factor to the landslide distribution map.

On the other hand, in multivariate statistical analysis, the weighted factors controlling the landslide occurrence indicate a relative contribution of each of these factors to the degree of landslide hazard within a defined land unit. The common property of these analyses is their nature of being based on the presence or absence of stability phenomena within these previously defined land units (Van Westen, 2000). The statistical approach can provide an insight into the multifaceted processes involved in shallow landslide occurrence, and useful assessments of susceptibility to shallow landslide hazard in large areas. However, the results are very sensitive to the data set used in the analysis and it is not straightforward to derive the hazard (i.e. probability of occurrence) from the susceptibility.

2.4.2 Physically-based models

Physically-based models attempt to extend spatially the slope stability models (e.g., the "infinite slope stability method") widely adopted in geotechnical engineering (Wu and Sidle, 1995; Iverson, 2000). To link rainfall pattern and its history to slope stability/instability conditions, physically-based models incorporate infiltration models (e.g., Green and Ampt, 1911; Philip, 1954; Salvucci and Entekabi, 1994). Various approaches have been proposed to predict the accumulation of the infiltrated water into the ground from relatively simple "pipe and pot" models to parsimonious topographic-index based models to complex, 3D variably saturated flow models based on Richards equation.

Topographically-based modeling has become very popular due to availability and quality of digital elevation models (DEMs). Elevation data are used in algorithms to calculate surface derivatives such as slope, aspect, flow direction, upslope contributing area, and topographic index. These topographic attributes are used in distributed hydrological modeling (Beven and Moore, 1993) and catchment scale shallow landslide modeling (Tarboton, 1997; Borga et al., 2002; Tarolli et al., 2006). Montgomery and Dietrich (1994), and Pack et al. (1998) have developed two catchment-scale shallow landslide models (SHALSTAB and SINMAP, respectively) where they use a steady state shallow subsurface flow based on the work by O'Loughlin (1986). They assume that the steady state hydrologic response model mimics what the relative spatial pattern of wetness would be during an intense natural storm which is not in steady state. A topographic index, TWI, given by the ratio between specific upslope contributing area and local slope is used as a surrogate for lateral subsurface flow processes.

The slope stability component (i.e., the infinite slope stability model) uses this topographic index to analyze the stability of each topographic element.

Assuming that there is no overland flow and no significant bedrock leakage, then the effective precipitation, q [LT^{-1}] (rainfall minus evapo-transpiration), times the upslope contributing area, A [L^2], must be the amount of runoff that occurs through a particular grid cell of width b [L] under steady state conditions (Figure 2.7):

$$q \cdot A = K_{sat} \cdot h \cdot b \cdot \sin \beta \quad (2.22)$$

where K_{sat} [LT^{-1}] is the saturated hydraulic conductivity, h [L] is the water-table thickness above the soil/bedrock interface, and β [$^\circ$] is the local slope angle.

Equation (2.22) can be rearranged in:

$$h = \frac{q}{K_{sat}} \cdot \frac{A}{b \cdot \sin \beta} = \frac{q}{K_{sat}} \cdot TWI \quad (2.23)$$

where TWI is the topographic wetness index.

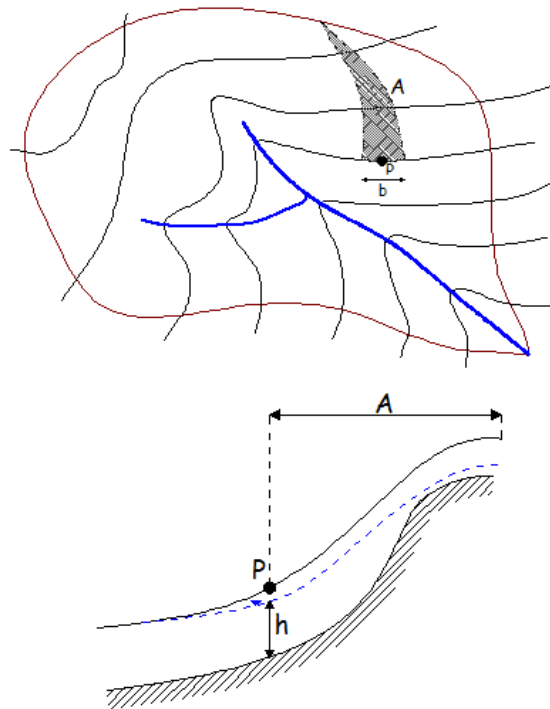


Figure 2.7. Sketch of an elementary drainage area: (top) planar view and (bottom) longitudinal section

Coupling Equation (2.23) with the infinite slope stability model (2.20) leads to the following expression of the factor of safety:

$$FS = \frac{2c'}{\gamma L \sin(2\beta)} + \frac{\tan \phi'}{\tan \beta} + \frac{\gamma_w}{\gamma} \frac{q}{K_{sat}} \frac{TWI}{L} (\tan \beta + \cot \beta) \tan \phi' \quad (2.24)$$

Several applications show this approach to be capable of capturing the spatial variability of shallow landslides hazard, because of the essential role of topographic control in shallow landsliding. This approach permits uncalibrated predictions and has proven reasonably successful, though there is a tendency for overprediction to occur (Dietrich et al., 2001). In fact, the approach by Montgomery and Dietrich (1994) and Pack et al. (1998) does not account for transient movement of soil water. This simplification can affect model capability of predicting shallow landslide potential because the steady flow condition can be unrealistic in the course of rainstorm.

Unsteady lateral subsurface flow was approached by Okimura and Ichikawa (1985) and Wu and Sidle (1995) by coupling the infinite slope stability model with a groundwater kinematic wave model. Borga et al. (2002) relaxed the hydrological steady-state assumption in topographic-index based shallow landslide models by using a modified version of the quasi-dynamic wetness index developed by Barling et al. (1994). This allowed them to obtain information on the rainfall duration needed to cause slope instability under the assumption that lateral subsurface flow in the saturated zone (i.e., below the water table) occurs simultaneously at any point across the catchment (Grayson et al., 1997). Casadei et al. (2003) linked a dynamic spatially distributed shallow subsurface runoff model accounting for evapotranspiration and unsaturated zone storage to an infinite slope model. To overcome the limitations of a kinematic wave hydrology in gentle and convergent slopes (Hilberts et al., 2004), Troch et al. (2003) and Hilberts et al. (2004) developed the hillslope storage Boussinesq (HSB) equation model. Subsequently, the HSB model has been coupled with the infinite slope stability model by Talebi et al. (2008) to investigate the effect of rainfall and water table variations on hillslope stability.

The build-up of pore water pressure as generated by the advance of the wetting front was investigated by Pradel and Raad (1993) using the Green-Ampt infiltration model to analyze the critical wetting front position triggering failure. Rulli et al. (1999) developed a distributed model coupling the Green-Ampt (1911) infiltration model, kinematic subsurface flow and infinite slope stability model in order to investigate shallow landslides in areas where Hortonian runoff generation is predominant. Iverson (2000) provided an insight of physical mechanism underlying landslide triggering by rain infiltration by solving the Richard's equation. The model links slope failure and landslide movement to groundwater pressure heads that change in response to rainfall. D'Odorico et al. (2005) coupled the short-term infiltration model by Iverson (2000) and the long-term steady state topography driven subsurface flow (Montgomery and Dietrich, 1994) and analyzed the return period of landslide triggering precipitation using hyetograph at different shapes. They assumed that the pore pressure transient observable in the course of a rainfall is due to the unsteady vertical flow through the soil profile, while slope-parallel subsurface flow is assumed to at a longer time-scale and to determine the pre-storm wetness conditions. This is also the approach used

in TRIGRS (transient rainfall infiltration and grid-based regional slope-stability analysis by Baum et al., 2008) which was developed to account for the transient effects of rainfall on shallow landslide initiation. TRIGRS combines an analytical solution for groundwater flow in one vertical dimension with an infinite-slope stability calculation (Savage et al., 2003; Baum et al., 2008). Slope-parallel subsurface flow is simulated by means of the topographic index approach and is used to set the initial soil-moisture condition for numerical simulations.

Three-dimensional hydrological models have been developed to perform physically-based simulations for well characterized field sites. Three-dimensional Richards' equation solvers provide a complete description of the pore pressure fields in saturated/unsaturated soil.

VanderKwaak (1999) developed the Integrated Hydrology Model (InHM) to quantitatively simulate fully coupled three-dimensional variably saturated subsurface flow and two-dimensional surface/channel flow. InHM is capable of simulating the four principal runoff generation mechanisms: Horton overland flow (i.e., infiltration excess), Dunne overland flow (i.e., saturation excess), subsurface stormflow, and groundwater flow. The flexibility of InHM has facilitated successful simulation of hydrologic response for a variety of catchment sizes and hydrologic environments (see VanderKwaak, 1999; Loague et al., 2005; Mirus et al., 2007; Heppner, 2007; Ebel et al., 2007). Simoni et al. (2008) combined the infinite slope stability model with GEOtop (Rigon et al., 2006). GEOtop simulates soil-moisture content and pore pressure evolution resulting from rain infiltration and models subsurface saturated and unsaturated flows, and turbulent fluxes across the soil-atmosphere interface. GEOtop model has been applied within a probabilistic framework in order to account for uncertainties of parameters, and Simoni et al. (2008) have proven to be able to reproduce a real event that occurred in the eastern Italian Alps (Sauris catchment). However, three-dimensional Richards' equation solvers require the solution of extremely large systems of equations even for small problems (Paniconi et al., 2003). Moreover, the parameterization and calibration of these models is often cumbersome due to the small amount and low accuracy of the available data (Hilberts, 2006). At the catchment scale it is most often necessary to make simplifying assumptions related to hydrologic response (Loague et al., 2006), and topographic-index based models are thus often preferred over more physically-based hydrological models.

2.5 Digital terrain modeling in hydrology: capabilities and limitation

There is a continuous demand for simpler techniques to assist with day-to-day land management. Action agencies responsible for land and water management are being required to identify those areas of land susceptible to various types of hydro-geological hazard such as erosion, landslides, and floods. With the increasing availability of digital elevation models (DEMs) topography was often used as an indirect pointer for water flow paths.

Digital terrain modeling has become increasingly popular with powerful analytical functions in geographic information systems (GIS). The results of DEM analyses are particularly powerful and useful in many environmental studies such as hydrological modeling (Beven and Moore, 1993), landslide hazard modeling (Montgomery and Dietrich, 1994; Pack et al., 1998; Acharya et al., 2006), soil mapping (Skidmore et al., 1991; Thompson et al., 2001; Scull et al., 2003), land-use change modeling (Verburg et al., 2002; Vanacker et al., 2003), erosion modeling (Mitasova et al., 1996; Cochrane and Flanagan, 1999; Amore et al., 2004).

In hydrological modeling, DEMs are most often used in algorithms to derive slopes, aspects, flow direction, upstream contributing area, etc. In particular, the use of DEMs and topographic attributes extracted from DEMs to simulate water flow paths and spatial patterns of wetness has been a central focus of hydrological modeling ever since the development of the area-slope index in geomorphology (Carson and Kirkby, 1972) and the topographic wetness index (TWI) in hydrology (Kirkby, 1975). These indices have been largely used to infer the water storage in the entire catchment area (e.g. Lamb et al., 1998), the extension of saturated areas (e.g., Grabs et al., 2009), and as general indicators of the influence of topography on soil–water storage dynamics (e.g., McGuire et al., 2005; Tetzlaff et al., 2009a, b) and shallow landslide triggering (e.g., Montgomery and Dietrich, 1994; Borga et al., 2002).

The traditional topographic index (Kirkby, 1975) is normally calculated, by digital terrain analysis, as the natural logarithm of the ratio between the drained area A per unit contour length b , $a=A/b$, and the slope of the ground surface at the location, $\tan\beta$: $TWI = \log(a/\tan\beta)$. Beven and Kirkby (1979) developed the topographic index into a terrain analysis-based hydrologic model (TOPMODEL), which is able to produce a simple relation of soil–water storage (deficit) in a catchment. This model expresses the local storage deficit below saturation by assuming that the major factor affecting the water flow paths is the catchment topography.

When calculating TWI from the DEM, different algorithms and modifications of the original “TOPMODEL” index can be used. The variants of TWI differ in the ways that the specific upslope area a , and local slope $\tan\beta$ are computed. Table 2.2 summarizes the algorithms that have been developed to compute the TWI since the early 1980s.

Calculation of upslope area depends on the way the accumulated area of upstream cells is routed to downstream cells. Traditionally, the area from a cell has been transferred in the steepest downslope direction to one of the eight neighbouring cells (O’Callaghan and Mark, 1984). Quinn et al. (1991) introduced a multidirectional flow algorithm that allowed the area from one cell to be distributed among all neighbouring downslope cells, weighted according to the respective slopes. An alternative single-direction algorithm was proposed by Tarboton (1997), who calculated the steepest downslope direction based on triangular facets that allowed the steepest direction to be routed in any direction rather than being restricted to the

eight cardinal and diagonal directions. The accumulated area is then routed to the two cardinal and diagonal directions that are closest to the steepest direction weighted according to their distance from.

Barling et al. (1994) were the first to deal with the problem of the steady-state assumption of flow, arguing that rainfall events are seldom sufficient to bring a hillslope to the steady-state condition. This motivated the development of their quasi-dynamic topographic wetness index with a time-variable upslope contributing area. They showed that the quasi-dynamic index was in closer agreement with the measured pattern of soil moisture storage than the traditional steady-state TWI

Table 2.2. A list of the major efforts of the last 30 years to produce more realistic terrain indices from digital elevation models

No.	Authors	Year	Terrain Index investigate	Improvement efforts focused upon	Method
1	Beven and Kirkby	1979	TWI		
2	O'Callaghan and Mark	1984	<i>a</i>	<i>a</i>	Single flow direction (D8)
3	Quinn et al.	1991	<i>a</i>	<i>a</i>	Multiple flow directions
4	Barling et al.	1994	<i>a</i>	<i>a</i>	Time-variable upslope area, $a(t)$
5	Tarboton	1997	<i>a</i>	<i>a</i>	Infinite possible single-direction flow path-ways (D^∞)
6	Beven and Freer	2001	TWI	<i>a</i>	Time-variable upslope area, $a(t)$
7	Borga et al.	2002	TWI	<i>a</i>	Time-variable upslope area, $a(t)$
8	Orlandini et al.	2003	<i>a</i>	<i>a</i>	Path-based method considering cumulative deviation (D8-LTD)
9	Hjerdt et al.	2003	$\tan\beta$	$\tan\beta$	Downslope index, DWI
10	Seibert and McGlynn	2007	<i>a</i>	<i>a</i>	Combination of multiple flow and D^∞ (MD^∞)

Table 2.2 shows that most of the developments in TWI to date have focused on new ways to compute specific upslope contributing area (O'Callaghan and Mark, 1984; Quinn et al., 1991; Tarboton, 1997; Orlandini et al., 2003; Seibert and McGlynn, 2007) or time-variable upslope contributing area (Barling et al., 1994; Beven and Freer, 2001; Borga et al., 2002). Local slope, $\tan\beta$, continued to be assumed a good surrogate to describe the local drainage propensity. One exception has been the development of the downslope wetness index, or drainage efficiency index, $DWI=d/L_d$, where L_d represents how far a particle of water has to travel along its flow path to lose a given head potential, d . Hjerdt et al. (2004) showed how this DWI outperformed the standard topographic index for mapping mire distribution in Sweden and approximating soil nitrate patterns and soil depths in headwater catchments in the USA. Nevertheless, subsequent use of the downslope index has shown equivocal results (e.g., Güntner et al. 2004; Grabs et al. 2009).

Some studies have questioned the fundamental assumptions of the topographic index theory (Burt and Butcher, 1985; Crave and Gascuel-Oudou, 1997; Seibert et al., 1997; Pellenq et al., 2003; Hjerdt et al., 2004). Two of these assumptions are of widespread use: (i) the hypothesis of steady-state subsurface flow, where time-dependent storage terms are neglected, and (ii) the validity of the kinematic-wave equation (KWeq) used to describe the subsurface water flow. The latter is an approximation of the Boussinesq equation in which, however, the diffusive term depending on hydraulic pressure gradient is neglected and the total hydraulic gradient is approximated with the slope of the topographic surface. The KWeq can therefore only propagate the effects of disturbances in a downslope direction and it cannot predict any backwater effect induced by complex dynamical organization of flow paths.

Furthermore, the topographic index framework does not account for subsurface flow path hydrological connectivity. As originally conceived, topographic index-based hydrological models do not account for storm flow, that is, shallow subsurface flow generated in the vadose (i.e., unsaturated) zone by perched water tables (or lateral unsaturated flow) just subsequent to storm events. Nor does it account for any representation of bedrock; specifically, the spatial distribution of soil thickness. In other words, topographic-index based models assume that subsurface flow hydrological connectivity in the saturated zone (i.e., below the water table) occurs simultaneously at any point across the catchment (Grayson et al., 1997).

2.6 Hydrological connectivity: Concepts and modelling

Hydrological connectivity has become an increasingly important topic for hydrology in recent years (Bracken and Croke, 2007). In a broad sense, hydrologic connectivity relates to the passage of water from one part of the landscape to another, thereby generating some catchment runoff response. This passage depends on static or *structural* elements such as topography and soil surface properties on the one hand and dynamic or *functional* processes such as the capacity of water to move through the system in response to some forcing on the other hand (Antoine et al., 2009).

Over the years there have been numerous definitions of hydrological connectivity (e.g., Western et al., 2001; Stieglitz et al., 2003; Bracken and Croke, 2007; Lane et al., 2004; Ocampo et al., 2006). However, as Stieglitz et al. (2003), in this thesis hydrological connectivity will refer to the condition by which disparate regions on the hillslope are linked via subsurface water flow.

When investigating storage–runoff relationships, hydrologists remain strongly influenced by ideas like the variable source area concept of Hewlett and Hibbert (1967). This concepts view runoff generation as a function of the volume or rate of inputs relative to the ability of landscape components to receive them. Following Hewlett and Hibbert (1967) were field studies that demonstrated the spatial and temporal dynamics of variable source areas (e.g.

Dunne and Black, 1970) and modeling studies that related these areas to topography (e.g. Beven and Kirkby, 1979 with their TOPMODEL). Difficulty in applying models based on these ideas in some environments has lead hydrologists to conduct field studies over the last 10–15 years (e.g., Western et al., 1999; Spence and Woo 2003; Tromp van Meerveld and McDonnell 2006a; Tromp van Meerveld and McDonnell 2006b). Results of these studies have revealed that changes to areas contributing to runoff are not continuous and that a little change in soil-water storage can have a dramatic effect on runoff response depending on how close parts of the basin are to meeting saturation thresholds. Research of runoff generation across a range of scales is supporting a shift to a new paradigm that views runoff generation not as the function of continual storage accumulation or depletion but as a threshold-mediated, connectivity-controlled process (Spence, 2010).

The degree of hydrological connectivity is mainly determined by the spatial organization of heterogeneity (Van Nieuwenhuysse et al., 2011). Soil characteristics affect the volume of rain-water can be infiltrated and define the rate at which this can occur. Soil moisture has been largely used to detect the degree of hydrological connectivity. The first attempt was lead by Western (Western et al., 1999 and 2001) in the Tarrawarra catchment in southwestern Australia. They observed that the spatial organization of the soil moisture produced alternating patterns of connection and disconnection to the catchment outlet (Western et al., 2001). Grayson et al. (1997) states that there are two contrasting soil moisture states (Figure 2.8). The dry state has a disorganized soil moisture patterns defined by local features (soil type, vegetation and slope). This is dominated by vertical percolation and infiltration processes. The wet state has a well-organized connected pattern dominated by larger scale upslope contributing are. This is dominated by lateral flow processes.

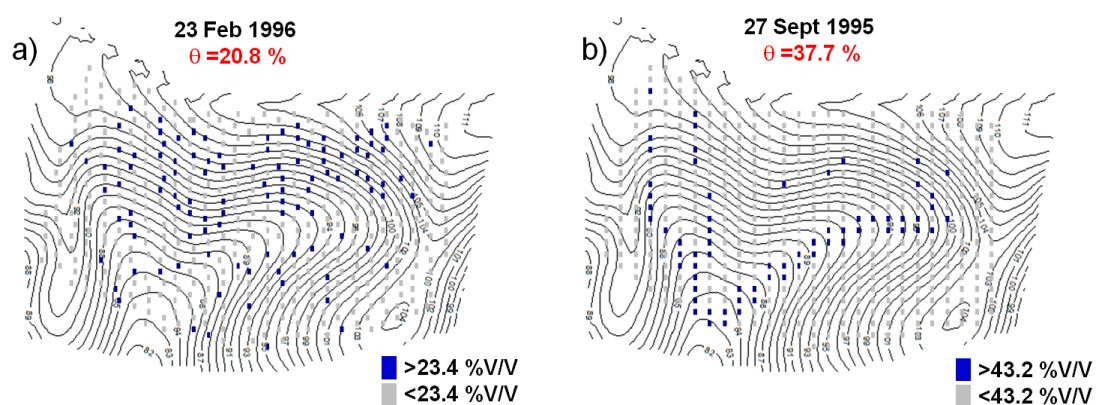


Figure 2.8. Diagrams of the development of soil moisture patterns (top 30 cm) showing the different degrees of connectivity between February (dry state) and September (wet state) 1996 at the Tarrawarra catchment. Contours show surface topography at 1 m intervals

This theory has been challenged by Tromp van Meerveld and McDonnell (2005) who argued that soil moisture can be a passive reaction to connectivity, particularly regarding subsurface flow. Soil moisture often co-varies with subsurface flow, however this is not necessarily a causal factor in subsurface flow. Tromp van Meerveld and McDonnell (2005) showed that at the Panola experimental hillslope in Georgia (USA) the subsurface saturation is the causal mechanism for production of lateral subsurface flow. Their data show that subsurface saturation is related to soil depth and bedrock micro-topography, not to soil moisture patterns, and that the relationship between median soil moisture does not represent the areas of subsurface saturation which indicates lateral flow (Figure 2.9).

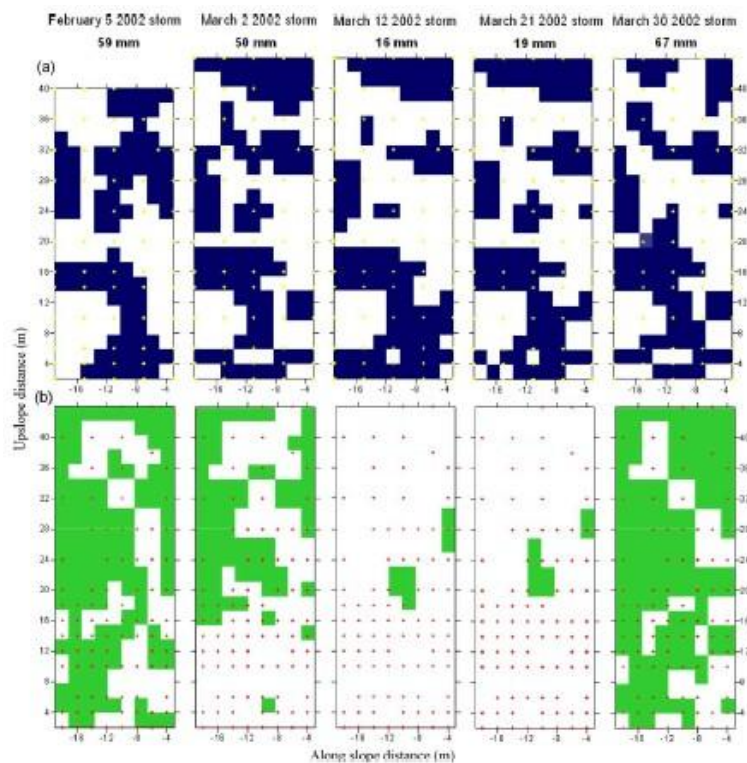


Figure 2.9. Map of the location of above median soil moisture (blue, a) and subsurface saturation (green, b) for 5 storms in 2002 at the Panola hillslope Georgia, USA, identifying the disparity between subsurface saturation and surface soil moisture. Yellow dots in (a) represent soil moisture measurement locations; red dots in (b) show the positions of maximum rise wells for water table detection. Taken from Tromp Van Meerveld and McDonnell (2005)

Western et al. (2005) agree with Tromp van Meerveld and McDonnell (2005) that saturation at some point in the profile is required for significant subsurface lateral flow and subsurface hydrological connectivity. However, they stated that the root-zone soil moisture represents an indicator of those processes, although the soil moisture pattern clearly needs to be interpreted in the context of properties of the soil profile.

The rough surface microtopography identified in other studies (Ali and Roy, 2010) highlight

the increased potential for subsurface throughflow. There has been increasing evidences that connectivity of subsurface flow paths is better represented by bedrock or impermeable soil subsurface topography (Tromp van Meerveld and McDonnell, 2006). Ground surface topography (normally used in topographic index-based hydrological model as a surrogate for subsurface hydraulic gradient) may be not sufficient to represent the subsurface flow processes. This fact highlights the need to consider the subsurface topography in the mathematical description of subsurface hydrological processes (Lanni et al., 2012).

However, numerical modeling often fails to represent adequately hydrological connectivity. Basic attempts to recognize the effects of connectivity have been introduced, such as through weighting delivery according to the distance of a land unit from the nearest water course (e.g., Johnes and Heathwaite, 1997; Munafo et al., 2005). Physically based, distributed models which solve for both the vertical and lateral flux of water across the landscape would implicitly account for hydrological connectivity. However, these models are commonly applied at grid-resolution coarser than those that are likely to control connectivity (Lane et al., 2009). The reasons for such coarse resolution are twofold. Firstly physically-based numerical models are exceptionally demanding in terms of parameterization (Merritt et al., 2003). The information demands of model calibration often exceed available data, and the models are rarely parsimonious with respect to the data available to determine them. The second reason comes from the computational difficulty of running such models with time steps that are small enough to capture the dynamics of catchment response and spatial resolutions that can capture the heterogeneous structure of the topography of drainage basins (Lane et al., 2009). At the state of the art, it is therefore required to make simplifying assumptions related to hydrologic response (Loague et al., 2006) in order to include a connectivity component in hydrological modeling (Lane et al., 2009).

Lane et al. (2004) have developed upon the topographic wetness index (TWI) of Beven and Kirkby (1979) in order to characterize connectivity of surface flow paths. As discussed above, TWI is commonly used as a measure of the relative propensity for a point in the landscape to develop saturation and, if saturation is controlled by topography alone, locations with the same value of the topographic index should have the same hydrological response. Lane et al. (2004) argued that the lowest value of TWI along a flow path that connects a point on a hillslope to the drainage network controls the connectivity of that point to the drainage network by surface overland flow. They called this lowest TWI value Network Index (NI) and implemented it in a diffusive risk modeling framework (the SCIMAP model) to include a connectivity component in simulating those risk that propagate via overland flow. Therefore, NI is limited to land areas where subsurface flow is not presented (Lane et al., 2009).

2.7 Summary of literature review

The current knowledge on rainfall infiltration into saturated/unsaturated soil and the behavior

of unsaturated soil shear strength and slope stability was presented in this chapter. The literature review highlighted that there are significant studies and models developed to predict the spatial and temporal occurrence of rainfall-triggered shallow landslides.

Topographically-based modeling of catchment-scale shallow landslide processes has become very popular in recent years, mainly due to the advances in availability and quality of digital elevation models (DEMs). DEM analyses are used in many terrain modeling applications to derive the topographic wetness index (TWI) used as a surrogate for lateral subsurface flow processes. The literature review highlighted that most of the developments in TWI to date have focused on new ways to compute specific upslope contributing area or time-variable upslope contributing area. Local slope, $\tan\beta$, continued to be assumed a good surrogate to describe the local drainage propensity, by neglecting the diffusive term (i.e., the gradient of the pressure head). The dynamic topographic wetness index presented in Chapter 3 represents an attempt to improve over the traditional topographic indices used in shallow landslide modeling.

Hydrologic connectivity related to the passage of water from one part of the landscape to another is not accounted for in the topographic index framework. The literature review depicted that at the hillslope scale hydrological connectivity is preliminary controlled by roughness in subsurface topography. Chapter 4 of this thesis will show that for the slope stability point of view, bedrock depressions may be responsible for the rapid pore pressure increase and rapid transition from stable to unstable conditions generally observed for shallow landsliding. This suggests that landslide models should consider the subsurface topography in order to include a connectivity component in the mathematical description of hydrological processes operating at the hillslope scale. An attempt to do this is presented in Chapter 5 of this thesis.

Chapter 3

A smoothed dynamic topographic index to describe the relative role of upslope and downslope topography on water flow paths and storage dynamics

3.1 Introduction

As reported in the literature review, some studies have questioned the fundamental assumptions of the topographic index theory, notably relating to the hypothesis of steady-state subsurface flow, where time-dependent storage terms are neglected and the validity of the kinematic-wave equation (KWeq) used to describe the subsurface water flow. KWeq is an approximation of the Boussinesq equation in which the diffusive term (i.e., the gradient of the pressure head) is neglected and the total hydraulic gradient is approximated with the local slope of the topographic surface. Thus, topographic wetness indices make the assumption that local drainage is not affected by downslope conditions.

Overall, the literature review highlighted the need to improve the metrics of local slope $\tan\beta$ in topographic wetness indices in order to better approximate both upslope and downslope controls on water flow paths, soil-water storage and resulting hydrological connectivity in the landscape.

Here, it is presented a new terrain-based index able to capture the relative role of upslope and downslope topography on water flow paths and (at least partially) overcome the limitations found in traditional topographic indices. The new index expands upon Barling's (1994) dynamic index concept to deal with past issues of local slope, overestimation of local hydraulic gradient (e.g., Crave and Gascuel-Oudou, 1997; Haitjema and Mitchell-Bruker, 2005) and (non-physical) fragmentation of the patterns (e.g., Lane et al., 2004; Sørensen and Seibert, 2007) especially when high-resolution DEM are analyzed. This is done by preserving the simple formulation and low computational demand which characterizes the use of popular, terrain-based indices.

The predictions of the new index and several other terrain-based indices are compared against patterns of water storage deficit (or water table depth) provided by a physically-based

model which describes the subsurface lateral flow dynamics obtained by solving the Boussinesq equation. This allows exploring how gradients of pressure head, induced by the downslope topography constraints, affect water storage dynamics and flow pathways organization.

This work has been published as: Lanni C, McDonnell JJ, Rigon R. 2011. On the relative role of upslope and downslope topography for describing water flow path and storage dynamics: a theoretical analysis. *Hydrological processes* **25**(25), 3909–3923. Doi: 10.1002/hyp.8263

3.2 Materials and methods

3.2.1 Study site

The study site used to test the index developed in this study is the 3.2 km² Salei alpine catchment in northern Italy. A 2 m-resolution DEM (with a total of 791636 cells) of the Salei basin was developed from LiDAR data. The catchment elevation ranges from 1,700 to 2,400 m above sea level. The average slope is 30°, with a substantial number of slopes that locally exceed 35°. A shallow sandy-silt, non-layered, soil (varying in depth from a few cm to 1-1.5 m), with medium-high saturated hydraulic conductivity ($K_{\text{sat}}=10^{-4}$ m/s) and soil-porosity $\Phi=0.3 \text{ m}^3 \text{ m}^{-3}$ (based on field observation by E. Farabegoli, pers. com.) covers the underlying bedrock. This bedrock consists of poorly fractured volcanoclastic conglomerates throughout the whole basin area. Annual precipitation is about 1000 mm (source: Meteo Trentino, Provincia Autonoma di Trento).

The catchment is characterized by two sub-basins, where steep hillslopes converge in two main central hollows. Topography represents a first order control for soil moisture patterns and subsurface flow paths as there are geological field evidence (by E. Farabegoli, pers. com.) that transient water tables develop at the soil-bedrock interface, generating relevant lateral flow during rainfall events. Terrain-based indices are therefore suitable to describe flow paths and storage dynamics at the Salei catchment, as also reported and detailed in other studies (Borga et al., 1998 and 2002; Tarolli et al., 2008; Orlandini and Moretti, 2009).

The watershed has been also used for shallow landslide studies. A comparison between patterns of slope instability predicted by the SHALSTAB model (Montgomery and Dietrich, 1994), GEOtop (e.g., Rigon et al., 2006) and inventoried landslide areas in the basin have highlighted the need to describe the transient nature of the subsurface flow mechanisms. The steady-state hypothesis used in SHALSTAB (similar to the TOPMODEL one) to simulate the hydrological control (i.e., the water table spatial patterns) on the triggering of shallow landslides leads to an overestimate of slope instability in the basin, and does not provide any information on the critical rainfall duration (i.e., the minimum rainfall duration needed to cause slope instability-e.g., Borga et al., 2002). This motivated the use of the Salei basin as a

shell for the development of the new terrain-based index.

Figure 3.1 shows the basic hydrological attributes used to define the new terrain-based index. Maps of the drainage directions (Figure 3.1a) were evaluated according to the path-based single flow direction method of Orlandini et al. (2003). This method was preferred over other methods (e.g., Quinn et al., 1991; Tarboton, 1997; Seibert and McGlynn, 2007) because it was shown to provide a better representation of flow paths across the surface of the Salei basin (Orlandini and Moretti, 2009; Gallant and Hutchinson, 2011). The drainage directions were coded by using a number between 1 and 8. A value of 1 indicates that the water particle moves eastward, a value of 2 indicates that the water particle moves northeasterly, and so on going counterclockwise.

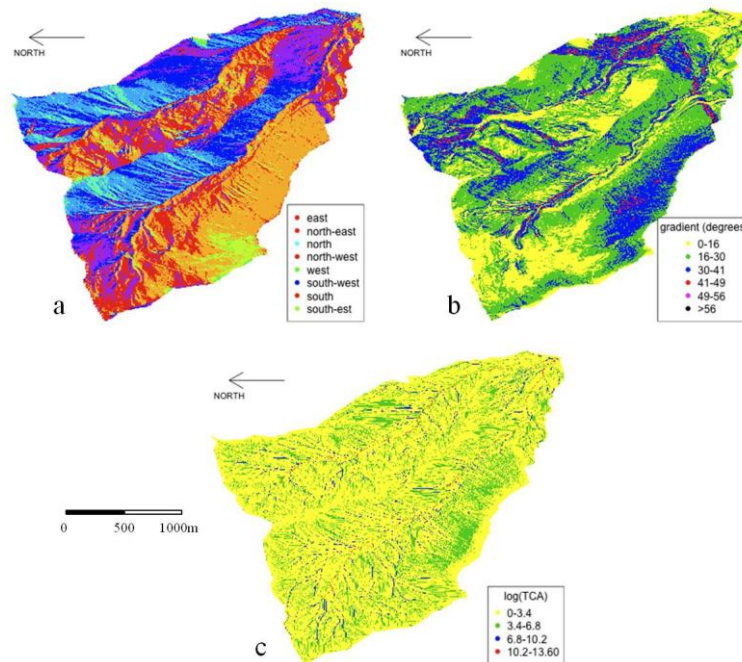


Figure 3.1. Maps of topographic drainage directions (a), local slope $\tan\beta$ (b), and upslope contributing area A (c) of the Salei catchment. The upslope contributing area is mapped as the natural logarithm of the area in m^2

3.2.2 The 2-dimensional Boussinesq (BEq) model

The numerical model BEq of Cordano and Rigon (submitted to *Water Resource Research*) is used to simulate flow paths, water table levels (i.e., soil-water storage deficit), and connectivity across the Salei catchment in response to three different rainfall events. The simulated rainfall events were characterized by the rainfall intensity (2, 4, and 8 mmh^{-1} , respectively), and the rainfall duration (16, 16, and 8h, respectively). These events correspond to events with a return period of one to ten years; therefore, they can be considered "typical" of the site. The results of these numerical simulations were then used to compare the performance of several terrain-based indices, including the new index

developed in this study.

The BEq model solves the following 2-dimensional form of the Boussinesq Equation (Bear, 1972):

$$\Phi(x, y) \frac{\partial H}{\partial t} = \nabla \cdot [K_{sat}(x, y, z) h(H, x, y) \vec{\nabla} H] + Q(x, y) \quad (3.1)$$

where H [L] is the hydraulic head (i.e., the water table elevation), h [L] is the pressure head which is a function of H and space: $h = \max(0, z_b(x, y))$ where $z_b(x, y)$ [L] is the bedrock elevation; t [T] is the time, $\nabla \cdot$ is the divergence operator, $\vec{\nabla}$ is the space gradient operator, $Q(x, y)$ [LT^{-1}] is a source term (for example the net rainfall intensity) which also accounts for boundary conditions (for instance the bedrock leakages), K_{sat} [LT^{-1}] is the saturated hydraulic conductivity, and $\Phi(x, y)$ [-] is the soil-porosity. The BEq model integrates each grid element, taking into account local variability of both topography and soil properties by a sub-grid parameterization (for further information on the numerical scheme download BEq on <http://www.geotop.org/cgi-bin/moin.cgi/Boussinesq>, or refer to Brugnano and Casulli, 2009).

Unlike the KWeq (kinematic wave equation), BEq does not neglect the diffusive term (i.e., the gradient of the pressure head $\vec{\nabla} h$) in the governing equations. Such process representation is therefore able to account for the enhancement or impedance of local drainage by downslope topography that has been generally neglected in previous studies (for instance, in Barling et al., 1994 or Grabs et al., 2009) where topographic indices were compared against patterns of water storage from KWeq-based hydrological.

3.2.3 The setting of the terrain-based indices

The ability of the new wetness index TWI_d^* , defined below to approximate the BEq-derived water table patterns was compared against the performance of five other topographic indices (Table 3.1).

Table 3.1: The six terrain-based indices defined in this study and their major features

<i>Index</i>	<i>Label</i>	<i>Formulation</i>	<i>Notes</i>
1	TWI	$\log\left(\frac{A/b}{\tan\beta}\right)$	Steady-state upslope contributing area by D8-LTD; Hydraulic gradient = local surface slope.
2	TWI_d	$\log\left(\frac{A(t)/b}{\tan\beta}\right)$	Time-variable upslope contributing area by D8-LTD; Hydraulic gradient = local surface slope.
3	TWI_d^{DWI}	$\log\left(\frac{A(t)/b}{DWI}\right)$	Time-variable upslope contributing area by D8-LTD; Hydraulic gradient = downslope index.
4	TWI_d^*	$\frac{1}{9}\left(TWI_d + \sum_{n=1}^8 TWI_{d_n}\right)$	As Index 2 with 3x3 low pass filter.
5	TWI^*	$\frac{1}{9}\left(TWI + \sum_{n=1}^8 TWI_n\right)$	As Index 1 with 3x3 low pass filter.
6	TWI^{mf}	$\log\left(\frac{A^{mf}/b}{\tan\beta}\right)$	Time-variable upslope contributing area by MF; Hydraulic gradient = local surface slope.

Index 1 in Table 3.1, $TWI = \log(a/\tan\beta)$, is the traditional topographic index (Beven and Kirkby, 1979) founded on the assumption of steady-state and local parallelism between ground and water table surfaces. It is defined as the natural logarithm of the ratio between the specific upslope contributing area a (here computed with the path based single flow routing algorithm D8-LTD of Orlandini et al., 2003) and the local slope, $\tan\beta$.

Index 2, TWI_d , is a dynamic topographic index which relaxes the hypothesis of steady-state by considering a time-linear variable upslope contributing area $A(t)$. The scenario shown in Figure 3.2 highlights the importance of considering the time-variable upslope contributing area to describe rainfall-runoff processes. In this example, two points, f and b , are located along the same drainage path. Point b (located downslope) presents a value of upslope contributing area larger than point f ($A_b > A_f$). Irrespective of the greater upslope contributing area, point b may actually be “recharged” by a smaller area than point f during a rainfall event of short duration, due to the upslope geomorphology. Hence, for a given duration T_c during a rainfall event, the effective (time-variable) upslope contributing area of point f , $A_f(t)$, may be larger than the effective upslope contributing area of point b , $A_b(t)$.

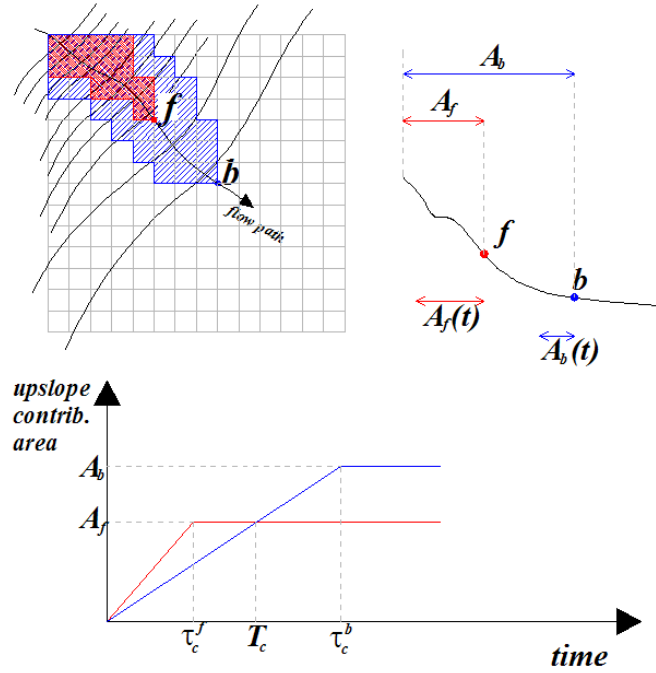


Figure 3.2. An example of time-variable upslope contributing area. Regardless of their steady-state upslope contributing area A , during a rainfall event the effective (time-variable) upslope contributing area, $A_f(t)$, of a point f located upslope may be larger than the effective (time-variable) upslope contributing area, $A_b(t)$, of a point b located downslope along the same flow path

The time-variable upslope contributing area is mathematically described by using the following linear model:

$$A_i(t) = \frac{t}{\tau_{c_i}} A_i \quad \text{for } t \leq \tau_{c_i} \quad (3.2a)$$

$$A_i(t) = A_i \quad \text{for } \tau_{c_i} \leq t \leq D \quad (3.2b)$$

$$A_i(t) = \max \left[0, A_i \left(1 + \frac{D-t}{\tau_{c_i}} \right) \right] \quad \text{for } t \geq D \quad (\text{if } \tau_{c_i} \leq D) \quad (3.2c)$$

$$A_i(t) = \max \left[0, A_i \left(\frac{2D-t}{\tau_{c_i}} \right) \right] \quad \text{for } t \geq D \quad (\text{if } \tau_{c_i} \geq D) \quad (3.2d)$$

Where $A_i(t)$ and A_i are, respectively, the time-variable upslope contributing area and the (steady-state) upslope contributing area in a given location i , t [T] is the time, D [T] is the

rainfall duration, and τ_{ci} [T] is the time of concentration of point i (i.e., the time required for a drop of water to travel from the most hydrologically remote location in the subcatchment to point i). Using Equation (3.2), the dynamic topographic index TWI_d (Index 2 in Table 3.1) in a generic point i can be written as:

$$TWI_{d_i} = \log\left(\frac{A_i(t)/b_i}{\tan \beta_i}\right) \quad (3.3)$$

Equations (3.2) and (3.3) require knowledge of τ_{ci} for each point in a catchment. We evaluated τ_{ci} as the maximum ratio between the flow-path length and the celerity of water given by Darcy's law:

$$\tau_{c_i} = \left[\frac{l_{H_j}}{\cos(\alpha_{l_{H_j}})} \cdot \frac{\Phi}{K_{sat} \sin(\alpha_{l_{H_j}})} \right]_{\max} \quad (3.4)$$

where $\alpha_{l_{H_j}}$ is the average inclination angle of a given flow path, j , of horizontal length l_{H_j} , which converges in the generic watershed-point i . If both soil-porosity, Φ , and saturated hydraulic conductivity, K_{sat} , are assumed constant in space, then Equation (3.4) becomes:

$$\tau_{c_i} = \left[\frac{l_{H_j}}{\cos(\alpha_{l_{H_j}}) \cdot \sin(\alpha_{l_{H_j}})} \right]_{\max} \cdot \frac{\Phi}{K_{sat}} = L_{H_i} \cdot \frac{\Phi}{K_{sat}} \quad (3.5)$$

where L_{H_i} is a morphological ratio given by $L_{H_i} = \left[\frac{l_{H_j}}{\cos(\alpha_{l_{H_j}}) \cdot \sin(\alpha_{l_{H_j}})} \right]_{\max}$.

By using the same Equation (3.2), we defined the TWI^{DWI}_d (Index 3 in Table 3.1) by replacing the local slope, $\tan \beta$, with the downslope index, DWI , in Equation (3.3):

$$TWI_{d_i}^{DWI} = \log\left(\frac{A_i(t)/b_i}{DWI_i}\right) \quad (3.6)$$

TWI^{DWI}_d relaxes the hypothesis of parallelism between ground and water table surfaces. Three values of d were selected to define DWI : $d=2m$, $d=5m$ and $d=10m$. The DWI for a generic point i was evaluated as the slope of the line that connects the point i with the first point located d -meters below the elevation of point i . This was done by assuming that the drop of water travels along the topographic drainage direction (Figure 3.3).

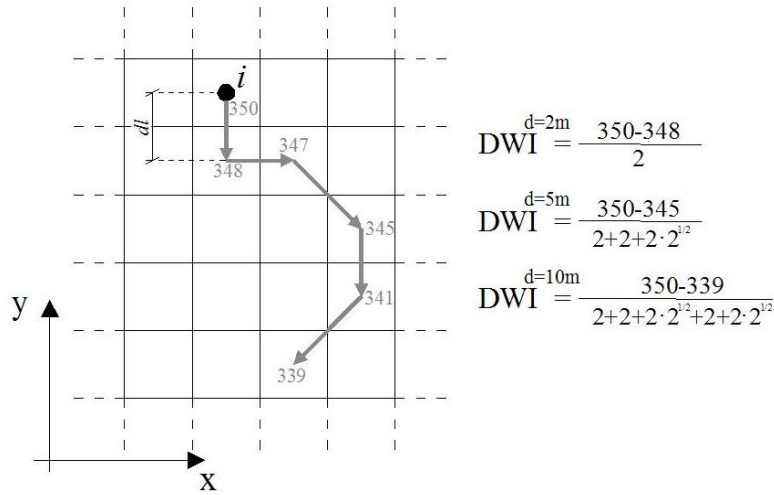


Figure 3.3. Value of DWI for a point i and three values of d (2, 5, 10m). The numbers inside cells are elevations (expressed in meters), arrows represent topographic drainage directions, and dl (2m) is the DEM resolution.

The new smoothed dynamic index TWI_d^* (*Index 4* in Table 3.1), was obtained by applying a 3x3 low-pass filter to the map of the dynamic wetness index TWI_d (i.e., by replacing the dynamic wetness index at cell i , TWI_{d_i} , with the average value from the surrounding n -cells):

$$TWI_{d_i}^* = \frac{1}{9} \left(TWI_{d_i} + \sum_{n=1}^8 TWI_{d_n} \right) \quad (3.7)$$

The 3x3 low-pass filter increases the spatial autocorrelation of the terrain index by smoothing out local variations in the spatial distribution of the dynamic wetness index TWI_d .

TWI^* (*Index 5* in Table 3.1) is a modified version of the traditional topographic index where the 3x3 low-pass filter is applied on the TWI 's map (*Index 1*) to consider the effect of non-local topography:

$$TWI^* = \frac{1}{9} \left(TWI_i + \sum_{n=1}^8 TWI_n \right) \quad (3.8)$$

This index differs from *Index 4* since it does not remove the hypothesis of steady-state.

The last index defined in this study is a second “traditional topographic index” (TWI^{mf} , *Index 6* in Table 3.1) where the upslope contributing area (A^{mf}) was computed by using the dispersive multiple flow direction algorithm of Quinn et al. (1991):

$$TWI^{mf} = \log \left(\frac{A_i^{mf} / b_i}{\tan \beta_i} \right) \quad (3.9)$$

A^{mf} is computed by distributing the incoming upslope flow to every adjacent downslope cell

on a slope-weighted basis. This method has been shown to be able to improve the computation of drainage areas and the description of flow paths over morphologically divergent terrains (e.g., Freeman, 1991; Quinn et al., 1991) where hydrodynamic dispersion is generally highly relevant.

In the following sections, *Index 1* (TWI) and *Index 5* (TWI^{mf}) are termed “traditional non-dispersive topographic index TWI” (since it was computed by using Orlandini’s path-based single flow routing method) and “traditional dispersive topographic index TWI^{mf}” (since it was computed by using Quinn’s dispersive multiple flow routing method), respectively.

3.2.4 Performance Criteria

The goal of this theoretical analysis was to assess the ability of the six wetness indices to reproduce water table fluctuation (i.e., dynamics of water storage deficit) and subsurface flow paths derived from the physically-based BEq model. Specifically, it is tested the ability of each index to generate a clear contrast between wetter and drier zones.

Spatially uniform representation of rainfall, hydraulic conductivity, and soil-porosity is used to run the BEq model in order to obtain predictions only affected by topography. The results are an emerging property of the model simulation and can be consistently compared to the spatial distribution of the terrain-based wetness indices defined in Table 3.1.

Two approaches were used to compare wetness patterns derived from the BEq model with those derived from the terrain-based wetness indices of Table 3.1. For the first approach (Approach I), reclassified binary maps with specific threshold values were used to differentiate between wetter and drier zones. For the second approach (Approach II), continuous data of terrain indices and water table levels (i.e., deficit of storage, according to TOPMODEL definition) derived by the BEq model were used. The two different approaches enabled to verify that results were not dependent on the particular method used to classify the patterns of storage (binary versus continuous data). Six statistical measures were used to identify the level of similarity between wetness-indices and simulated patterns of wetness/dryness: five similarity coefficients were used to assess the level of similarity in Approach I, while Spearman’s rank correlation coefficient (Spearman, 1904) was used to assess the level of map similarity in Approach II.

To reclassify the original maps into binary (wetter/drier) maps, the spatial distribution of values above or below a given threshold value was rearranged by coding each value as an indicator function $I(z_i; z_k)$:

$$I(z_i; z_k) = 1 \quad \text{if } z_i \geq z_k \quad (3.10a)$$

$$I(z_i; z_k) = 0 \quad \text{if } z_i < z_k \quad (3.10b)$$

where z_i is the value of wetness index or water table level in point i , and z_k is the threshold value that separates the drier areas from the wetter ones.

A second indicator datum $\underline{I}(z_i; z_k)$ (such that $\underline{I}(z_i; z_k)=0$ if $z_i \geq z_k$ and $\underline{I}(z_i; z_k)=1$ if $z_i < z_k$) was also defined in order to guarantee the following condition:

$$\sum_N I(z_i; z_k) + \underline{I}(z_i; z_k) = N \quad (3.11)$$

where N is the total number of cells in the raster map. The 75th percentile of the individual empirical cumulative distribution functions (ECDFs) was used to define the threshold value z_k and to separate the wetter areas from the drier ones. For comparison, the 25th percentile as indicator threshold z_k was also used in order to assess the ability of the different terrain indices to include topographic divergent areas among the wetter zones.

The similarity coefficients used to assess the level of similarity of the binary maps (Approach I) are summarized in Table 3.2 (the case of the traditional topographic index TWI is there reported).

Table 3.2: An overview of the applied similarity coefficients (Approach I) and their theoretical range. The case of the traditional dispersive TWI index is here reported

<i>Similarity Coefficient</i>	<i>Formulation</i>	<i>Range</i>
λ	$\frac{\sum_{i=1}^N \underline{I}(TWI_i; TWI_{75^{th}}) \cdot I(h_i; h_{75^{th}})}{\sum_{i=1}^N I(TWI_i; TWI_{75^{th}}) \cdot I(h_i; h_{75^{th}}) + \sum_{i=1}^N \underline{I}(TWI_i; TWI_{75^{th}}) \cdot I(h_i; h_{75^{th}})}$	[0,1]
μ	$\frac{\sum_{i=1}^N I(TWI_i; TWI_{75^{th}}) \cdot \underline{I}(h_i; h_{75^{th}})}{\sum_{i=1}^N I(TWI_i; TWI_{75^{th}}) \cdot \underline{I}(h_i; h_{75^{th}}) + \sum_{i=1}^N \underline{I}(TWI_i; TWI_{75^{th}}) \cdot \underline{I}(h_i; h_{75^{th}})}$	[0,1]
SM	$\frac{\sum_{i=1}^N I(TWI_i; TWI_{75^{th}}) \cdot I(h_i; h_{75^{th}}) + \sum_{i=1}^N \underline{I}(TWI_i; TWI_{75^{th}}) \cdot \underline{I}(h_i; h_{75^{th}})}{N}$	[0,1]
SC	$\frac{\sum_{i=1}^N I(TWI_i; TWI_{75^{th}}) \cdot I(h_i; h_{75^{th}})}{\sum_{i=1}^N I(h_i; h_{75^{th}})}$	[0,1]
Ck	$\frac{SM - RA}{1 - RA}$	$[-\infty, 1]$

The overall probability of random agreement, RA, which appears in Ck is given by:

$$RA = \frac{\sum_{i=1}^N I(TWI_i; TWI_{75^{th}})}{N} \cdot \frac{\sum_{i=1}^N I(h_i; h_{75^{th}})}{N} + \frac{\sum_{i=1}^N I(TWI_i; TWI_{75^{th}})}{N} \cdot \frac{\sum_{i=1}^N I(h_i; h_{75^{th}})}{N} \quad (3.12)$$

These five coefficients have been used in several similar studies (e.g., Rodhe and Seibert, 1999; Günter et al., 2004; Grabs et al., 2009). λ and ν represent, respectively, the proportion of false negative cases (i.e., the rate of occurrence to predict a “drier” area when the BEq results in being a “wetter” area) and false positive cases (i.e., the rate of occurrence to predict a “wetter” area when the BEq results in being a “drier” area). The simple-matching coefficient (SM) specifies the percentage of catchment-points where both the topographic index and the BEq-derived water-table depth (or storage deficit) predict values larger than their respective threshold values z_k . SC is a measure of direct spatial coincidence, and Cohen’s kappa coefficient (Ck, Cohen, 1960) is a coefficient able to take into account the agreement occurring by chance.

A modified version of the Hoshen-Kopelman algorithm (Hoshen et al., 1997) was used to compute the number of “wetter clusters” (i.e., spatial aggregates of value above the threshold z_k that separates the drier areas from the wetter ones) in the binary maps of the different terrain indices. The size of the “wetter clusters” and their cumulative distribution function (ECDF_{size}) were also determined. This was done in order to assess the capacity of the different terrain indices to (a) separate wetter areas from surrounding drier areas, (b) to reproduce the size of the isolated wetter clusters provided by the BEq model. The rationale behind this is that a high number of isolated clusters indicates limited ability of the wetness index to clearly separate the wetter areas from the drier areas.

3.3 Results

3.3.1 The role of the diffusive term

The BEq model simulated the water-table depth (i.e., the water storage deficit) at each point in the Salei basin during the investigated rainfall events. Here, only results of a 16 hour-long, 4mmh^{-1} -intense rainfall event are presented, since the qualitative results were the same for the other simulated rainfalls (a 16 hour-long, 2mmh^{-1} -intense rainfall, and an 8 hour-long, 6mmh^{-1} -intense rainfall).

Figure 3.4 plots the drainage directions from the BEq-derived water-table surface $\vec{V}(z_b + h)$ against the direction of the terrain gradient (or local slope) $\vec{V}(z_b)$. The four graphs refer to the 1st (top-left), 6th (top-right), 11th (bottom-left), and 16th hour (bottom-right) from the onset of rainfall. In Figure 3.4, the direction of $\vec{V}(z_b + h)$ was derived by using Orlandini’s single

flow path algorithm. The sizes of the circles indicate the percentage of catchment-points characterized by a given pair of water table (in abscissa) and topographic drainage (in ordinate) directions. The red diagonal contains the percentage of catchment-points where the $\vec{\nabla}(z_b + h)$ and $\vec{\nabla}(z_b)$ present the same direction, while circles outside of this diagonal represent the percentage of points where there is no coincidence.

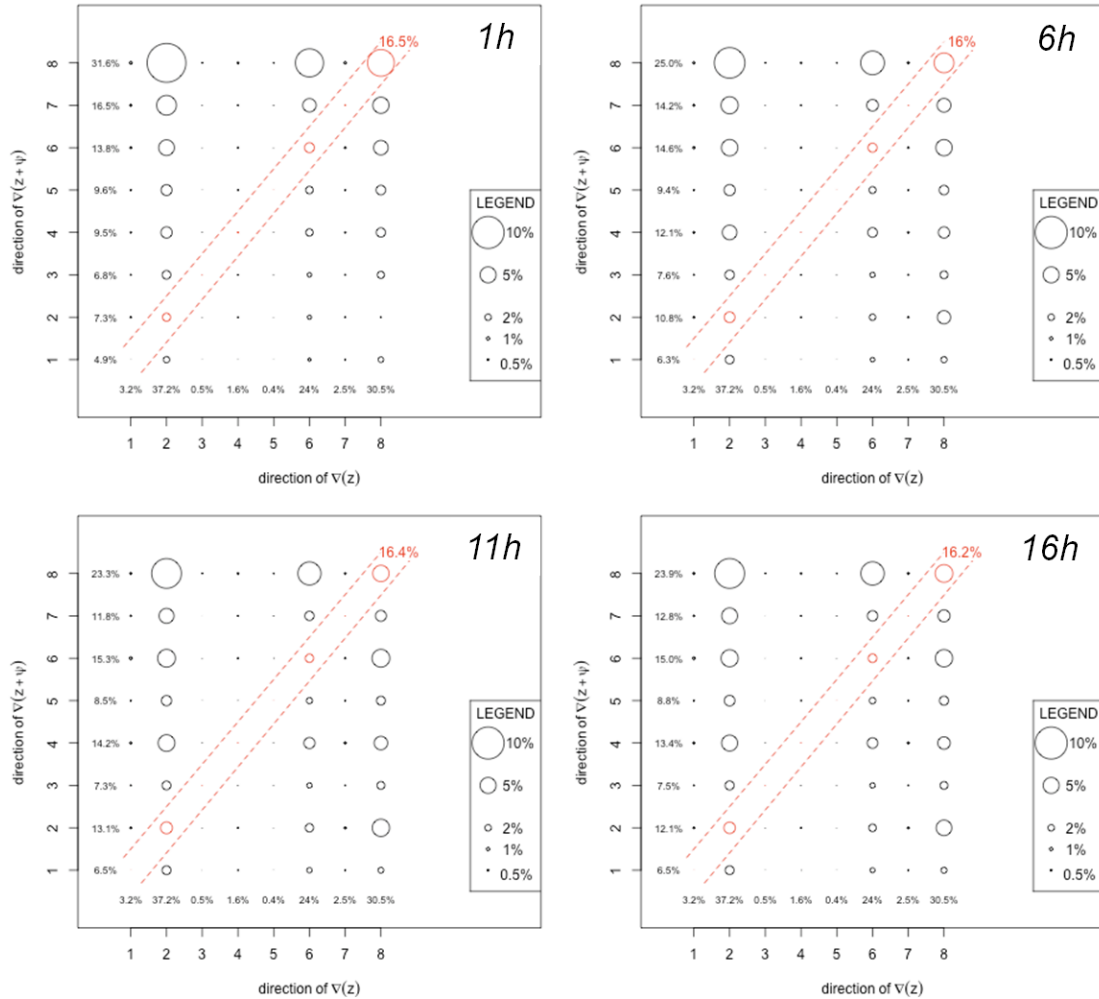


Figure 3.4. The direction of BEq-derived water table gradient $\vec{\nabla}(z_b+h)$ against the direction of the topographic surface gradient $\vec{\nabla}(z_b)$. Directions are coded with numbers ranging from 1 (east direction) to 8 (south-east direction), going counterclockwise. The percentages in the left and bottom inside margins of the plots represent the percentage of points characterized by a given value of water table drainage direction and topographic surface drainage direction, respectively

The four graphs show that the direction of $\vec{\nabla}(z_b + h)$ equals the direction of $\vec{\nabla}(z_b)$ (i.e., that $\vec{\nabla}(h) = 0$) in only 16% of the catchment-points, and that in many cases the BEq-derived

flow direction did not follow the topographic paths. In fact, while the topographic surface tended to establish three main drainage directions (north-east direction, south-west direction; and south-east direction in 91.7% of cases), the direction of the subsurface flow (from the BEq-model) resulted in a more complex variability across the watershed. The BEq-derived flow paths also exhibited a temporal variability induced by dynamic soil-water potential effects not captured by the static topography. Given that the flow directions are time variable, then the local values of storage deficit are also time variable.

Figure 3.5 shows this effect of diffusive processes for a transect approximately perpendicular to the general direction of the topographic hollows (that can be considered representative of each other transect having the same direction). Along the transect, the surface topography and the BEq-derived water table surface were generally not parallel, particularly where the downslope topography induced backwater effects. A wedge of saturation developed near the topographic hollows and moved upslope from the foot of the slopes (Points 1 and 2 noted on the transect of Figure 3.5b) inducing larger storage in zones close to the hollows. Low saturation deficits were also present at some locations far from the hollows (for example, at point 3) where downslope topographic reliefs limit the release of water from areas located upslope.

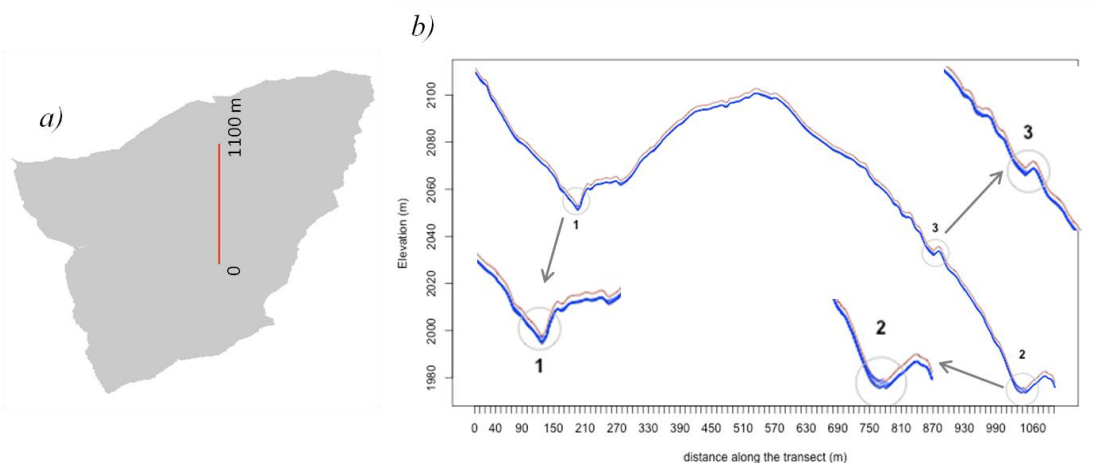


Figure 3.5. 2-dimensional transect of Salei catchment and simulated water-table level by BEq model. The red line in panel (a) shows the position of the transect reported in panel (b). Low water storage deficit is observed near topographic hollows at the foot slope and where the irregular downslope topography prevents the free water drainage

3.3.2 The performance of the terrain indices

3.3.2.1 Binary maps analysis (APPROACH I)

Indicator map derivation showed that the smoothed dynamic topographic index TWI_d^* was able to reproduce the dynamics of storage (or water table depth) generated by the BEq model

better than the other wetness indices listed in Table 3.1. The visual comparison among the five maps in Figure 3.6 allows a preliminary qualitative assessment of pattern similarity. This comparison indicates that TWI_d^* (Fig. 3.6d) is the most convincing index in describing similarity with the BEq-derived water storage patterns (Fig. 3.6e).

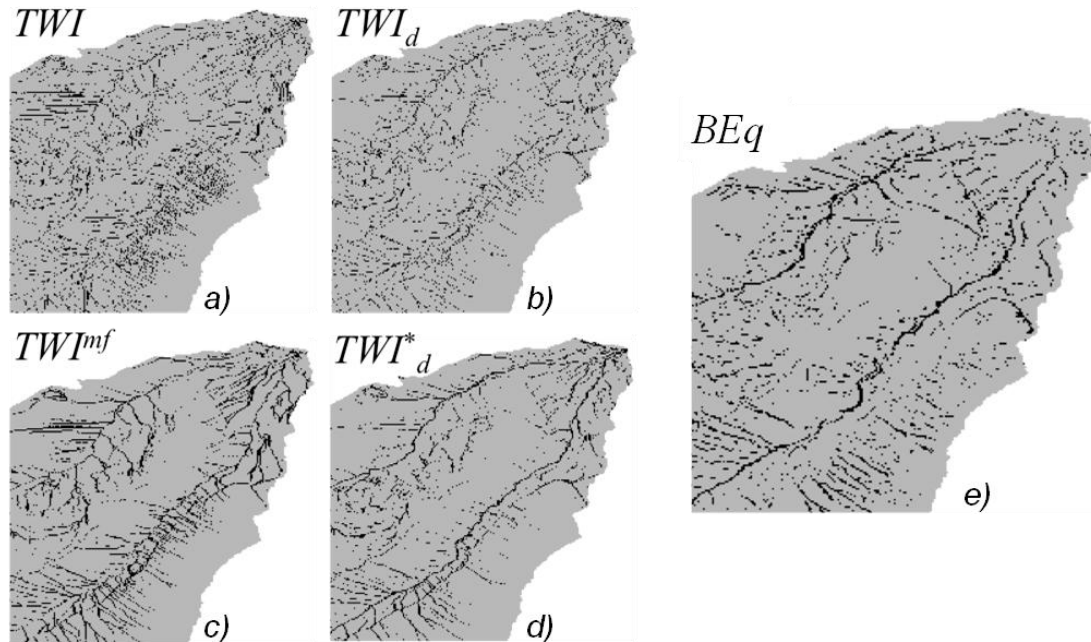


Figure 3.6. Spatial patterns of the traditional “non dispersive” topographic index TWI (a), dynamic topographic index TWI_d (b), traditional “dispersive” topographic index TWI^{mf} (c), smoothed dynamic topographic index TWI_d^* (d), and BEq-derived water table levels (e). The maps show in gray the points lower than the 75th percentile and in black the points higher than the 75th percentile of the individual cumulative distribution functions

The temporal evolution of the similarity coefficients λ , ν , SM , SC , and C_k between binary-coded terrain indices and simulated water table level are summarized in Table 3.3 and Table 3.4. Table 3.3 refers to $z_k=75^{\text{th}}$ percentile (i.e., the 75th percentile of the individual cumulative distribution functions was used as a threshold to separate wetter and drier areas), while Table 3.4 refers to $z_k=25^{\text{th}}$ percentile of the ECDFs.

Table 3.3: Similarity coefficients between reclassified binary maps of wetness indices (TWI , TWI^{mf} , TWI_d , TWI_d^*) and simulated water table depth (or storage deficit) by BEq model with $z_k=75$ th percentile of the individual cumulative distribution functions. Values in bold represent the best index at a given rainfall-hour

$z_k=75\%$	Label	Hour of simulation															
		1	2	3	4	5	6	7	8	9	10	11	12	13	14	15	16
λ	TWI	0.18	0.18	0.17	0.17	0.17	0.17	0.17	0.17	0.17	0.17	0.17	0.17	0.17	0.17	0.17	0.17
	TWI^{mf}	0.19	0.18	0.17	0.17	0.16	0.16	0.16	0.16	0.16	0.15	0.15	0.15	0.15	0.15	0.15	0.15
	TWI_d	0.16	0.15	0.15	0.14	0.14	0.14	0.14	0.14	0.14	0.14	0.14	0.14	0.14	0.14	0.15	0.15
	TWI_d^*	0.16	0.15	0.14	0.14	0.13	0.13	0.12	0.11	0.11							
ν	TWI	0.55	0.53	0.52	0.51	0.50	0.50	0.51	0.51	0.51	0.51	0.51	0.51	0.51	0.51	0.51	0.51
	TWI^{mf}	0.57	0.54	0.52	0.50	0.49	0.48	0.48	0.47	0.47	0.46	0.46	0.46	0.46	0.46	0.46	0.45
	TWI_d	0.48	0.46	0.44	0.43	0.42	0.42	0.42	0.42	0.42	0.42	0.43	0.43	0.43	0.44	0.44	0.44
	TWI_d^*	0.49	0.46	0.43	0.41	0.39	0.38	0.37	0.37	0.36	0.36	0.36	0.36	0.36	0.36	0.35	0.35
SC	TWI	0.45	0.47	0.48	0.49	0.49	0.49	0.49	0.49	0.49	0.49	0.49	0.49	0.49	0.48	0.48	0.48
	TWI^{mf}	0.43	0.46	0.48	0.49	0.51	0.52	0.52	0.53	0.53	0.54	0.54	0.54	0.54	0.54	0.54	0.54
	TWI_d	0.52	0.54	0.56	0.57	0.58	0.58	0.58	0.58	0.58	0.58	0.57	0.57	0.57	0.56	0.56	0.55
	TWI_d^*	0.51	0.54	0.57	0.59	0.60	0.62	0.63	0.64								
SM	TWI	0.72	0.73	0.74	0.74	0.75	0.75	0.75	0.75	0.75	0.74	0.74	0.74	0.74	0.74	0.74	0.74
	TWI^{mf}	0.71	0.73	0.74	0.75	0.76	0.76	0.76	0.76	0.77	0.77	0.77	0.77	0.77	0.77	0.77	0.77
	TWI_d	0.76	0.77	0.78	0.79	0.79	0.79	0.79	0.79	0.79	0.79	0.79	0.79	0.78	0.78	0.78	0.78
	TWI_d^*	0.75	0.77	0.78	0.79	0.80	0.81	0.81	0.82								
Ck	TWI	0.27	0.29	0.31	0.32	0.33	0.33	0.33	0.33	0.33	0.32	0.32	0.32	0.32	0.31	0.31	0.31
	TWI^{mf}	0.24	0.28	0.31	0.33	0.35	0.36	0.37	0.37	0.38	0.38	0.39	0.39	0.39	0.39	0.39	0.40
	TWI_d	0.36	0.39	0.42	0.43	0.44	0.45	0.45	0.44	0.44	0.44	0.43	0.43	0.42	0.42	0.41	0.41
	TWI_d^*	0.34	0.38	0.42	0.45	0.48	0.49	0.50	0.51	0.52	0.52	0.53	0.53	0.53	0.53	0.53	0.53

Table 3.4: Similarity coefficients between reclassified binary maps of wetness indices (TWI , TWI^{mf} , TWI_d , TWI_d^*) and simulated water table depth (or storage deficit) by BEq model with $z_k=25$ th percentile of the individual cumulative distribution functions. Values in bold represent the best index at a given rainfall-hour

$z_k=25\%$	Label	Hour of simulation															
		1	2	3	4	5	6	7	8	9	10	11	12	13	14	15	16
λ	TWI	/	0.58	0.56	0.53	0.49	0.48	0.48	0.48	0.48	0.48	0.48	0.48	0.48	0.48	0.48	0.48
	TWI^{mf}	/	0.56	0.53	0.48	0.43	0.41	0.40	0.39	0.39	0.38	0.38	0.37	0.36	0.36	0.36	0.36
	TWI_d	/	0.58	0.54	0.50	0.47	0.45	0.44	0.44	0.44	0.45	0.45	0.46	0.46	0.47	0.47	0.48
	TWI_d^*	/	0.60	0.56	0.50	0.44	0.41	0.39	0.38	0.37	0.36	0.36	0.35	0.35	0.35	0.35	0.35
ν	TWI	0.25	0.19	0.19	0.18	0.17	0.16	0.16	0.16	0.16	0.16	0.16	0.16	0.16	0.16	0.16	0.16
	TWI^{mf}	0.25	0.19	0.18	0.16	0.14	0.14	0.13	0.13	0.13	0.13	0.12	0.12	0.12	0.12	0.12	0.12
	TWI_d	0.25	0.19	0.18	0.17	0.16	0.15	0.15	0.15	0.15	0.15	0.15	0.15	0.15	0.16	0.16	0.16
	TWI_d^*	0.25	0.20	0.19	0.17	0.15	0.14	0.13	0.13	0.12							
SC	TWI	0.75	0.80	0.81	0.82	0.83	0.84	0.84	0.84	0.84	0.84	0.84	0.84	0.84	0.84	0.84	0.84
	TWI^{mf}	0.75	0.81	0.82	0.84	0.85	0.86	0.87	0.87	0.87	0.87	0.87	0.88	0.88	0.88	0.88	0.88
	TWI_d	0.75	0.80	0.81	0.83	0.84	0.85	0.85	0.85	0.85	0.85	0.85	0.85	0.85	0.84	0.84	0.84
	TWI_d^*	0.75	0.80	0.81	0.83	0.85	0.86	0.87	0.87	0.88							
SM	TWI	0.75	0.70	0.72	0.74	0.75	0.76	0.76	0.76	0.76	0.76	0.76	0.76	0.76	0.76	0.76	0.76
	TWI^{mf}	0.75	0.72	0.73	0.76	0.78	0.79	0.80	0.80	0.81	0.81	0.81	0.82	0.82	0.82	0.82	0.82
	TWI_d	0.75	0.71	0.73	0.75	0.77	0.77	0.78	0.78	0.78	0.78	0.77	0.77	0.77	0.77	0.76	0.76
	TWI_d^*	0.75	0.70	0.72	0.75	0.79	0.80	0.80	0.81	0.82	0.82	0.82	0.82	0.82	0.82	0.83	0.83
Ck	TWI	0	0.22	0.26	0.30	0.34	0.35	0.36	0.36	0.36	0.36	0.36	0.36	0.36	0.36	0.36	0.35
	TWI^{mf}	0	0.25	0.29	0.36	0.42	0.45	0.46	0.47	0.48	0.49	0.50	0.51	0.51	0.52	0.52	0.52
	TWI_d	0	0.22	0.27	0.33	0.37	0.40	0.41	0.41	0.41	0.40	0.40	0.39	0.38	0.38	0.37	0.36
	TWI_d^*	0	0.20	0.25	0.34	0.41	0.45	0.48	0.49	0.51	0.52	0.52	0.53	0.53	0.53	0.53	0.53

TWI_d approximated the BEq-derived storage deficit (or water table depth) most accurately

during the first and second rainfall hours (values in bold face), while TWI_d^* performed better in subsequent hours if wetter and drier areas were separated by using $z_k=75^{\text{th}}$ percentile. TWI^{mf} was better able to approximate the BEq-derived wetter areas during the first five rainfall hours with $z_k=25^{\text{th}}$ percentile of the individual ECDFs, while TWI_d^* outperformed the other indices in the subsequent hours.

The traditional dispersive topographic index TWI consistently performed worse than the other indices in both cases ($z_k=25^{\text{th}}$ percentile and $z_k=75^{\text{th}}$ percentile of ECDFs) confirming the need to relax the steady-state assumption and to consider non-local factors (e.g., non-local topography) in describing the local drainage and storage dynamics. Tables 3.3 and 3.4 also show that the similarity between TWI-BEq and TWI_d -BEq slightly decreases after the 8th rainfall hour, while the similarity between TWI^{mf} -BEq and TWI_d^* -BEq continued to increase until the last simulated hour when the diffusive processes are expected to become more relevant and the patterns of soil-water are highly connected and organized.

3.3.2.2 Spearman Rank analysis (APPROACH II)

In this second approach, Spearman's rank correlation coefficient ρ (Spearman, 1904) was used to assess the level of similarity between terrain index and BEq-derived patterns of storage deficit (or water table depth).

Figure 3.7a shows the shift in performance of the dynamic TWI_d index and the smoothed dynamic TWI_d^* index (first two hours versus the remaining), confirming the results obtained with APPROACH I and $z_k=75^{\text{th}}$ percentile of the ECDFs (Table 3.3).

The dynamic topographic index defined by using the downslope index (DWI) and $d=2\text{m}$ was the best index to approximate the BEq-derived patterns of storage deficit during the first three rainfall-hours (Figure 3.7a). However, the use of downslope index, DWI, instead of local slope, $\tan\beta$, reduced the ability of the dynamic index to reproduce the simulated water-table levels (TWI^{DWI}_d less effective than TWI_d), especially when the higher values of d (5 and 10 m) were used to derive the DWI.

The traditional topographic index TWI was generally recognized as the least performing index, confirming what has been found with APPROACH I.

Performance of the terrain indices increased when the steady-state hypothesis was relaxed (TWI_d better than TWI, with an average increase of Spearman's coefficient equal to $\overline{\Delta\rho} = +9\%$) and when the low-pass filter was applied to the dynamic topographic indices TWI_d (TWI_d^* better than TWI_d with $\overline{\Delta\rho} = +17\%$).

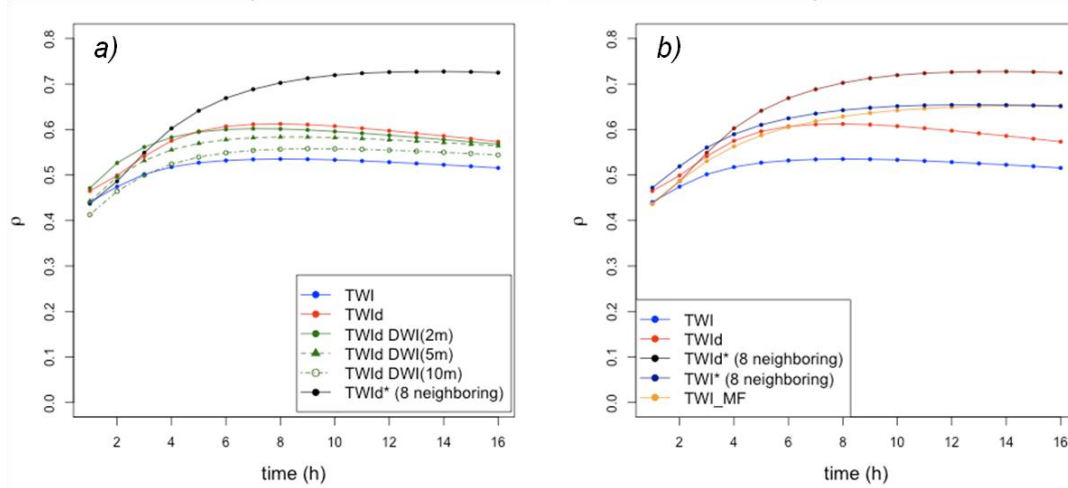


Figure 3.7. On the left, temporal evolution of Spearman's rank correlation coefficient ρ between simulated water table level and traditional non-dispersive topographic index, TWI (blue), dynamic topographic index, TWI_d (red), smoothed dynamic topographic index, TWI_d^* (black), and dynamic index where the DWI is used to describe the local drainage, TWI_d^{DWI} (green). On the right, the role played by the low-pass filter on the terrain indices performance

Figure 3.7b shows that the ability of topographic indices to reproduce the patterns of soil-water storage deficit derived with the BEq model improved when the low-pass filter was used to smooth out local variations (TWI_d^* better than TWI, and TWI_d^* better than TWI_d). The traditional dispersive topographic index TWI^{mf} performed similarly to the smoothed traditional dispersive index TWI^{mf} only from the 11th rainfall hour, when a considerable number of divergent areas also exhibited low saturation deficit. Figure 3.7b also shows that after the 8th rainfall hour Spearman's correlation coefficient ρ associated with TWI_d slightly decreases while Spearman's correlation coefficient ρ associated with TWI_d^* increases to remain steady after the 13th hour. Besides, Spearman's correlation coefficient ρ associated with TWI_d exceeded 0.7 after the 8th rainfall hour (approximately) indicating that the agreement between the index pattern and the simulated water table (or water storage deficit) pattern was good.

3.3.2.3 Connectivity analysis

The smoothed wetness index TWI_d^* and the traditional dispersive topographic index TWI^{mf} showed better ability to generate a clear contrast between wetter and drier areas than the dynamic TWI_d index and the traditional non-dispersive topographic TWI index (Figure 3.6). The analysis of the wetness patterns predicted by each of the wetness indices and the BEq model revealed that the number of wetter clusters (i.e., spatial aggregates of values larger

that the threshold value z_k generated by TWI^*_d and TWI^{mf} were very close to the number of BEq-derived wetter clusters (Figure 3.8, rightmost bars-block). However, while the TWI^{mf} index generated connected patterns of wetter clusters too large, the TWI^*_d index proved able to reproduce both the number of wetter clusters and the spatial aggregation of water storage patterns. In fact, the wetter clusters distribution from TWI^*_d showed statistical properties (mean and quantiles values) that were in good agreement with the statistical properties of the BEq-derived wetter clusters distribution (Figure 3.8, 1st-4th bars-blocks versus dashed lines). TWI and TWI^* overestimated the fragmentation of the wetness areas, while the DWI-derived dynamic wetness index, TWI^{DWI}_d (not reported in Figure 3.8), overestimated the clusters spatial extension and underestimated the number of clusters for high values of “loss of elevation” d (5 and 10 m), and, vice-versa, underestimated the clusters spatial extension and overestimated the number of clusters for $d=2$ m.

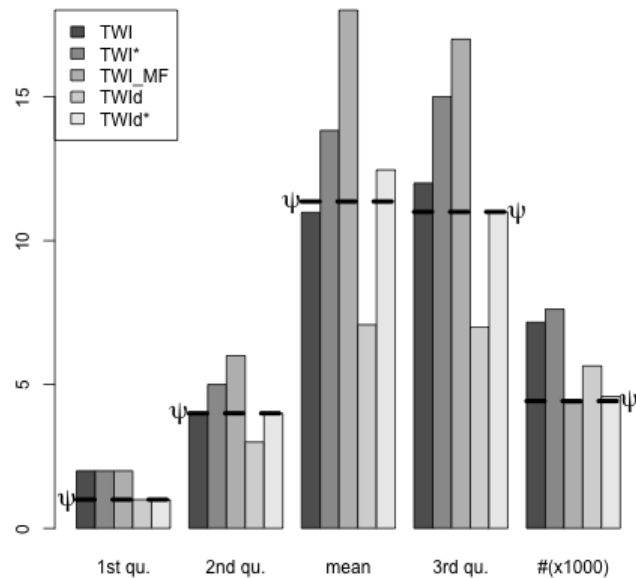


Figure 3.8. Bar plots showing the ability of the different terrain indices to reproduce connected “wetter” areas. The rightmost bars-block represent the number of isolated “wetter” clusters provided by the five (TWI , TWI^* , TWI^{mf} , TWI_d , TWI^*_d) terrain indices (bars) and the BEq model (dashed line). The first, second, third and fourth bars-blocks represent the 1st quantile, 2nd quantile, mean, and 3rd quantile values of the individual cumulative distribution functions of the “wetter” cluster sizes

3.4 Discussion

3.4.1 On the relative role of upslope and downslope topography for describing water flowpath, connectivity and storage dynamics

The use of a topographic wetness index for distributing soil-water storage imposes an inherent assumption about the controlling processes on subsurface flow dynamics, namely, that subsurface lateral flow dominates (e.g., Grayson et al., 1997). The results obtained in this theoretical analysis have shown that diffusive, pressure related, processes can significantly affect the subsurface lateral flow dynamics (Figures 3.4 and 3.5) and that the traditional topographic index alone is a poor proxy for describing subsurface flow paths and storage dynamics over complex topography. The steady state assumption which implies that the storage deficit at any point in a catchment is influenced by the total upslope contributing area, and the kinematic-wave theory, whereby the effects of disturbance can only propagate in a downslope direction, limit the ability of the traditional TWI index to describe storage dynamics in topographically complex, lateral flow-dominated mountain catchments.

Water storage deficit at a given location may in fact be strongly controlled by the downslope topography. Very steep and planar downslope topography enhances the local drainage, independently of the local value of the ratio between upslope contributing area and local slope. On the other hand, an abrupt decrease in slope angle or the presence of micro-topographic reliefs may prevent the free water drainage, inducing backwater effects. A saturation wedge may also develop at the foot of the hillslope and affect the upslope storage dynamics for a length depending upon the incoming flux from upslope (Hewlett and Hibbert, 1963; Weyman, 1973 and 1974). This mechanism can be intimately related to the hydrological connectivity between the topographic channel and the surrounding hillslopes, and it is not considered at all in the TWI index where downslope controls on local drainage are neglected. Therefore, rainfall-runoff models based on the traditional topographic index to describe the lateral subsurface flow component (i.e., the balance between the incoming upslope flow and the outgoing downslope flow) are not able to fully represent storage dynamics, at least for the right reasons, where downslope topography and soil water potential effects play an important role in controlling the local drainage.

3.4.2 On the need for hydrological smearing

None of the six terrain indices tested in this study were able to perfectly reproduce the dynamics of storage derived from the Boussinesq model. This is because none of them perfectly captures the hydrodynamic processes induced by the irregular and complex topography. The downslope index DWI attempts to include elements of the downslope topography to describe the local drainage propensity. However, results of this study have

shown that the DWI is difficult to apply in practice. The effective value of d (loss of elevation), a crucial element of the DWI method, must be chosen by trial and error—as a single value for the entire watershed—based on what local micro-topographic features (i.e., local irregularities) must be filtered out. Therefore, the value of d changes as a function of local morphology and is not a topological property of a basin.

The traditional dispersive topographic index TWI^{mf} attempts to include the hydrodynamic processes by distributing the incoming flow (i.e., the routed upslope contributing area) to a point among the neighboring cells at a lower elevation. This enabled it to better estimate water storage in divergent areas (Table 3.4) but, at the same time, TWI^{mf} showed poor performance with respect to the other tested quality measures (and specifically Spearman's correlation coefficient analysis and connectivity analysis). Orlandini and Moretti (2009) showed that multiple flow direction algorithms are not able to delineate the morphological drainage system, since physical dispersion inherent in transport processes across the topographic surface may not obey the same laws as artificial dispersion. The results of the study presented in this chapter support their findings by showing that a 3x3 low pass filter applied on the traditional non-dispersive TWI index was sufficient to outperform the dispersive TWI^{mf} index in approximating the BEq-derived water storage dynamics. In particular, TWI^{mf} showed small differences between convergent and divergent areas in the first rainfall hours when “wetter” cells were primarily areas of flow convergence (Figure 3.6, Table 3.3). This confirmed that multiple flow directions algorithms suffer from too high flow dispersion (Seibert and McGlynn, 2007) making it unable to reproduce subsurface flow paths in convergent areas.

Fine DEM grids create challenges for the TWI. Small-scale topographic “noise” generates high spatial variability in the ratio between upslope contributing area and local slope, reducing the ability of topographic index-based rainfall-runoff models to predict spatial patterns and dynamics of water storage. The problem has been noted by other researchers. For instance, Sørensen and Seibert (2007) argued that the water table shape may be smoother than the land surface topography and may be related more accurately to a coarse resolution DEM than to a finer resolution DEM. Wolock and Price (1994) concluded that coarse resolution DEMs were preferable to run the topographic index-based TOPMODEL as the predicted water-table shape may be better represented by a coarser resolution DEM. Lane et al. (2004) showed results that could be considered similar to ours. They argued that when fine-resolution DEMs are used to run TOPMODEL, a large number of unconnected saturated areas are produced. This is similar to our findings of high disaggregation of points observed in the traditional non-dispersive topographic index TWI and the dynamic index TWI_d (Figures 3.6a and 3.6b).

Values of upslope contributing areas for the Salei basin were greatly affected by the DEM-resolution (confirming results by Sørensen and Seibert, 2007). For example, the

percentage of basin-points having an upslope contributing area larger than 160 m^2 increased from 18% at 2 m-resolution to 70% at 10 m-resolution DEM. Therefore, the coarse 10 m-scale remains inappropriate to delineate water flow paths. In fact, the smoothed dynamic index TWI_d^* was poorly correlated with the BEq-derived storage deficit patterns when applied to this 10 m-resolution DEM, indicating that a fine-resolution DEM is a necessary element to compute our TWI_d^* and appropriate times of concentration τ_c . The 3×3 low-pass filter subsequently applied to the dynamic topographic index maps mitigated the effects of local irregularities in topography and allowed us to include non-local topographic effects in the terrain index computation. This resulted in less fragmented and more robust patterns of wetness (Figure 3.6).

The smearing process also allowed the reduction of the differences in the upslope contributing area between points near and points inside topographic hollows (spatial-threshold effect). Figure 3.9 provides a schematic representation of this spatial-threshold effect at the hillslope/channel transition. On “digital terrain”, points inside topographic hollows show values of upslope contributing area which are much higher than points immediately upslope. This effect is in contrast with results of the BEq model (Figure 3.5) which showed a similar water-storage propensity for topographic positions close to and inside the topographic hollows. In fact, as discussed above, in points close to the hollows local water storage is strongly controlled by the development of a saturated wedge that progressively expands in the upslope direction. As a result, locations near-topographic hollows may receive drainage not only from areas which are directly upslope from them but also downslope from them too.

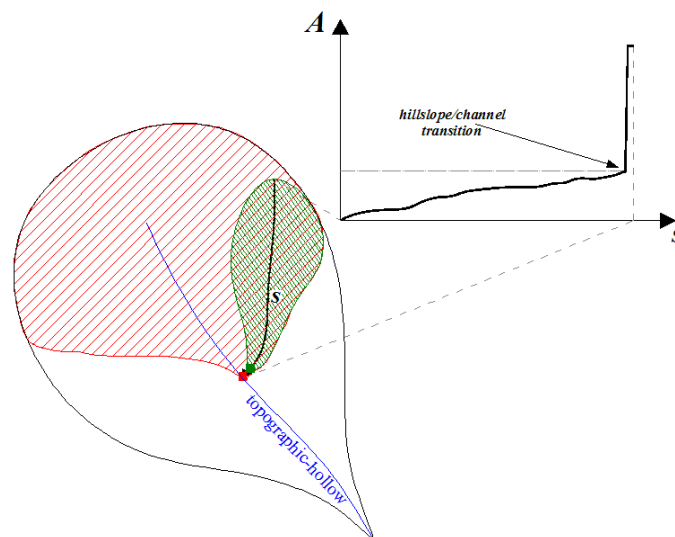


Figure 3.9. Conceptual representation of the threshold effect on the value of upslope contributing area at the hillslope/channel transition of digitized watersheds. The point inside the topographic hollow shows a value of upslope contributing area A much higher than a point located one pixel upslope

The smoothed dynamic index TWI_d^* has proven more capable to include these phenomena than existing topographic indices. However, it remains a terrain-derived index, and as such can be used to describe the dynamics of storage only when topography (i.e., lateral subsurface flow) is recognized as the predominant control on subsurface flow mechanisms. Under different landscape contexts from those analyzed in this work, storage dynamics and soil-moisture patterns can be dominated by other factors, such as soil drainability (Tetzlaff et al., 2009a), vegetation and micro-climate (Western et al., 2004), bedrock geology (Sayama et al., 2011) where a realistic representation of storage patterns and storage dynamics cannot be achieved through the use of a solely terrain-based wetness index. In these cases, appropriate procedures should be used to select the requisite level of hydrological model complexity able to represent the dominant processes (Fenicia et al., 2008), consistent with empirical observations (Birkel et al., 2010 and 2011).

3.5 Concluding remarks

The position of the water table and the storage deficit below saturation at a given point in a watershed is the result of a balance between upslope accumulation of water, downslope drainage efficiency, and vertical recharge from the unsaturated zone—all interplaying with the complexities of bedrock surface and permeability below. In a context where lateral flow in the soil layer dominates, this theoretical study showed that downslope topography significantly affects the propensity of a point to retain or release water and therefore alters the flow and storage dynamics of upslope points. Analysis in this chapter allowed to (a) examine the relative effects of advective (i.e., topographic) and diffusive (pressure dependent) flow processes by using a physically based Boussinesq equation solver (BEq), and (b) test the ability of several terrain-based wetness indices to approximate the BEq-derived water storage dynamics.

The results obtained showed that locally-computed topographic wetness indices were not able to account for the role that complex topography plays on storage dynamics. Specifically, they were not able to represent the effect of downslope topography on upslope water flow. Results also highlighted the need to relax the steady-state assumption on which traditional topographic indices are based. The new terrain index (TWI_d^*) applies a 3x3 low-pass filter to a dynamic topographic index (TWI_d) to smooth out the effects of local topography and grid influence on water flow paths (i.e., the artifacts on flow paths connected to the use of a regular grid). The statistical comparison here developed showed that TWI_d^* outperformed previous indices when working with high resolution DEMs, resulting in a less fragmented and disconnected water table configuration. This was achieved without losing the accuracy afforded by high resolution DEMs to describe drainage paths and upslope accumulated area. Moreover, since the TWI_d^* uses the concept of time-variable upslope contributing area, it is not limited by a single value, monotonic function between groundwater storage and runoff

production.

Because many rainfall-runoff models and catchment scale shallow landslide models rely upon these indices to cope with the spatial distribution and the dynamics of soil-water storage in a catchment, TWI_d^* may be a better alternative to the traditional topographic index in describing subsurface flow processes, at least where topography (i.e., lateral flow) is recognized as the predominant control for subsurface flow mechanisms.

Chapter 4

Simulated effect of soil depth and bedrock topography on near-surface hydrologic response and shallow landslide triggering

4.1 Introduction

This Chapter explores the effect of hillslope hydrological behavior on slope stability in the context of transient subsurface saturation development and landslide triggering.

The overarching goal is to answer the question: *how does bedrock topography influence the dynamics of pore pressure development and resulting triggering of shallow landslides?*

In fact, almost all shallow landslide models for use at the basin scale assume that the soil-bedrock interface is a simple topographic surface paralleling the soil surface. As a result, none of the slope stability models have yet included an important new conceptual element derived from the hillslope hydrology literature: the filling and spilling of water perched at the soil-bedrock interface. Indeed the importance of moisture dynamics at the soil-bedrock interface has been widely acknowledged in hillslope hydrology (e.g., Weiler et al., 2005). Recent hydrological analyses by several groups in several different hydrogeological settings (e.g. Spence and Woo, 2003; Buttle et al., 2004; Tromp van Meerveld and McDonnell, 2006b, Graham et al., 2010; Spence, 2010) have shown that filling and spilling of microtopographic depressions in the bedrock topographic surface control the development and connectivity of patches of positive pore pressure. For the hillslope hydrologist, these patches and their downslope connectivity, form the precondition for resultant subsurface stormflow (Tromp van Meerveld and McDonnell, 2006a). This behavior is now viewed as dominant subsurface stormflow delivery mechanism whereby the existence of a threshold relationship between rainfall amount and hillslope outflow appears to be a common property of hillslope drainage (see review in Weiler et al., 2005). For the slope stability modeler, these patches appear to be a key, unstudied part of the landslide initiation process with potential first order hydrologic control on where a slip surface might be found.

In this Chapter, a series of virtual experiments (Weiler and McDonnell, 2004) are performed

to address how subsurface topography affects the location and spatial pattern of slip surface development and pore pressure dynamics.

The Panola hillslope hydrological research site (Freer et al., 2002) is used as a virtual laboratory to explore how soil depth, slope inclination and other factors conspire to trigger shallow landslides. A number of sub-questions are also addressed:

1. *How does the subsurface topography affect the location and spatial pattern of slip surface development?*
2. *How does local and slope-averaged slope angle influence maximum pore pressure and temporal and spatial extension of transient saturation at the soil bedrock interface?*
3. *How does rainfall amount and intensity affect development of positive pore pressure at the soil-bedrock interface of steep hillslopes?*
4. *How does bedrock topography influence the size and shape of the triggered area?*

This work build upon the work of Hopp and McDonnell (2009) where the 3D Darcy-Richards equation solver (Hydrus 3-D by Simunek et al., 2006) is used to quantify patterns of pore pressure development. Output from Hydrus 3-D are linked to a slope stability model that builds upon a modified version of the cellular automata model (CA) presented in Piegari et al. (2009). The CA model here presented simulates the spatial propagation of the destabilized area providing an estimation of the hillslope area on the verge of collapse.

This work has been provisionally accepted for publication as: Lanni C, McDonnell JJ, Hopp L, Rigon R. 2012. Simulated effect of soil depth and bedrock topography on near-surface hydrologic response and shallow landslide triggering. in *Earth Surface processes and Landforms*.

4.2 The Panola trench hillslope

The Panola experimental hillslope is used as a shell for the virtual experiments presented in this study. The Panola hillslope has a slope angle of 13° , is 28 m wide and 48 m long and lies within the Panola Mountain Research Watershed (PMRW), located about 25 km southeast of Atlanta, Georgia, USA, in the southern Piedmont. The site is described in detail by Tromp-van Meerveld and McDonnell (2006a, 2006b) and the reader is referred to those papers for further details. The downslope boundary of the Panola hillslope is formed by a 20 m wide trench. The upper boundary of the study hillslope is formed by a small bedrock outcrop. Soil depths on the study hillslope have been measured on a regular 2x2 m grid and linearly interpolated to a 1x1 m digital elevation model. The surface topography of the study hillslope is largely planar while the bedrock topography is very irregular (Figure 4.1a), resulting in highly variable soil depth across the study hillslope ranging from 0 to 1.86 m with an average value of 0.63 m (Figure 4.1b).

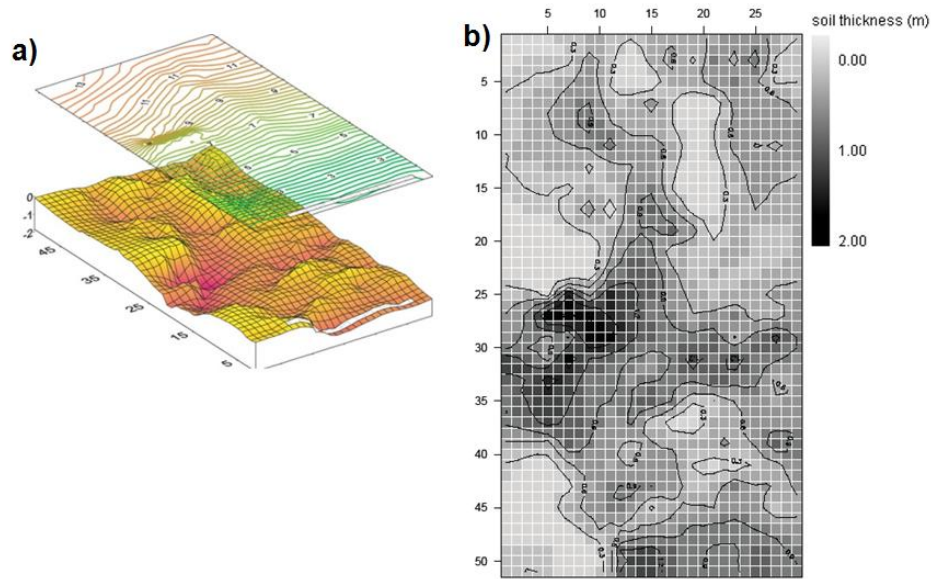


Figure 4.1. Irregular bedrock surface vs regular ground surface at the Panola hillslope (a), and soil depth variability (b)

The soil on the study hillslope is a sandy loam without clear structuring or layering, except for a 0.15 m deep organic-rich soil horizon. The soil is classified as the coarse, loamy, mixed thermic Typic Dystrochrepts from the Ashlar series. There are not observable differences in soil type across the study hillslope. The climate is humid and subtropical with a mean annual air temperature of 16.3°C and mean annual precipitation of 1240 mm, spread uniformly over the year (NOAA, 1991). Rainfall tends to be of long duration and low intensity in winter, when it is associated with the passage of fronts, and of short duration but high intensity in summer, when it is associated with thunderstorms (Tromp-van Meerveld and McDonnell, 2006a). Overland flow is uncommon at PMRW and is observed only during very intense thunderstorms after extended dry periods. Even during these storms, overland flow was restricted to small areas and re-infiltrated within several meters.

4.3 Methods

4.3.1 The hydrological response model and the hillslope stability model

The Hydrus-3D hydrological model (Simunek *et al.*, 2006) was used to compute water movement in unsaturated/saturated soil and to provide the 3-dimensional pore-pressure field input to the slope stability model. Hydrus 3-D can accommodate flow domains with irregular geometries like that of the Panola hillslope. It solves the Richards' Equation (2.6) presented in Chapter 2.

For mechanical behavior of the Panola soils, a rigid and perfectly-plastic soil behavior is assumed. According to the modified Bishop's criterium (1959) proposed by Lu and Likos (2006), the soil-shear strength τ [FL^{-2}] can be expressed as:

$$\tau = c' + [(\sigma - p_a) - \sigma^s] \cdot \tan \phi' \quad (4.1)$$

Where c' [FL^{-2}] is the effective soil cohesion, σ [FL^{-2}] is the total stress, p_a [FL^{-2}] is the pore-air pressure, ϕ' is the effective soil frictional angle, σ^s is defined as the suction stress characteristic curve of the soil with a general functional form of:

$$\sigma^s = -(p_a - p_w) \quad \text{if } (p_a - p_w) \leq 0 \quad (4.2a)$$

$$\sigma^s = f(p_a - p_w) \quad \text{if } (p_a - p_w) > 0 \quad (4.2b)$$

where p_w [FL^{-2}] is the pore-water pressure. This criterion allows the contribution of negative pore-water pressure (suction) on soil shear strength to be taken into account.

The suction stress characteristic curve, σ^s , can also be expressed in terms of effective saturation degree or normalized volumetric water content following Vanapalli et al. (1996):

$$\sigma^s = -\frac{\theta(\psi) - \theta_r}{\theta_{sat} - \theta_r} (p_a - p_w) = -S_e (p_a - p_w) \quad (4.3)$$

where S_e [-] is the relative saturation degree, θ [-] is the actual water content, θ_{sat} [-] is the saturated water content, and θ_r [-] is the residual water content.

The factor of safety FS provides a measure of slope stability. FS is given by the ratio between maximum retaining forces, F_r , and driving forces, F_d :

$$FS = \frac{F_r}{F_d} \quad (4.4)$$

Simply put, the slope is considered stable for $FS > 1$, while slope failure occurs when the critical state $FS = 1$ (such that $F_r = F_d$) is achieved. As revealed from the literature review (Chapter 2), the infinite slope stability hypothesis has been widely applied in many investigations of natural slope stability (e.g., Montgomery and Dietrich, 1994; Wu and Sidle, 1995; Vanbeek et al., 2002; Borga et al., 2002; D'Odorico et al., 2005; Casadei et al., 2003; Lu and Godt, 2008) because of its relative simplicity, where the thickness of the soil mantle is much smaller than the length of the slope.

Assuming $p_a = 0$ in Equations (4.1), (4.2) and (4.3), the factor of safety of an infinite slope model that accounts for saturated/unsaturated zones can be written as:

$$FS = \frac{2c'}{\gamma z \sin(2\beta_i)} + \frac{\tan \phi'}{\tan \beta_i} + \frac{\gamma_w \Psi}{\gamma z} (\tan \beta_i + \cot \beta_i) \tan \phi' \quad \text{for } \psi \leq 0 \quad (4.5a)$$

$$FS = \frac{2c'}{\gamma z \sin(2\beta_i)} + \frac{\tan \phi'}{\tan \beta_i} + S_e(\psi) \frac{\gamma_w \Psi}{\gamma z} (\tan \beta_i + \cot \beta_i) \tan \phi' \quad \text{for } \psi > 0 \quad (4.5b)$$

where β_i [°] is the local slope angle, \bar{z} [L] is the vertical soil-depth, γ_w and γ and [FL⁻³] are the volumetric unit weight of water and soil, respectively.

A cellular automata (CA) model (see Bak et al., 1987; Rodriguez-Iturbe and Rinaldo, 1997; Jensen, 1998 for a review) is then used to propagate instability starting from pattern of instability provided by the infinite slope stability model.

CA is conceptually related to raster GIS because it models the space by tessellating it into regular, discrete locations and assigning attributes to each location. An individual cell can be viewed as a unique location within the grid. Raster GIS data can be associated with the states of the automaton and represent the spatial information on which the model works. A cell's state will change according to transition rules that apply simultaneously to every cell in the space. These rules are based on both the current state of the cell under study and also the state of its neighbors. CA models have been largely used to model landslide propagation for regional landslide characterizations that exhibit self-organized critical states (Avolio et al., 2000; Clerici and Perego, 2000; Turcotte et al., 2002; D'Ambrosio et al., 2003; Iovine et al., 2003; Guthrie et al., 2007).

The CA model used in this study is a modified version of the CA model presented by Piegari et al. (2009). Piegari et al. (2009) accounted for the effect of the triggering factor (i.e., rainfall) on the value of factor of safety (FS) by introducing an empirical parameter ν that controlled the rate at which all sites were driven towards instability. Here, the modified CA model uses the pore pressure dynamics simulated by Hydrus 3-D to account for the effect of rainfall on landslide triggering.

The present work adopt a scheme where the solid and fluid sub-problems are uncoupled and the patterns of FS are re-initialized at each time step on the base of the FS configuration provided by the infinite slope stability model. More specifically, when a raster-cell i becomes unstable (i.e., $FS_i \leq 1$ according to the infinite slope stability model), it affects, via a chain reaction, the stability of the 8 neighboring cells i_{nn} , by reducing their driving forces, $F_d^{i_{nn}}$, of a fraction λ of the driving forces of the destabilized cell i , F_d^i :

$$FS_{i_{nn}} = \frac{F_r^{i_{nn}}}{F_d^{i_{nn}} + \frac{1}{8} \lambda F_d^i} \quad \text{with } nn=1, \dots, 8 \quad (4.6)$$

where $FS_{i_{nn}}$ and $F_r^{i_{nn}}$ with $nn=1, \dots, 8$ are the safety factors and the retaining forces of the 8

neighboring, respectively.

In Equation (4.6) the fraction $1/8$ indicates that the destabilizing forces F_d^i of the unstable cell i are redistributed equally among the neighboring cells i_{nn} . The parameter λ is a parameter that determines the degree of conservation of the system. $\lambda=0$ means that the system is completely dissipative (i.e., the destabilized locations do not affect the stability of the neighboring cells), while $\lambda=1$ means that the system is completely conservative (i.e., the destabilizing forces of destabilized locations are completely transferred to neighboring cells). Here, it is assumed $0 < \lambda < 1$ by considering a non-conservative case, since many complex dissipative phenomena can contribute to stress transfer processes (Fredlund and Rahardjo, 1993). The chain reaction continues until no unstable locations are generated, according to the flow chart of Figure 4.2.

This simplified model was used to propagate instability and to provide an estimation of the most likely landslide initiation zones on the hillslope.

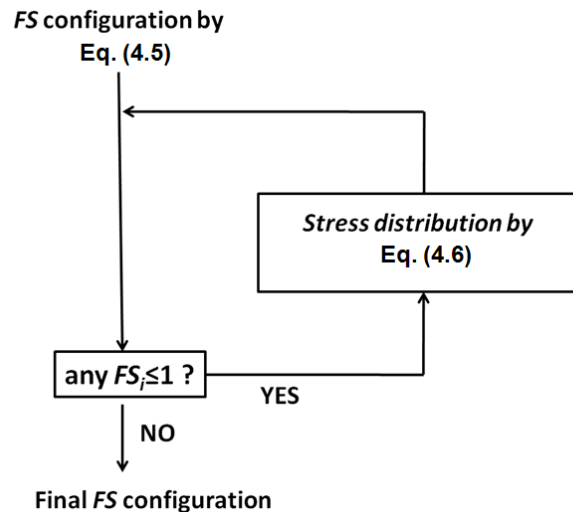


Figure 4.2. Flow chart of the cellular automata model. The stress is propagated until no new unstable locations are generated. The final FS configuration gives an estimation of the most likely hillslope portion to be affected by landslide activation

4.3.2 Hydrological and mechanical characterization

Hopp and McDonnell (2009) evaluated Hydrus 3-D's ability to represent measurements of pore-pressure recorded by tensiometers at several points in the Panola hillslope (detailed information on the field data can be found in Freer et al., 2002). Here, the same soil water retention and hydraulic conductivity functions as Hopp and McDonnell (2009) have been used. These are described using the van-Genuchten-Mualem model presented in Chapter 2 - Equations (2.7) and (2.8).

The soil mantle was divided into three layers to account for the observed reduction of

saturated hydraulic conductivity K_{sat} in the profile. Saturated hydraulic conductivity of the bedrock saprolite was approximated based on measured values reported in Tromp-van Meerveld et al. (2007). Table 4.1 shows the hydrological parameters used in this study to characterize both soil and the bedrock material of the Panola hillslope. For our virtual experiments, we set the saturated hydraulic conductivity at the contact between soil and bedrock to be three orders of magnitude less than the soil K_{sat} .

Both the water retention function and the hydraulic conductivity function of the soil material and bedrock saprolite exhibit a steep slope near zero pressure head. In particular, the soil hydraulic conductivity $k(\psi)$ increases drastically near zero pressure head in a short range of suction head ψ (about 0.5 m).

We used empirical relationships (by Terzaghi et al., 1996) to estimate the effective frictional angle ($\phi'=34^\circ$) and the effective cohesion ($c'=0$ kPa) of the sandy loam soil of Panola hillslope. The bedrock layer was considered stable in our experiments because of the good mechanical characteristic of the saprolite rock.

Table 4.1: Average soil thickness $\overline{\Delta z}$ and hydrological parameters of the soil and saprolite bedrock layers of Panola Hillslope (from Hopp and McDonnell, 2009)

<i>Material</i>	$\overline{\Delta z}$ (cm)	θ_r (-)	θ_{sat} (-)	α (m^{-1})	n (-)	K_{sat} (ms^{-1})
Soil	15	0.28	0.475	4.0	2	10^{-3}
	10	0.28	0.46	4.0	2	$4 \cdot 10^{-4}$
	38	0.325	0.45	4.0	2	$1.8 \cdot 10^{-4}$
Bedrock	-	0.30	0.45	3.25	2	$1.7 \cdot 10^{-7}$

4.3.3 Virtual experiment design

The geometrical domain of Panola hillslope was implemented in Hydrus 3-D where a finite element mesh of triangular prisms with 35600 nodes and 64638 3D-elements was generated. On this geometry, eight experiments that included three different slope angles β (13° - i.e., the original Panola hillslope inclination, 20° , and 30°) and four different rainfall events were conducted. Each rainfall event was spatially and temporally uniform. These events were characterized by the same cumulative rainfall, but different distribution in time (i.e., different values of rainfall intensity and duration). Two rainfall scenarios (*long-rainfall* and *short-rainfall* in Table 4.2) were selected for the virtual experiments with the lower slope angles ($\beta = 13^\circ$ and $\beta = 20^\circ$). Two events (*very long-rainfall*, and *very short-rainfall* in Table 4.2) were also analyzed in the steepest hillslope case ($\beta = 30^\circ$).

Table 4.2: The hillslope angles and rainfall event features used in the virtual experiments. I = rainfall intensity; D = rainfall duration.

		<i>Rainfall event</i>			
		<i>Very short</i>	<i>Short</i>	<i>Long</i>	<i>Very long</i>
		I = 20 mm/h D = 3 h	I = 12 mm/h D = 5 h	I = 6.25 mm/h D = 9 h	I = 5 mm/h D = 12 h
Overall slope angle β	13°		x	x	
	20°		x	x	
	30°	x	x	x	x

These three hillslope inclinations ($\beta = 13^\circ$, $\beta = 20^\circ$, and $\beta = 30^\circ$) allowed to investigate how the overall slope angle influences the maximum pore-pressure values, the spatial extension and level of connectivity of patterns of transient saturation at the soil-bedrock interface, and the temporal persistence of these. Despite these overall slope angle comparisons, the local slope values, $\tan\beta_i$, of the bedrock topography (i.e., at the soil-bedrock interface) in any given pixel was highly variable and often larger than the overall slope angle $\tan\beta$. For example, β_i ranged from 6° to 57° at the steepest ($\beta = 30^\circ$) hillslope configuration. Hence, because of the soil mechanical properties of the sandy loam soil ($\phi' = 34^\circ$ and $c' = 0$ kPa) and according to Equation 4.5, some points would achieve instability under positive pore pressure (i.e., where $\tan\beta_i < \tan\phi'$) and some others would achieve instability under negative pore pressure (i.e., where $\tan\beta_i > \tan\phi'$).

Initial conditions for the virtual experiments were set to a relatively dry state (with low unsaturated hydraulic conductivity values) which reproduces the antecedent soil-moisture condition generally observed at the Panola hillslope (Tromp van Meerveld et al., 2007) before of a rainfall event. The initial mean soil-water content was $\theta = 0.32 \text{ cm}^3 \text{ cm}^{-3}$, with initial pressure head ψ ranging from -1.0 to -0.7 m linearly distributed with depth. This relative dry state ensured that: (i) numerical results were not affected by the unbalanced initial conditions, such that modification in pore-pressure regime was only due to the effect of rain infiltration; (ii) the factor of safety, FS, of the steepest hillslope configuration ($\beta = 30^\circ$) was greater than 1 in each point of the hillslope before of the beginning of rainfall. Boundary conditions of the geometrical domain were the following: atmospheric boundary (i.e., rainfall rate) at the soil surface (i.e., upper boundary of the numerical domain), potential seepage face boundary at the downslope end of the hillslope (the face was treated as a prescribed pressure head boundary with $\psi = 0$, while the unsaturated part was treated as a no-flux boundary), free drainage boundary at the bottom boundary of the numerical domain (it was imposed a unit gradient of the total head and therefore the flux was equal to the hydraulic conductivity for any particular pressure head at given time), and no-flux boundary at the upslope and side

boundaries.

4.4 Results

4.4.1 The role of bedrock topography on pore pressure development and integrated hydrological response

Figure 4.3 shows the temporal evolution of pressure head at the soil-bedrock interface for the base case 13°-Panola hillslope during the *long-rainfall* event ($I=6.25 \text{ mmh}^{-1}$, $D=9 \text{ h}$ in Table 4.2). Well-connected patches of saturation developed after 9 hours from the onset of rainfall. The mid-slope zone was characterized by the main bedrock depression (Figure 4.1), and exhibited the highest pore-pressure values (with a maximum value of 0.69 m). The hillslope hydrograph from the slope base is also shown in Figure 4.3 (right-hand side), where the shaded portions correspond to the time periods of pore pressure development.

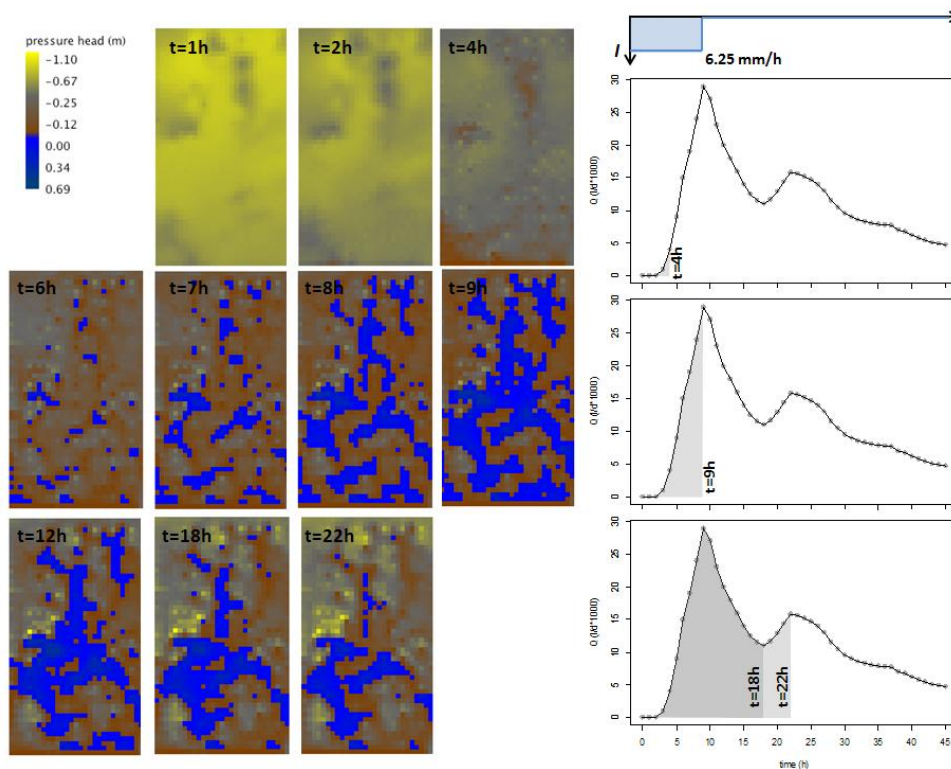


Figure 4.3. Patterns of transient saturation at the soil-bedrock interface of the original 13° Panola hillslope for distinct time steps in the hillslope hydrograph (shaded right-hand side of the figure) for several hours during the *long-rainfall* event. The blue zones represent the patches of transient saturation (perched water table); the yellow, grey and brown colors identify variably unsaturated soil conditions. Flow is concentrated in the mid-slope which exhibits the highest pore pressure values

The hillslope hydrograph shows a double peak: the first at the end of the long-rainfall event

(9th hour), the second 13 hours after the end of this rainfall (22nd hour). The minimum value of discharge between these two peaks is localized around the 18th hour (9 hour after the end of the event). The second peak is due to the spilling of water from the main-bedrock depression that was filled during the drainage following the initial rainfall burst.

4.4.2 Relation between hillslope gradient and spatio-temporal extent of transient saturation at the soil-bedrock interface

Figure 4.4 describes the relation between hillslope gradient and spatio-temporal extent of transient saturation at the soil-bedrock interface for the *long-rainfall* event ($I=6.25 \text{ mmh}^{-1}$ and $D=9 \text{ h}$).

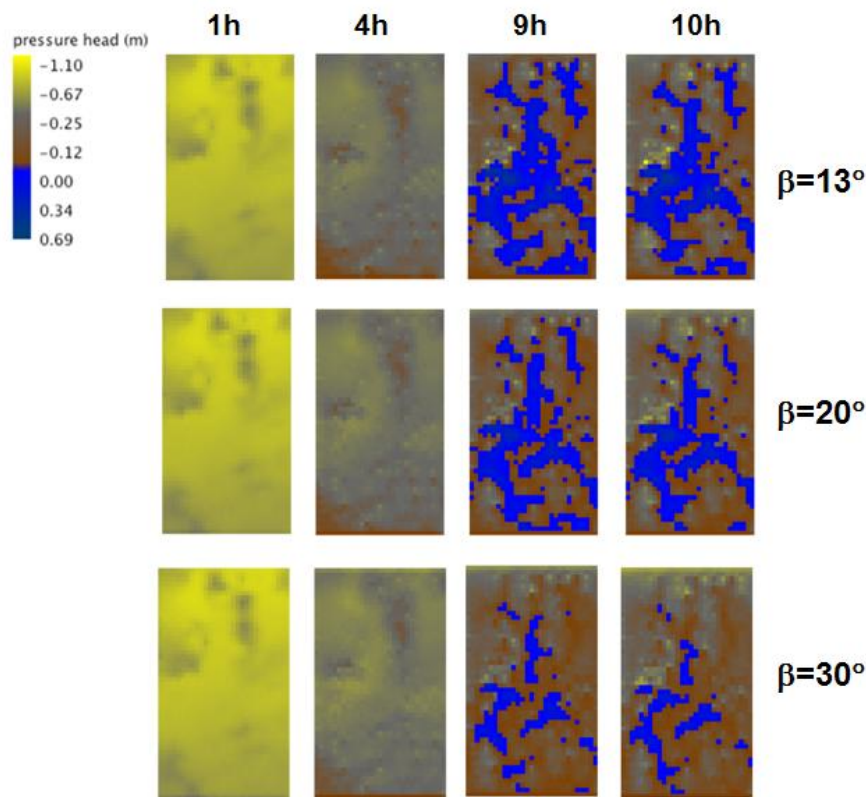


Figure 4.4. Maps of pore pressure at the soil bedrock interface of the original 13° Panola hillslope (first row), and the modified 20° and 30° Panola hillslopes (second and third rows, respectively) for the long-rainfall event. Maps of pore-pressure are quite similar during the first stage of rainfall (the maps of 1st hour and 4th hour are showed in the first and second columns, respectively), while the overall inclination significantly affects the dynamic of pore pressure in the second stage of rainfall (the maps of 9th hour and 10th hour are showed in the third and fourth columns, respectively) when lateral flow becomes relevant

An increase in overall slope angle β lead to a general decrease in the extension and connectivity of saturated areas and their temporal persistence at the soil-bedrock interface. This finding is consistent with Hopp and McDonnell (2009). Despite the slope angle influence, the maximum value of pressure head (0.69 m) was not affected by the slope inclination. During the first stage of rainfall (at approximately 4-5 hours), pore pressure maps at the soil bedrock interface of 13°, 20° and 30° slope angles showed similar patterns (first and second columns in Figure 4.4). The maps of pore pressure resemble the map of soil depth (shown in Figure 4.1) with areas characterized by the thinnest soils responding first to the precipitation input.

Figure 4.5a shows the temporal evolution of the transient saturation area at the soil-bedrock interface for the three slope angles during the *long-rainfall* event. The size of saturated area is expressed in terms of percentage of the total hillslope area. For all the investigated hillslope inclinations, perched water table developed shortly after 4-5 hours from the beginning of the rainfall. The maximum size of saturated area reached 40% of the total hillslope area for the 13° hillslope, and 13% of the total hillslope area for the 30° hillslope. The time of persistence of this transient saturation was drastically reduced for the steepest hillslope. In fact, while the original 13° Panola hillslope still exhibited transient water-table at the soil-bedrock interface after three days of drainage, only 50 hours and 28 hours of drainage were necessary to dissipate positive pressure heads at the soil-bedrock interface for the modified 20° and 30° hillslopes, respectively.

In Figure 4.5b, the average value of positive pore pressures developed at the soil-bedrock interface is plotted against the percentage of saturated area. The maximum size of saturated area at the soil-bedrock interface of the original 13° hillslope was achieved at the end of the event (9th hour). However, the average value of positive pore pressures continued to increase after the end of the event with the concomitant decrease of saturated area. The average value of positive pore pressures and saturated area extension both decreased from the 14th hour onwards. The same behavior was also observed for the modified 20° and 30° hillslopes (with reduced time-lag between maximum saturated area and maximum value of average value of positive pore pressures), and for the other rainfall events (Table 4.2) analyzed.

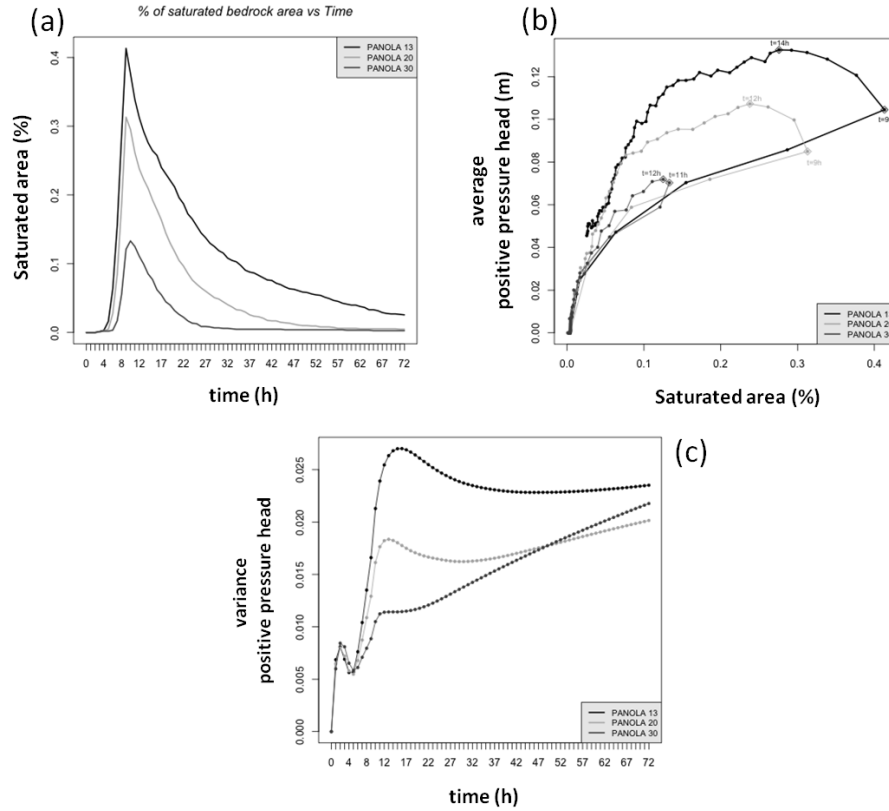


Figure 4.5. Saturated area and pressure head response for the *long-rainfall* event. (a) Temporal evolution of saturated area at the soil-bedrock interface of the original 13° and modified 20° and 30° Panola hillslopes during the *long-rainfall* event. (b) Dynamics of the mean value of positive pressure head versus percentage of saturated area at the soil-bedrock interface for the three analyzed Panola hillslope angles. (c) Temporal evolution of the variance σ_{ψ}^2 of the values of pressure head recorded at the soil-bedrock interface for the three slope angles investigated

4.4.3 When does slope angle affect the dynamics of subsurface flow and pore pressure development?

Pore-pressure rise at the soil-bedrock interface was inversely related to soil depth during the first rainfall-hours for all the three hillslope inclinations analyzed. During this first phase, rain infiltration was strictly vertical and no differences were found for the three analyzed hillslope angles ($\beta=13^\circ, 20^\circ, 30^\circ$). Figure 4.5c shows the evolution of the variance of the values of pressure head at the soil-bedrock interface $\sigma_{\psi}^2(t)$ during the *long-rainfall* event. $\sigma_{\psi}^2(t)$ is defined as follow:

$$\sigma_{\psi}^2(t) = \frac{1}{N} \sum_{i=1}^N (\psi_i(t) - \bar{\psi}(t))^2 \quad (4.7)$$

where N is the total number of nodes of the numerical-domain at the soil-bedrock interface (1479 points), ψ_i [L] is the value of suction head at node i , $\bar{\psi} = 1/N \cdot \psi_i$ is the average value of pressure head at the soil-bedrock interface, and t [T] is a generic time.

Equation (4.7) describes how much localized pore pressure values deviate from the average value of pressure head at the soil-bedrock interface. Therefore, it provides a measure of the spatial variability of pore pressure during and after the rainfall event. The initial value of the variance of pressure head at the soil-bedrock interface, $\sigma_{\psi}^2(t=0)$, was zero because all the nodes were characterized by the same pore-pressure value before the beginning of the *long-rainfall* event. $\sigma_{\psi}^2(t)$ increased after the beginning of the event, indicating a different response of the bedrock-points to the rainfall input. The $\sigma_{\psi}^2(t)$ of the three investigated hillslope angles (13° , 20° , and 30°) were very similar until the 5th rainfall-hour. $\sigma_{\psi}^2(t)$ then diverged in the successive phases of the rainfall event. Hence, the hillslope gradient affected the pore pressure dynamics in the second phase of rainfall (4-5 hours after rainfall commencement). In particular, the lower the overall hillslope angle β , the higher the variance of pressure head recorded at the soil-bedrock interface. This was basically related to the different (lateral) subsurface flow velocities in dissipating the positive pore pressure during the second phase of rainfall and after the end of the rainfall event.

All the investigated slope angles showed a double peak in the shape of $\sigma_{\psi}^2(t)$ (Figure 4.5c). The second peak occurred always after the end of the event (15th hour, 13th hour, and 12th hour for the 13° -, 20° -, and 30° -Panola hillslope, respectively).

Figure 4.6 shows the maps of pressure head at the soil bedrock interface for the modified 30° Panola hillslope during the *short-rainfall* ($I = 12 \text{ mmh}^{-1}$, $D = 5 \text{ h}$) and the *long-rainfall* ($I = 6.25 \text{ mmh}^{-1}$, $D = 9 \text{ h}$) events. The maps are arranged in order of increasing amounts of cumulative rainfall. For both the *short-* and *long-rainfall* events a threshold of about 35 mm of rainfall was necessary to generate measurable spots of transient saturation at the soil-bedrock interface. Once this threshold was exceeded a rapid propagation of transient saturation extent was then observed. The rainfall intensity I affected the temporal dynamics of this process but, irrespective of rainfall intensity, similar patterns of pore pressure were observed for the same total rainfall amount.

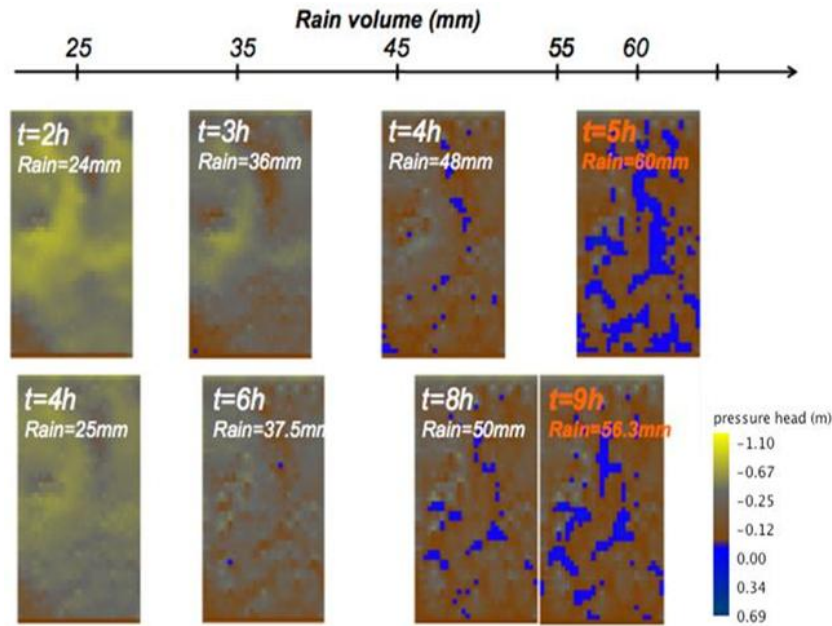


Figure 4.6. Maps of pore-pressure at the soil-bedrock interface of the modified 30°-Panola hillslope during the *short-rainfall* (top) and *long-rainfall* (bottom) events. Patterns of pore pressure are similar when the same value of cumulative rainfall has been achieved

4.4.4 Linking subsurface hydrology and landslide triggering

The pore pressure values provided by Hydrus 3-D were used to compute the factor of safety FS in each soil-pixel by applying the infinite slope stability model developed in Equation (4.5). This allowed calculation of the factor of safety at each depth of the discretized domain. Only the steepest hillslope scenario ($\beta=30^\circ$) was affected by conditions of instability (i.e., raster cells where FS dropped below 1). In particular, the slip surface (i.e., the depth of failure) was always localized at the soil-bedrock interface where FS first dropped below 1.

The CA model (flow chart in Figure 4.2 and Equation 4.6) was used to redistribute the driving forces of the unstable pixels to the neighboring regions within the hillslope domain and thus outline the hillslope zones on the verge of collapse. Figure 4.7 shows the patterns of unstable points for the 30°-hillslope at several times during the *long-rainfall* event. Red points represent unstable locations provided by the infinite slope stability model (Equation 4.5). The black points are ones that become unstable when the driving forces of the destabilized locations are redistributed to the neighboring cells (Equation 4.6). The patterns of instability were evaluated by using four different values of the failure propagation rate λ (i.e., the percentage of driving forces redistributed to the neighbors): 0.2, 0.4, 0.6 and 0.8.

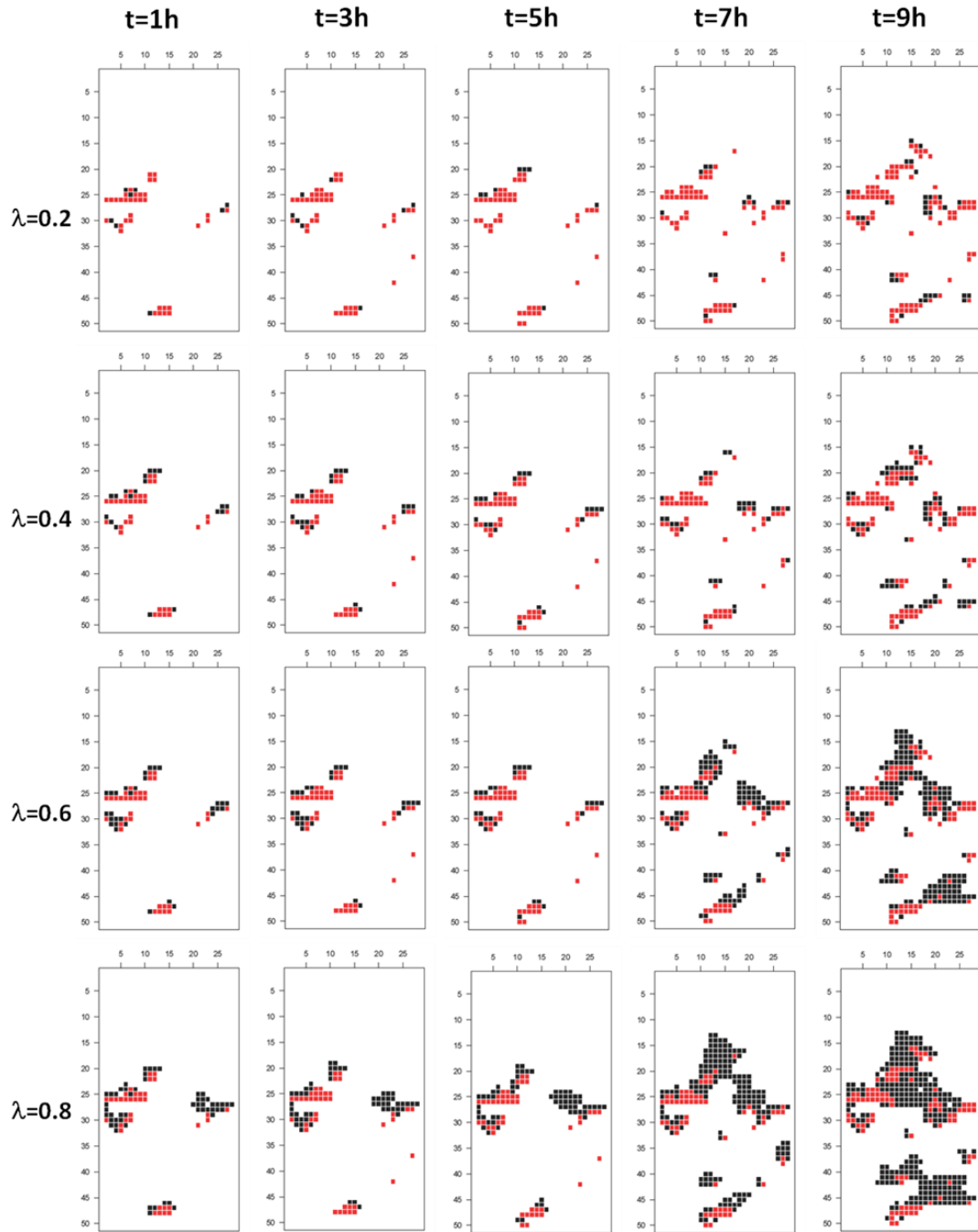


Figure 4.7. Temporal patterns of unstable locations generated by the cellular automaton (CA) model for four different values of λ (0.2, 0.4, 0.6, and 0.8 on the first, second, third and fourth row, respectively). The *long-rainfall* event case ($I=6.25$ mm/h, $D=9h$) is here shown. In red are the points classified unstable by the infinite slope stability model (Equation 4.5). The black points are the ones that become unstable when the driving forces of the destabilized locations are redistributed to the neighboring cells (Equation 4.6). Rapid failure propagation is observed for high values of λ ($\lambda=0.6$ and $\lambda=0.8$) during the second stage of rainfall event (i.e., after 5 hours from rainfall beginning)

Maps of instability in Figure 4.7 show two large clusters of instability with centers localized approximately 25 and 45 m downslope from the crest of the hillslope. Patterns of instability did not exhibit significant differences during the first rainfall hours and λ had only a small effect on where failure occurred (i.e. the maps in the 1st, 2nd, and 3rd columns in Figure 4.7 are very similar). On the other hand, instability spread very quickly in the second phase of rainfall (approximately 6-7 hours after the onset of rainfall) especially when the higher values of λ ($\lambda=0.6$ and $\lambda=0.8$) were used to run the CA model. This threshold-like expansion behavior was also observed for the other rainfall events analyzed (*very short*-, *short*-, and *very long*-rainfall events in Table 4.2), where the time at which the threshold expansion behavior was observed decreased with increasing rainfall intensity.

Figure 4.8 shows that instability spread very quickly when a cumulative rainfall of 30-35 mm was achieved, irrespective of rainfall intensity. Once this rain amount was exceeded a rapid propagation of instability was then observed. This precipitation threshold was similar for all the values of λ considered.

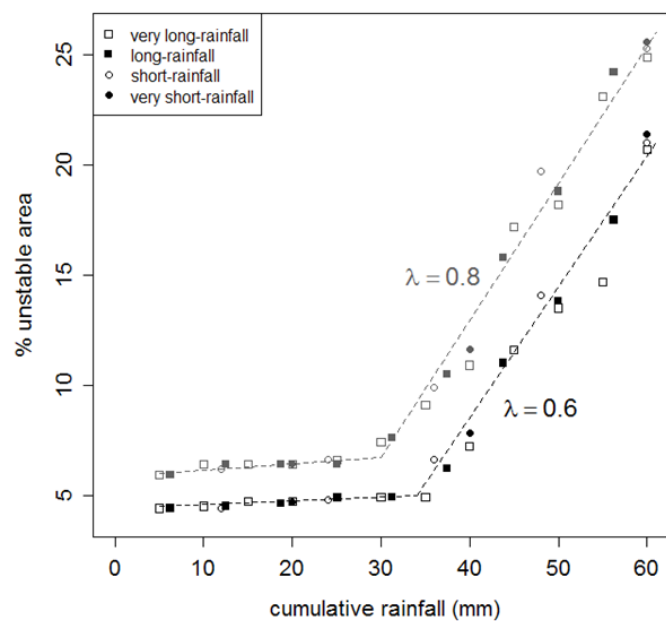


Figure 4.8. Cumulative rainfall against % of unstable area provided by the CA model for all the rainfall events analyzed. Instability spread very quickly when a cumulative rainfall of 30-35 mm was exceeded

4.5 Discussion

Many of today's popular landslide initiation models used to map landslide triggering assume that the DEM of the ground surface is a good proxy to describe subsurface pore pressures and flow path dynamics or to characterize the initial conditions for soil-water storage prior to rainfall events (e.g., Baum et al., 2008). These models generally use the DEM of the ground

surface to compute a steady-state (e.g., Montgomery and Dietrich, 1994; Wu and Sidle, 1995; Pack et al., 1998) or a ‘quasi-dynamic’ wetness index (Borga et al., 2002; Casadei et al., 2003) where it is assumed that the specific (steady-state or time-variable) upslope area derived from the surface topography is a surrogate measure of subsurface flow in response to a rainfall of specified duration. The subsurface flow paths (i.e., the drainage directions) are derived from DEM analysis and the land surface slope is used as a substitute for the slope of the hydraulic gradients.

The results of this study showed that subsurface topography, not surface topography, controls the development of perched water table during rainfall events and that bedrock depressions are the zones primarily responsible for localized pore pressure increases. These findings are consistent with the preponderance of evidence from many study hillslopes around the world (as reviewed in Weiler et al., 2005). The filling and spilling of water in this zone may be a first order effect on the generation of shallow landslide triggering.

4.5.1 On the relation between bedrock topography and the development of positive pore pressure

The bedrock topography induced the development of positive pore pressure at the soil-bedrock interface. Filling and spilling of water in this zone determined the temporal evolution and the connectivity of zones of transient saturation at the soil-bedrock interface of the Panola hillslope. Rain water infiltrated vertically through the soil profile during the first stage of rainfall due to the high infiltration soil capacity of the Panola-soil. The first bedrock points to respond to the precipitation input were those with the thinnest soil above the bedrock level, where a temporary perched water table developed and water began to move laterally. The initially fragmented patches of transient saturation became more connected as the water table rose high enough that water spilled over the ridges of isolated bedrock micro-depressions. The main bedrock depression on the midslope (see the soil depth map in Figure 4.1) represented a major depression and was responsible for the slope-wide increase of the average value of positive pore pressures.

The slope-averaged value of positive pore pressure decreased when the water level in the bedrock depression rose high enough so that water spilled over the bedrock ridge. This macro spillage determined the second peak of the hydrograph after the end of the *long-rainfall* event (Figure 4.3), and the second peak of the variance σ_{ψ}^2 of the pore pressure values at the soil-bedrock interface observed after the end of the *long-rainfall* event (Figure 4.5c).

The dynamics of filling and spilling were strongly affected by the hillslope gradient. The fill and spill mechanism transitioned from a fill-dominated system at 13° to a spill-dominated system at 30°. The higher the hillslope gradient, the lower the spatial extension and temporal persistence of transient saturation at the soil-bedrock interface were (Figures 4.4 and 4.5a). While these general findings follow Hopp and McDonnell (2009), the stability-based

analysis of this work showed that in the first phase of rainfall, the three investigated hillslope angles ($\beta=13^\circ$, $\beta=20^\circ$, $\beta=30^\circ$) exhibited similar patterns of pore-pressure. In this first phase, flow only occurred vertically through the soil profile because of the high vertical gradient of pressure head. The hydrological response of the three hillslope angles changed only in the second phase of the rainfall event, when the infiltration front reached the poorly permeable soil-bedrock interface and positive pore pressures developed. As observed in many studies, the break in vertical permeability between soil and bedrock materials was a key driver for lateral flow generation (see early work by Weyman, 1973, and later review in Weiler et al., 2005). This positive pore pressure development induced an increase in the hydraulic conductivity of two to three orders of magnitude at the soil-bedrock interface and subsequent high increase in lateral flux. Torres et al. (1998) argued that this behavior is typical of coarse-soil with a steep, non-linear hydraulic conductivity function $k(\psi)$ near zero pressure head. A very large increase in hydraulic conductivity and lateral flow is observed when a threshold suction head value is exceeded. This explains the very similar values of the variance of pressure head at the soil-bedrock interface observed during the early rainfall-hours for all the three hillslope gradients analyzed (Figure 4.5c), and the subsequent different dynamics when the magnitude of lateral flow become strongly affected by the hillslope inclination.

4.5.2 On the interaction of subsurface topography, hillslope hydrology and landslide triggering

Development of pressure head at the soil-bedrock interface of Panola hillslope during the second phase of rainfall (i.e., when lateral flows become relevant) was influenced by the bedrock micro-topography. Figure 4.9 illustrates this hydrological behavior schematically for the mapped Panola hillslope geometry (Figures 4.9a and 4.9b), compared to a planar hillslope of same dimension and mean soil depth (Figures 4.9c and 4.9d). Numerical simulation (with Hydrus 3-D) obtained by setting the same boundary and initial conditions as for the “irregular” Panola hillslope showed that in the planar case, a saturated wedge developed at the slope base and expanded upslope as described in Weyman (1973; 1974 and subsequent studies). The pore pressure increases moved downslope with increasing wetness and were directly related to the upslope contributing area. This schematic representation (pore pressure head directly related to the upslope contributing area) underlies most of today’s topographic index-based landslide models (e.g., Montgomery and Dietrich, 1994; Borga et al., 2002). The resulting slip surface then forms starting from the hillslope toe and propagates upslope. On the other hand, transient saturation at the Panola hillslope (Figures 4.9a and 4.9b) is accomplished via a combination of subsurface saturation in shallow soil areas and subsurface saturation in the bedrock depressions (located on the midslope). Maximum pore pressure increases are localized in the bedrock depression, where the factor

of safety is then affected most. Unlike the planar slope, unstable areas are localized near the main depression on the midslope and where the bedrock surface exhibits the steepest local topography (Figure 4.7), and pore pressure fields are weakly correlated with the upslope contributing area calculated from the digital elevation model (DEM) of the bedrock surface.

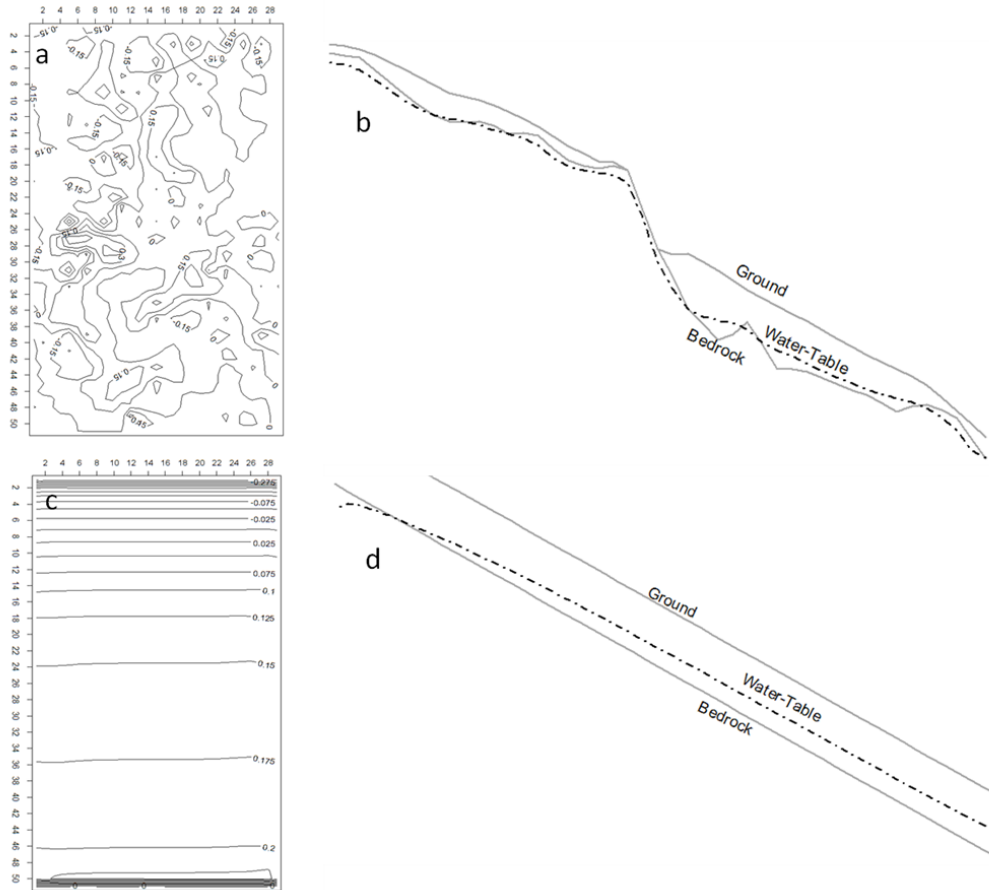


Figure 4.9. A comparison between the hydrological behavior of the “irregular” Panola hillslope and a “regular” planar hillslope. Both slopes received an input of 6.25 mmh^{-1} over 9 hours. Panels (a) and (c) show the pressure head lines (at the 9th rainfall-hour) at the soil-bedrock interface of the irregular and regular slopes, respectively. A saturated wedge expands upslope from the hillslope toe in the planar case (d). Roughness at the bedrock topography of the Panola hillslope (b) induce localized increase in pressure head (by preventing the free downslope drainage) resulting in complex patterns of instability (Figure 4.7). The vertical dimensions in panels (b) and (d) are exaggerated differently

The steepest hillslope (the modified 30°-Panola hillslope) was the only slope representation to exhibit failure during the investigated rainfall events. About this, the difference between

the 13°- and 30°-Panola hillslope was that while the spilling of water from the main bedrock depression at the 13°-Panola hillslope occurred during the drainage following the initial rainfall, at the 30°-Panola hillslope it occurred during the same rainfall event (i.e., during the second phase of rainfall when lateral flows become relevant). This was basically related to the different velocity of the 30°-Panola hillslope in dissipating the positive pore pressure than the 13°-Panola hillslope.

Interestingly, the failure zone was not localized in the main bedrock depression on the midslope, where the maximum increase of pore pressure values were observed. Rather, it was located in the zone immediately upslope the main depression, where the localized bedrock surface was very steep and pore pressure increased enough to generate instability. Here, pore pressure increased because of the presence of the bedrock ridge just downslope the main bedrock depression that induced upslope flow accumulation. This specific result recalls findings of Speight (1980) who argued that it is the balance between the specific catchment area (i.e., upslope area) and the dispersal area (i.e., downslope area) that controls the "storage propensity" of a given location. Downslope topographic micro-relief can significantly modify the upslope flow dynamics, altering the drainage directions and determining the landslide position.

4.5.3 Issues in modeling slope stability

The simulation effort reported in this study focused on a relatively small spatial scale (the ~0.1 ha Panola hillslope) and a relatively short temporal scale. To show the potential effect of subsurface topography in determining timing and position of shallow landslide initiation, it has been used a methodology which is similar to that of Dutton et al. (2005) and Mirus et al. (2007), with a "sophisticated" 3-dimensional hydrological analysis and separate FS estimates. Admittedly, this approach does not address the fully coupled processes of hydrologic response and slope deformation that would be desirable to describe the complex mechanism of collapse induced by our irregular bedrock topography. A coupled model has been developed by Borja and Witte (2010). They developed a physics-based continuum model that captures the coupled solid deformation–fluid flow processes in variably saturated slopes. Their model accommodates relevant constitutive properties of the soil, in order to realistically quantify stresses and pore pressures responsible for triggering slope failure. In future studies, this will be the best approach to assess the role of bedrock depressions on soil displacements and subsequent slope failure. What makes this next step challenging is that this type of model requires a long list of further details on soil properties (in addition to those required by our uncoupled model), including: elastic bulk modulus, Poisson's ratio (needed to introduce stresses in the model), dilatancy angle (that affects the volume change of the soil during yielding) and possibly other parameters depending on the constitutive law used to

model the soil material. Furthermore, characterization of the initial in situ stress conditions within the slope would be needed for implementation of such an approach.

Here, although not as rigorous as the hydrologic-response (Hydrus 3-D) model, the simplified slope stability model provided a first-order understanding of the importance of irregular bedrock topography in the context of hillslope stability. The infinite slope stability model allowed to establish the triggered zones (or local instability), while the CA model allowed to describe the mechanical interactions among pixels. The rationale behind this is that landslide initiation requires that the equilibrium threshold is exceeded in a certain number of locations close to the triggered (and often isolated) points, in order to form a pattern of weakness for the soil mantled slope. The triggered points increase the shear stress in adjacent points in the hillslope causing failure of a connected domain with shear stress larger than the threshold value (Pelletier et al., 1997). It should be noted that a definitive value of the factor of safety for the connected domain (i.e., failure area) is not provided. Indeed, the efforts of this work aimed to understand the impact of the irregular subsurface topography in determining the spatial spreading and temporal development of this connected failure area (i.e., the threshold-like expansion behavior that emerged during the second phase of the rainfall).

A modified CA model with a different rule to propagate soil-stresses of destabilized cells was also tested; in this modified version, the destabilizing force F_d^i of the unstable cell i with elevation z_i is only redistributed among the neighbors i_{nn} with elevation $z_{i_{nn}}$ lower than z_i . Accordingly, the safety factors of the 8 neighbors i_{nn} are given by:

$$FS_{i_{nn}} = \frac{F_r^{i_{nn}}}{F_d^{i_{nn}} + F_d^i \frac{\max(0, z_i - z_{i_{nn}})}{\sum_{i_{nn}} \max(0, z_i - z_{i_{nn}})}} \quad (4.8)$$

Results by this modified CA model confirmed that instability spread over large area once the about 35 mm-threshold on cumulative rainfall was exceeded.

Finally, it should be noted that this work has not focused on the effect of other sources of heterogeneity on stability responses of the subject slope. Spatial heterogeneity related to soil cohesion, soil friction angle, soil permeability, and root cohesion do impact the location of shallow landslide events. These properties may vary largely (even on small scales) and adoption of a deterministic (i.e., single) value of these properties may result in unrealistic representation of the instability locations. Here, research efforts focus solely on the role played by soil depth and bedrock topography on near-surface hydrologic response and slope stability. This effect of heterogeneity has so far received very little attention in the context of hillslope stability, while there are now tangible evidence (based on both field experiments and numerical analysis) that subsurface topography has a strong impact in controlling

connectivity and dynamics of saturated patches at the soil-bedrock interface and therefore effective stress and soil mechanical behavior.

4.5.4 Implications for catchment-scale shallow landslide models

Many recent catchment-scale landslide modeling efforts have focused on new and more effective ways to describe flows from upslope by using the topographic index or dynamic topographic index approaches (i.e., Montgomery and Dietrich, 1994; Wu and Sidle, 1995, Borga et al. 2002, Tarolli and Tarboton, 2006). Our work suggests that new focus on soil depth mapping (to then back-calculate the topography of the bedrock surface) may be useful to improve our ability to predict timing and location of shallow landslide initiation.

It is worth pointing out that the scale of interest in this study is much smaller than for the catchment-scale studies of hydrologically driven shallow landslide model that are reported in the literature (e.g., Montgomery et al., 1998, 2000; Pack et al., 1998; Casadei et al., 2003, Borga et al., 2002; Reid et al., 2007; Tarolli et al., 2008; Capparelli and Versace, 2010; Arnone et al., 2011). At the catchment scale, it is most often necessary to make simplifying assumptions related to hydrologic response (Loague et al., 2006). However, the results of this work showed that subsurface topography has a strong impact in controlling the connectivity of saturated patches at the soil-bedrock interface but despite this evidence, most catchment-scale shallow landslide models fail to include a connectivity component. Therefore, results of this work invoke at least a simplified treatment of the problem. This has been done for overland flow processes (Lane et al., 2004) and fine sediment and soil erosion processes (Reid et al., 2007, and Lane et al., 2009) by extending the traditional topographic index approach to include a simplified representation of surface hydrological connectivity. A similar approach can be adopted for subsurface flow processes and shallow landslide processes.

4.6 Conclusions

This Chapter has sought to link an important new finding from the hillslope hydrological literature—the filling and spilling of transient saturation at the soil-bedrock interface—with landslide related processes at the hillslope scale. The results of this work highlighted that bedrock-depressions play a key role on pore pressure dynamics and shallow failure initiation. Topographic depressions at the bedrock layer induce localized zones of increased pressure head such that the development of pore-pressure fields—not predictable by ground surface topography—leads to rapid landslide propagation. Isolated transient groundwater pockets at the soil-bedrock interface produced during rainfall events spill over small bedrock ridges to form sudden and connected saturated areas that instantaneously reduce the factor of safety through the hillslope. This emergent behavior occurs after that a precipitation threshold has

been exceeded and may be key responsible for the rapid transition from stable to unstable conditions generally observed for shallow (and for this unpredictable) landslide phenomena. Modelling pore pressure spatial distribution using the topography of the bedrock may significantly improve the ability of landslide models to detect shape and location of the slip surface. While such data are largely unavailable, except for well studied hillslopes and watersheds, promising new work (Pelletier and Rasmussen, 2009) suggests that soil depth modeling may be a way to then derive bedrock topographic relief and lead to the coupling of physically-based landslide models with quantitative soil–landscape methods to ultimately improve the ability to predict shallow landslide potential. Other works (e.g., Lane et al., 2004; Reid et al., 2009) have suggested that a connectivity component for (lateral) subsurface flow may be easily implemented in catchment-scale shallow landslide models. An attempt to do this is presented in the next Chapter of this Thesis.

Chapter 5

Modelling catchment-scale shallow landslide occurrence by means of a subsurface flow path connectivity index

5.1 Introduction

Chapter 4 has recognized that at least a simplified treatment of subsurface hydrological connectivity is needed to improve the ability to predict timing and location of shallow landslide initiation. The subsurface flow paths that link source areas to a generic point in the hillslope control the development of pore-water pressures at that point and the local value of the factor of safety. Even if two locations have the same mechanical (i.e., cohesion and frictional angle) and geomorphological (i.e., upslope source area, local slope, aspect, curvature, etc.) attributes there may be a substantial difference between them in terms of shallow landslide propensity, depending on whether the point hydrologically connects with its own upslope source area.

Arising from these considerations, in this Chapter a new topographic index-based shallow landslide model that includes the concept of hydrological connectivity in the description of the subsurface flow processes is presented. The model keeps the simplicity of the topographic index approach needed to conduct large scale analysis. In the model, hydrological connectivity is preliminary related to the spatial variability of soil depth across the investigated catchments, and the initial soil moisture conditions. Vertical rain-water infiltration into unsaturated soil is simulated by using the concept of drainable porosity (i.e. the volume of stored soil-water removed/added per unit area per unit decline/growth of water table level – Hilberts et al., 2005). This allows simulating pore-water pressure dynamics under the assumption of quasi-steady state hydraulic equilibrium and to estimate the time for development of a perched water-table at the soil/bedrock interface. The model incorporates the computation of a connectivity time, which is the time required for a generic hillslope element to achieve complete saturation along the flow path most likely to link it with its own upslope source area. The dynamic topographic index developed in Chapter 3 is used to describe the transient lateral subsurface flow for times greater than the connectivity time. The hydrological model is then coupled with the infinite slope stability model to derive a

shallow landslide model which is able to account for the effect of the unsaturated zone storage on slope stability. A critical rainfall intensity is computed by the model for a set of rainfall durations, which represent the hydrological conditions leading to hillslope instability. A scaling model for extreme rainfall is used to estimate the return period of the critical rainfall for shallow landsliding.

Model testing is carried out in three study sites located in the central Italian Alps. In this area, shallow landslides are generally triggered by local, convective storms during the summer and initial fall seasons. For these areas, accurate field surveys provide a description of hydraulic and geotechnical properties of soils and a detailed representation of soil depth variation as a function of local slope is reported. An inventory of shallow landslides is also available. Finally, the proposed shallow landslide model is used to derive local rainfall intensity-duration thresholds for the initiation of shallow landslides.

This work has been submitted as: Lanni C, Borga M, Rigon R, Tarolli P. 2012. Modelling catchment-scale shallow landslide occurrence by means of a subsurface flow path connectivity index. In *Hydrology and Earth System Science*.

5.2 Materials and methods

5.2.1 The hydrological model

Figure 5.1 schematizes the hydrological model developed in this chapter. The model provides the pore pressure values at the soil-bedrock interface in each point of a hillslope. In the model, during a rainfall event the formation of lateral flow is preceded by the development of positive pressure head (i.e. perched water table) at the soil-bedrock interface. Several researchers (McNamara et al., 2005; Rahardjo et al., 2005) have shown that infiltration through an unsaturated zone is vertical and (generally) causes no positive pore pressures. This vertical flow is reduced if the infiltration front meets a less permeable layer (for example, the bedrock layer) and the infiltration rate is larger than the permeability of this low-conductive layer. Under this condition, the infiltrating rainwater collects at the less permeable soil layer inducing rapid increases of pore-water pressure and unsaturated hydraulic conductivity (according to the relationship between matric suction head and unsaturated hydraulic conductivity). As a result, a perched water table will form on the surface of the low-conductive layer, and a subsurface flow will move laterally along the upper surface of this layer (e.g. Weyman, 1973; Weiler et al., 2005).

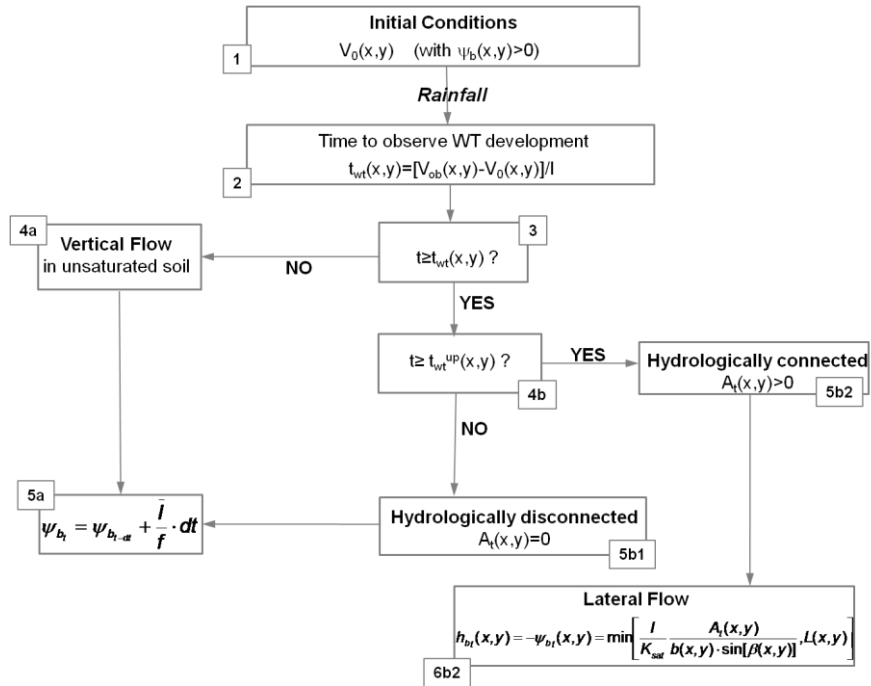


Figure 5.1. A flow chart depicting the coupled saturated/unsaturated hydrological model developed in this Chapter

Moreover, in the model we assume that a generic hillslope element (x,y) receives flow from the related upslope catchment area A(x,y) when isolated patches of transient saturation become connected with element (x,y) (Fig. 5.2). This assumption follows recent field observations (e.g., Tromp-van Meerveld and McDonnell, 2006b; McGuire and McDonnell, 2010) and physically based modelling studies (e.g., Hopp and McDonnell, 2009; Lanni et al., 2011) where it has been shown that a generic hillslope element receives (rapid) drainage from the upslope contributing area when patches of saturation at the soil-bedrock interface become spatially connected with it.

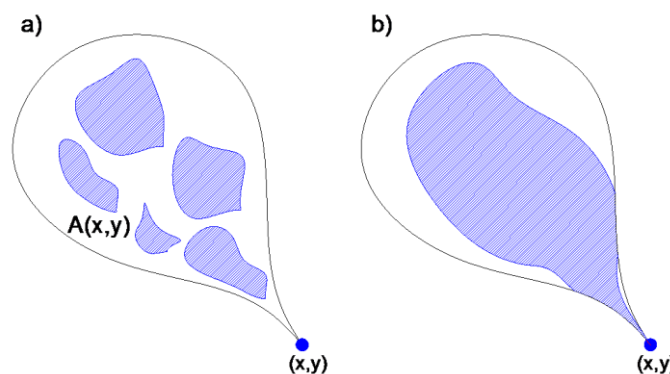


Figure 5.2. The concept of hydrological connectivity. Lateral subsurface flow occurs at point (x,y) when this becomes hydrologically connected with its own upslope contributing area A(x,y) (b)

According to field observations, unsaturated soil conditions through the whole soil-profile (i.e. positive suction head or negative pressure head) are used to initialize the model (step 1 in Fig. 5.1). For each hillslope element (x,y), the time $t_{wt}(x,y)$ needed to build up a perched zone of positive pore pressure at the soil-bedrock interface is computed by using the following expression (2 in Fig. 5.1):

$$t_{wt}(x,y) = \frac{V_{wt}(x,y) - V_o(x,y)}{I} \quad (5.1)$$

where V_o [L] is the initial storage of soil moisture through the soil profile before of a rainfall event (Fig. 5.3); V_{wt} [L] is the storage of soil moisture needed to produce a perched water table (i.e., zero-pressure head) at the soil-bedrock interface (Fig. 5.3); and I [LT^{-1}] is the rainfall intensity. Computation of V_o and V_{wt} require the use of a relationship between soil moisture content θ [-] and suction head ψ [L], and a relationship between ψ and the vertical coordinate (positive upward) z [L] (Fig. 5.3).

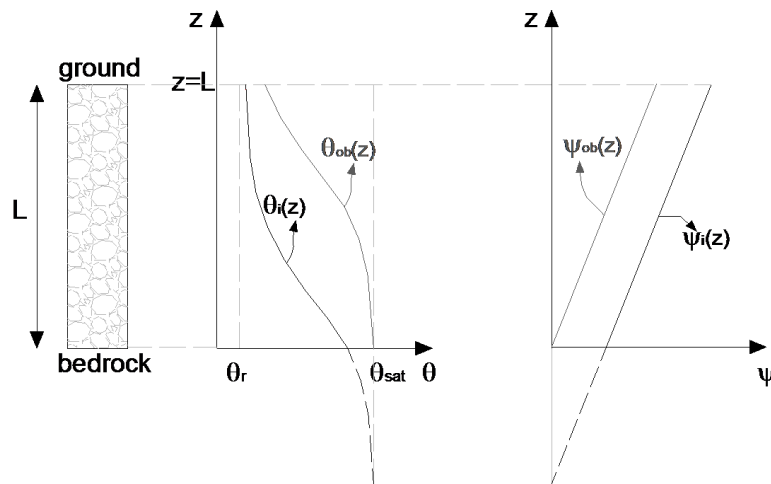


Figure 5.3. $\theta_i(z)$ and $\psi_i(z)$ are, respectively, the initial water content and the initial suction head vertical profiles. $\theta_{wt}(z)$ and $\psi_{wt}(z)$ represents the linear water content and suction head vertical profiles associated with zero-suction head at the soil-bedrock interface

By using the assumption that the suction head profile $\psi(z)$ changes from one steady-state situation to another over the time, the relation between ψ [L] and z [L] is that of hydraulic equilibrium:

$$\psi = \psi(z=0) + z = \psi_b + z \quad (5.2)$$

where $\psi_b = \psi(z=0)$ is the suction head at the soil-bedrock interface. Bierkens (1998) argued that this assumption is valid for shallow system where redistribution of soil-water is rapid.

Furthermore, comparisons with numerical models results described in Appendix 5.A (at the end of this Chapter) demonstrate that t_{wt} (the time needed to build up a perched zone of positive pore pressure at the soil-bedrock interface) computed by using this simplified approach is similar to results from a one-dimensional Richards' equation solver (Figure 5.A1).

The constitutive relationship between θ and ψ used in this study is the van Genuchten function (van Genuchten, 1980):

$$\theta(\psi) = \theta_r + (\theta_{sat} - \theta_r)[1 + (\alpha\psi)^n]^{-m} \quad (5.3)$$

with θ_{sat} [-] = saturated water content; θ_r [-] = residual water content; α [L^{-1}] = parameter that depends approximately on the air-entry (or air-occlusion) suction; n [-] and m [-] = van Genuchten parameters. Combining Equations (5.2) and (5.3) leads to:

$$\theta(\psi) = \theta_r + (\theta_{sat} - \theta_r)[1 + (\alpha(\psi_b + z))^n]^{-m} \quad (5.4)$$

Troch et al. (1992) found that for the $\theta(\psi)$ relationship it is possible to assume the following relationship between m and n :

$$m = 1 + \frac{1}{n} \quad (5.5)$$

instead of the common $m=1-1/n$, without losing the ability to aptly fit the soil moisture retention data for a wide range of soil types. The storage of soil moisture through the soil profile V is obtained by integrating Equation (5.4) from the bedrock to the ground surface:

$$V = \int_{z=0}^{z=L} \theta(z) dz = \theta_r \cdot L + (\theta_{sat} - \theta_r) \left[(L + \psi_b)(1 + (\alpha(L + \psi_b))^n)^{-\frac{1}{n}} - \psi_b(1 + (\alpha\psi_b)^n)^{-\frac{1}{n}} \right] \quad (5.6)$$

while V_{wt} can be obtained by setting zero-pressure head at the soil-bedrock interface ($\psi_b=0$):

$$V_{wt} = \theta_r \cdot L + (\theta_{sat} - \theta_r) \cdot L \cdot (1 + (\alpha L)^n)^{-\frac{1}{n}} \quad (5.7)$$

The suction head value at the soil-bedrock interface at a generic time $t < t_{wt}(x,y)$ (i.e., before development of a perched water table), ψ_{bt} , can be calculated by using the concept of drainable porosity f [-] proposed by Hilberts et al. (2005):

$$f = \frac{dV}{d\psi_b} = (\theta_{sat} - \theta_r) \cdot \left[(1 + (\alpha(L + \psi_b))^n)^{-1-\frac{1}{n}} - (1 + (\alpha\psi_b)^n)^{-1-\frac{1}{n}} \right] \quad (5.8)$$

An expression for $d\psi_b/dt$, useful to estimate the suction head at the soil-bedrock interface at a

generic time t , ψ_{bt} (5a in Fig. 5.1) can be calculated by using Equation (5.8):

$$\frac{d\psi_b}{dt} = \frac{I}{f} \Rightarrow \psi_{bt} = \psi_{bt-1} + \frac{I}{(\theta_{sat} - \theta_r) \cdot \left[(1 + (\alpha(L + \psi_b))^n)^{-1-\frac{1}{n}} - (1 + (\alpha\psi_b)^n)^{-1-\frac{1}{n}} \right]} \quad (5.9)$$

For $t \geq t_{wt}(x,y)$, the generic hillslope element (x,y) exhibits a perched water table at the soil-bedrock interface. However, this does not guarantee the hydrological connectivity between element (x,y) and its related upslope contributing area $A(x,y)$. In fact, due to the heterogeneity of initial soil-moisture and soil depth, isolated patches of saturation which do not necessarily connect with point (x,y) may have developed inside $A(x,y)$.

In the model, it is assumed that lateral subsurface flow affects the local soil-water storage of point (x,y) when the water table time t_{wt} indicates continuous saturation through $A(x,y)$. Thus, each point (x,y) has two water table characteristic times: (1) t_{wt} , which indicates the local time for the development of a perched water table; and (2) a connectivity time t_{wt}^{up} – given by the maximum value of t_{wt} in $A(x,y)$ – which indicates the time required by element (x,y) to become hydrological connected with $A(x,y)$. Therefore, a generic hillslope element (x,y) receives flow from its own upslope contributing area starting from $t = t_{wt}^{up}(x,y)$ (3 and 4b in Fig. 5.1). Details on the formulation of the connectivity time t_{wt}^{up} are given in Appendix 5.B at the end of this Chapter.

The incoming lateral flow in element (x,y) is then calculated by using the upslope contributing area $A(x,y)$ as a surrogate for lateral flow. Specifically, the method proposed in Chapter 3 was adapted to take into account the connectivity time for lateral subsurface flow commencement:

$$A_t(x,y) = \frac{t - t_{wt}^{up}(x,y)}{\tau_c(x,y)} A(x,y) \quad \text{for} \quad t_{wt}^{up}(x,y) < t \leq \tau_c(x,y) \quad (5.10a)$$

$$A_t(x,y) = A(x,y) \quad \text{for} \quad \tau_c(x,y) \leq t \leq d \quad (5.10b)$$

$$A_t(x,y) = \max \left[0, A(x,y) \left(1 + \frac{d-t}{\tau_c(x,y) - t_{wt}^{up}(x,y)} \right) \right] \quad \text{for} \quad t \geq d \quad \text{if} \quad \tau_c(x,y) \leq d \quad (5.10c)$$

$$A_t(x,y) = \max \left[0, A(x,y) \left(1 + \frac{2d - t_{wt}(x,y) - t}{\tau_c(x,y) - t_{wt}^{up}(x,y)} \right) \right] \quad \text{for} \quad t_{wt}^{up}(x,y) < t < d \quad \text{if} \quad \tau_c(x,y) \leq d \quad (5.10d)$$

where A_t and A are, respectively, the time-variable upslope contributing area and the (steady-state) upslope contributing area; t [T] = time; d [T] = rainfall duration; τ_c [T] = time of concentration (i.e., the time required for a drop of water to travel from the most hydrologically remote location in the subcatchment $A(x,y)$ to the (x,y) point under investigation). τ_c is defined as the maximum ratio between the flow-path length and the celerity of water given by Darcy's law added to the connectivity time for lateral subsurface flow commencement $t_{wt}^{up}(x,y)$:

$$\tau_c(x,y) = \left\{ \frac{l_{Hj}(x,y)}{\cos(\beta_{1Hj}(x,y))} \frac{\Phi_{1Hj}(x,y)}{K_{sat1Hj}(x,y) \cdot \sin(\beta_{1Hj}(x,y))} \right\} + t_{wt}^{up}(x,y)$$

with $j=1, \dots$, number of flow paths converging in point (x,y) (5.11)

where $\beta_{1Hj}(x,y)$ [°] is the average inclination angle of the j -th flow path, of horizontal length l_{Hj} [L], which converges in the (x,y) catchment-point, while $\Phi_{1Hj}(x,y)$ [-] and $K_{sat1Hj}(x,y)$ [LT⁻¹] are the average soil-porosity and saturated hydraulic conductivity along the j -th flow path, respectively.

Therefore, under the assumptions of constant rainfall intensity I in time and space, the positive pore pressure value at the soil-bedrock interface of point (x,y) for a generic time $t \geq t_{wt}^{up}(x,y)$, $h_{bt}(x,y)$ is given by (6b2 in Fig. 5.1):

$$h_{bt}(x,y) = -\psi_{bt}(x,y) = \min \left[\frac{I}{K_{sat}(x,y)} \cdot \frac{A_t(x,y)}{b(x,y) \cdot \sin[\beta(x,y)]}, L(x,y) \right] \quad (5.12)$$

where β [°] is the local slope angle, and A_t/b [L] is the time-variable contributing area per unit contour length.

5.2.2 The coupled hydrological-slope stability model

For hillslopes it is common to define the safety factor as the ratio between maximum retaining forces, F_r , and driving forces, F_d :

$$FS = \frac{F_d}{F_r} \quad (5.13)$$

The slope is stable for $FS > 1$, while slope failure occurs when the critical state $FS = 1$ (such that $F_r = F_d$) is achieved. Lu & Likos (2006) derived a formulation to compute the factor of safety of an infinite slope model that accounts for saturated/unsaturated zones. If the failure surface is located at the soil-bedrock interface, then the Lu & Likos' factor of safety can be written as:

$$FS = \frac{2 \cdot c'}{\gamma \cdot L \cdot \sin[2\beta]} + \frac{\tan \phi'}{\tan \beta} + S_e(\psi_b) \frac{\gamma_w}{\gamma} \frac{\Psi_b}{L} (\tan \beta + \cot \beta) \cdot \tan \phi'$$

for $\psi_b > 0 (h_b < 0)$ (5.14a)

$$FS = \frac{2 \cdot c'}{\gamma \cdot L \cdot \sin[2\beta]} + \frac{\tan \phi'}{\tan \beta} + \frac{\gamma_w}{\gamma} \frac{\Psi_b}{L} (\tan \beta + \cot \beta) \cdot \tan \phi'$$

for $\psi_b > 0 (h_b < 0)$ (5.14b)

with c' [FL^{-2}]= effective soil cohesion; ϕ' [$^\circ$]= effective soil frictional angle; γ_w and γ [FL^{-3}]= volumetric unit weight of water and soil, respectively; S_e [-]= relative saturation degree. Equation (5.14) allows to take into account for the (positive) role played by suction head on the hillslopes stability. In this work, locations that are neither unconditionally unstable (i.e., locations that are unstable under the minimum soil-moisture conditions) or unconditionally stable (i.e., locations that are stable when saturated) will be called conditionally unstable as proposed in the pioneer work of Montgomery and Dietrich (1994).

By coupling the hydrological model (Eq. 5.9 and 5.12) with the slope stability model (Eq. 14) the factor of safety for conditionally unstable locations (x,y) at a generic time t reads:

$$FS_t(x, y) = \frac{2 \cdot c'(x, y)}{\gamma \cdot L \cdot \sin[2\beta(x, y)]} + \frac{\tan \phi'(x, y)}{\tan \beta(x, y)} + S_e(\psi_{bt}(x, y)) \frac{\gamma_w(x, y)}{\gamma(x, y)} \frac{\Psi_{bt}(x, y)}{L(x, y)} (\tan \beta(x, y) + \cot \beta(x, y)) \cdot \tan \phi'(x, y)$$

for $\psi_{bt}(x, y) > 0$ ($h_{bt}(x, y) < 0$) (5.15a)

$$FS_t(x, y) = \frac{2 \cdot c'(x, y)}{\gamma \cdot L \cdot \sin[2\beta(x, y)]} + \frac{\tan \phi'(x, y)}{\tan \beta(x, y)} + \frac{\gamma_w(x, y)}{\gamma(x, y)} \frac{I}{K_{sat}(x, y) \cdot L(x, y)} \frac{A_t(x, y)}{b(x, y) \cdot \sin \beta(x, y)} (\tan \beta(x, y) + \cot \beta(x, y)) \cdot \tan \phi'(x, y)$$

for $\psi_{bt}(x, y) \leq 0$ ($h_{bt}(x, y) \geq 0$) (5.15b)

5.2.3 Intensity-Duration-Frequency relationship for extreme rainfall events

The variability of rainfall intensity with rainfall duration for a specified frequency level is often represented by the Intensity-Duration-Frequency (IDF) relationship proposed by Koutsoyiannis et al. (1998):

$$I_F(d) = \zeta_F \cdot d^{m_F-1} \quad (5.16)$$

with $I_F(d)$ = rainfall intensity that can be exceeded with a probability of $(1-F)$. ζ_F and m_F are parameters estimated by least squares regression of $I_F(d)$ against rainfall duration d . It has been showed (Burlando & Rosso, 1996) that a Gumbel simple scaling model describes well the distribution of annual maximum series of rainfall in the Central Italian Alps. Based on this model, the rainfall intensity $I_F(d)$ can be determined as:

$$I_F(d) = \zeta_1 \left[1 - \frac{CV\sqrt{6}}{\pi} (\varepsilon + y_{TR}) \right] \cdot d^{m-1} \quad (5.17)$$

with ε = Euler's constant (~ 0.5772). ζ_1 and m can be estimated by linear regression of expectations of rainfall depth against duration, after log transformation, whereas the value of the coefficient of variation CV can be obtained as the average of coefficients of variation computed for the different durations, in the range of durations for which the scaling property holds. y_{TR} is given by:

$$y_{TR} = \ln \left(\ln \left(\frac{T_R}{T_R - 1} \right) \right) \quad (5.18)$$

where T_R [T] is the return period. By combining Equations (5.17) and (5.18), T_R can be written as a function of rainfall intensity and duration:

$$T_R = \frac{\exp \left[\exp \left[\frac{\pi}{CV\sqrt{6}} \left(1 - \zeta_1 \frac{I_F(d)}{d^{m-1}} \right) - \varepsilon \right] \right]}{\exp \left[\exp \left[\frac{\pi}{CV\sqrt{6}} \left(1 - \zeta_1 \frac{I_F(d)}{d^{m-1}} \right) - \varepsilon \right] \right] - 1} \quad (5.19)$$

5.2.4 Study sites and model application

The study area is represented by three small catchments located in the central Italian Alps: Cortina, Fraviano, and Pizzano catchments (Fig. 5.4). The overall surface of the three catchments is 7.5 km². Elevations (E) range from 1250 to 2830 m a.s.l., with an average value of 1999 m a.s.l. Average slope is 28°, almost identical between the three catchments. 10 m-resolution digital terrain models (DTMs) for the three catchments were derived from a 1:10,000 scale contour map. The shallow landslides analyzed in this work were mapped in the period between 2000 and 2003, and were triggered by several rainfall events, in particular by relatively short duration events occurred during the falls of 2000 and 2002. Vegetation covers 82.4% of the Cortina catchment, consisting of forest stands (74.2%) and grassland (8.2%), while the remaining part is unvegetated soils. The Fraviano catchment presents a higher portion of grassland (24.3%) than the Cortina catchment. The forest stands cover

55.3%, while remaining areas are unvegetated soil. Land use of the Pizzano catchment is similar to that observed for the Fraviano catchment.

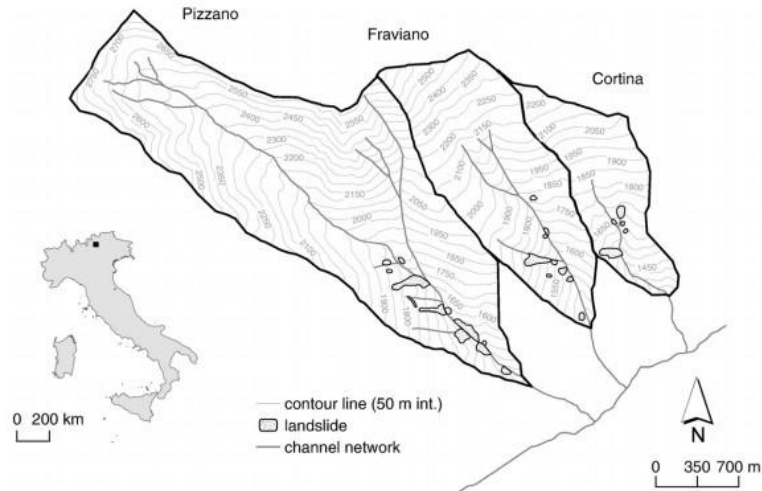


Figure 5.4. Catchments case study. The map shows the location of the three catchments, and the landslide distribution (polygons inside the catchments)

Soil depth, topographic curvature and local slope were surveyed at a total of 49 points within the three subwatersheds. Survey locations were chosen to represent the range of topographic variation in the areas of model application. At each location two or three soil depth replicates 2–3 m apart were collected by driving a 150 cm long 1.27 cm diameter sharpened copper coated steel rod graduated at 5 cm interval vertically into the ground using a fence post pounder until refusal. The advantage of the depth to refusal method is that it is a direct and simple measurement of soil depth. It is inexpensive, albeit laborious and time consuming and limited to depths to which a rod can be pounded. A disadvantage is that the measurement is biased to underestimating actual depth to bedrock, since there is uncertainty as to what actually causes refusal. Rocks and gravel that occur as residual relicts from weathering or colluvium may limit the rod penetration resulting in underestimation of soil depth.

The following relationship between soil depth L and local slope angle $\tan\beta$ was derived from the field measurements:

$$L = 1.006 - 0.85 \cdot \tan\beta \quad \text{for } 0^\circ \leq \beta \leq 45^\circ \quad (5.20a)$$

$$L = 0 \quad \text{for } \beta \geq 45^\circ \quad (5.20b)$$

for $E < 2000$ m a.s.l.

$$L = 1.006 - 0.85 \cdot \tan\beta \quad \text{for } 0^\circ \leq \beta \leq 40^\circ \quad (5.20c)$$

$$L = 0 \quad \text{for } \beta \geq 40^\circ \quad (5.20d)$$

for $E \geq 2000$ m a.s.l.

In fact, locations with local slope angle larger than 45° (below 2000 m) and 40° (above 2000 m) are characterized by rocky outcrops or very shallow soil thickness. Other topographic variables, such as plan curvature and specific catchment area, and land cover attributes showed no statistically significant relationship with soil depth. The relationship between soil depth and slope identified for the study catchments are consistent with findings reported in the literature (Saulnier et al., 1997; Tesfa et al., 2009).

The landslide area amounts to 1.4% of the total area for the Cortina and Fraviano catchments and to 1.2% of the total area for the Pizzano catchment. An intensive field campaign was carried out in the area during the summer season 2003, leading to the estimation of the hydraulic and mechanical soil-parameters reported in Table 5.1. The soil properties are assumed to be the same for all the three catchments. Although the forest stands cover more than 50% of the areas, the soils in the basins can be considered cohesionless or only slightly cohesive.

Table 5.1. Hydraulic and mechanical soil-parameters relative to the three investigated catchments

<i>Soil-parameter</i>	<i>Unit</i>	<i>Value</i>
Density ratio (γ_s / γ_w)	[-]	1.8
Saturated water content θ_{sat}	[-]	0.3
Residual water content θ_r	[-]	0.05
α – van Genuchten	m ⁻¹	3.44
n – van Genuchten	[-]	4.42
Saturated hydraulic conductivity K_{sat}	ms ⁻¹	10 ⁻³
Effective frictional angle ϕ	°	38
Effective cohesion c'	kPa	0

The soil-moisture initial conditions were assumed to represent average climatic conditions based on estimated evapotranspiration fluxes and interstorm duration statistics, which are typical of the seasons where shallow landslides were recorded (summer season and first half of the fall season). These unsaturated soil moisture conditions correspond to considerable cohesion which is due to capillarity, as conceptualized in the generalized principle of effective stress (Lu and Godt, 2008; Godt et al., 2009).

The procedure reported by Borga et al. (2005) was used to estimate the following scaling parameters of the IDF relationship (Eq. 18): $CV=0.42$, $m=0.48$, $\zeta_I=13.7 \text{ mmh}^{1-0.48}$.

Two general procedures may be considered for model application: diagnostic and predictive (Rosso et al., 2006). With the first procedure, terrain stability is simulated for a given temporal pattern of rainfall intensity and for given initial soil moisture conditions. This

allows exploration of the pattern of instability generated by specific storms and could be used to make real-time forecast of shallow landslides. The predictive procedure – able to provide a map of shallow landslide susceptibility- is adopted in this work. First, the critical duration d_c of rainfall which generates instability (i.e. $FS=1$) is computed for a range of constant rainfall intensity I (5, 10, 15, 20, 25, 30, 35, 40, 45, 50, 55, 60 mmh^{-1}). Then, the return period T_r is computed for each (I, d_c) pair analyzed by using Equation (5.20). Finally, the lowest return period for each conditionally stable location is selected. The map of the return period of the critical rainfall will provide a representation of the susceptibility to shallow landsliding across the landscape.

5.3 Results and discussion

The shallow landslide susceptibility map of Figure 5.5 was derived by adopting the predictive procedure discussed in the previous section. The criterion of shallow landslide susceptibility is based on the return period of the critical rainfall: higher return period values represent medium ($T_r=30-100$ years) and low ($T_r>100$ years) shallow landslide propensity, lower return period values represent high ($T_r=10-30$ years) and very high ($T_r<10$ years) shallow landslide propensity. A “very low” level of shallow landslide susceptibility is assigned to unconditionally stable points (i.e., locations that are stable when completely saturated, or locations characterized by bedrock outcrop). Examination of this map reveals that topographic elements in the steep areas close to the river are classified with a “very high” level of shallow landslide susceptibility ($T_r<10$ years). Conversely, higher values of critical return period T_r are found in gentle slope areas.

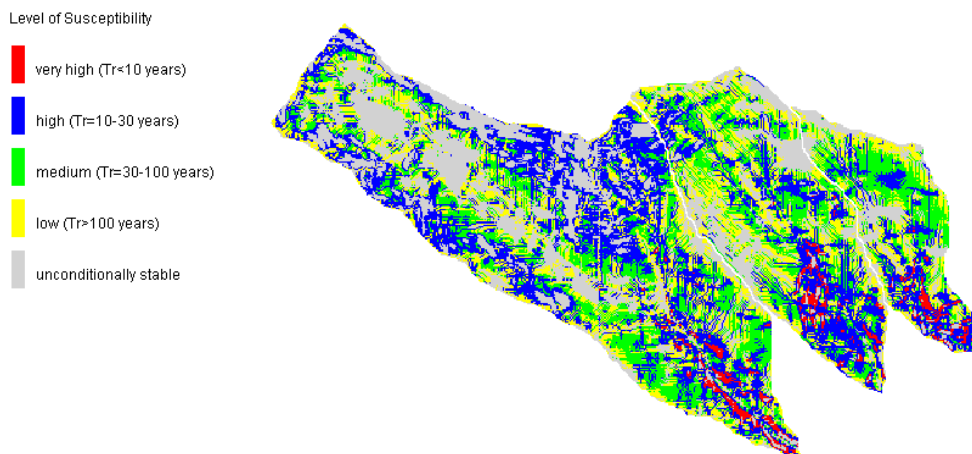


Figure 5.5. Patterns of Return period T_R (years) of the critical rainfalls for shallow landslide triggering (i.e., $FS \leq 1$) and associated levels of landslide susceptibility

5.3.1 Assessment of shallow landslide susceptibility

Analysis of the results indicates the good ability of the model to assess the shallow landslide propensity at the three investigated sites.

The assessment of the predictive power of the model is carried out by mapping the observed landslides onto the map of return period of critical rainfall necessary for slope instability and by comparing the resulting patterns. Table 5.2 shows the proportion of catchment area placed in the intervals of critical return period and the corresponding fraction of the landslide area. Better model performances are reflected by a larger difference between fractions of catchment, and observed landslide areas corresponding to low values of return period. For example, for the Pizzano basin the percentage of catchment area with a frequency of critical rainfall in the range of 0–10 years is equal to 1.6% (30.3% in the range of 10–30 years), while the corresponding fraction of observed landslide area is equal to 51.6% (41.4% in the range of 10–30 years). On the other hand, the percentage of landslide area with a frequency of critical rainfall >100 years is only the 1.1% versus the 49.3% (including the locations classified as unconditionally stable) of the catchment area. Therefore, the model would be able to correctly classify with a high or very high level of shallow landslide susceptibility most of the observed landslide areas. This is confirmed by the results for the Cortina and the Fraviano catchments, with this last one showing the best model predictions (63.8% of landslide area falling in the 2.5% of catchment area with $T_r \leq 10$ years).

Table 5.2. Percentages of slope-stability categories in terms of catchment area and observed landslide area in each range of critical rainfall frequency (i.e., return period TR) or level of shallow landslide susceptibility

T_R	Susceptibility Level	Pizzano		Fraviano		Cortina	
		C*	L**	C*	L**	C*	L**
Years	Category	%	%	%	%	%	%
0-10	Very High	1.6	51.6	2.5	63.8	3.8	24.3
10-30	High	30.3	41.4	26.9	36.2	24.2	75.7
30-100	Medium	18.0	5.9	22.1	0.0	26.3	0.0
>100	Low	18.0	1.1	24.3	0.0	21.9	0.0
Uncond. stable	Very Low	32.1	0.0	24.2	0.0	23.8	0.0

*C=catchment area; **L=landslide area

The model did not predict unconditionally unstable locations (i.e., locations predicted to be

unstable without rainfall). The contribute of negative pressure head (in Equation 5.15a) ensured the stability of steeper topographic elements (i.e., locations with $\tan\beta \geq \tan\phi'$ for cohesionless soils) that would be otherwise classified as unconditionally unstable from traditional landslide models (e.g. Montgomery & Dietrich, 1994; Wu & Sidle, 1995; Pack, 1995; Borga et al., 2002, Tarolli et al., 2011) that do not account for the role of negative pressure head on soil-shear strength.

This is an interesting aspect of this investigation, since it helps to overcome the limitations of previous studies carried out in the same catchments. For example, Tarolli et al. (2011) classified the 15% of the investigated area ($\sim 1.13 \text{ km}^2$) as unconditionally unstable, against the only 0.11 km^2 of inventoried landslide area. This overprediction was particularly pronounced in the upper hillslope zones (that are characterized by high local slope values), where the low upslope contributing areas (low recharge), the high local slope itself (high downslope drainage), and the till soil layer (high evapotranspiration rates) allow to maintain relatively dry (i.e., unsaturated) condition even during the year.

The results suggest that model predictions capture a high percentage of observed landslides, at the expenses of some overprediction of slope instability. However, overprediction of slope instability has been observed in other applications of topographic index-based shallow landsliding models (e.g. Dietrich et al., 2001). As explained in Tarolli et al., 2011, overprediction may be due to the following causes: i) inaccurate soil property data, ii) legacy effects of previous landslides, iii) limitation of the landslide surveys. Moreover, in steep terrain, a 10 m DTM-grid size such as that used here may lead to underestimation of the local slope steepness controlling shallow landsliding. It is also likely that the representation of the soil as cohesionless everywhere in this landscape may be responsible for overprediction of areas characterized by low return period.

5.3.2 Derivation of local rainfall thresholds for shallow landslide initiation

Once the capability of the model to assess the shallow landslide propensity at the investigated sites was verified, the model itself was used to derive local rainfall intensity-duration thresholds for shallow landslide initiation. Given the reduced computational cost of the model, it was possible to run a large number of numerical simulations in a very short time. We investigated 12 different constant value of rainfall intensity ($I = 5, 10, 15, 20, 25, 30, 35, 40, 45, 50, 55, 60 \text{ mmh}^{-1}$) in order to calculate, for each of these investigated cases, the critical rainfall duration d_c needed to cause slope instability (i.e., $FS=1$). Figure 5.6 shows the results obtained by plotting the rainfall intensity (ordinate axis) against the critical rainfall duration (abscissa axis) in a log-log graph (gray points). The lower envelope curve $I = 14.58 \cdot d_c^{-0.80}$ has been chosen as a I - d_c cautious threshold and may be used to forecast the occurrence of shallow landslides at the investigated sites based on continuous rainfall

measurements.

In Figure 5.6, the $I-d_c$ lower envelope is compared with the experimental $I-d$ threshold that triggered debris flow (filled circles in black) in some alpine catchments of the Dolomities. These catchments are geologically similar to our study area (the reader is referred to Gregoretto and Dalla Fontana, 2008 for further details on the empirical rainfall intensity–duration threshold). Modeled threshold is in good agreement with experimental threshold, proving that the $I-d_c$ cautious threshold may be used to forecast the occurrence of shallow landslides for the area of application.

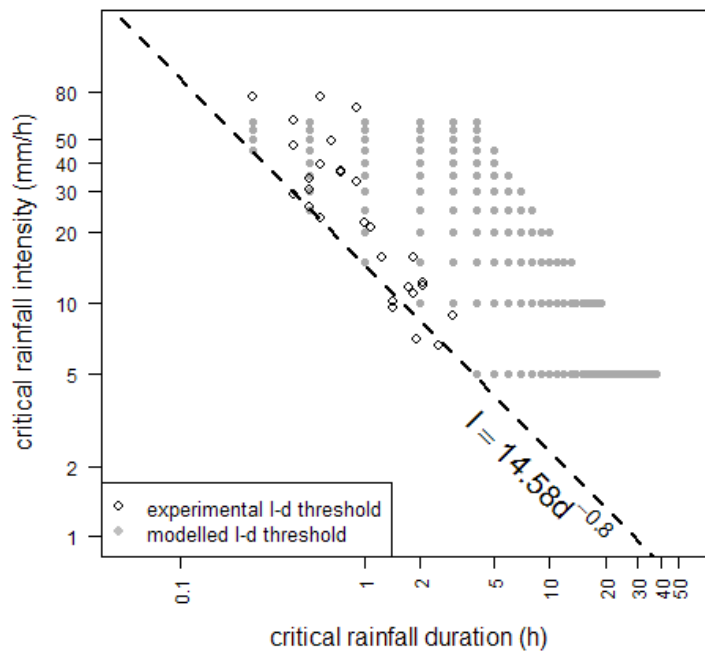


Figure 5.6. Modeled local rainfall intensity-duration ($I-d_c$) thresholds for shallow landslide initiation at the three investigated catchments, and experimental $I-d$ that triggered debris flow in some alpine catchments (of the Dolomities) similar to our study area

5.4 Summary and Conclusions

The shallow landslide model developed in this Chapter has proved to be appealing for investigating the relation between spatial occurrence of shallow landslides and characteristics of the triggering rainfall events. The model estimates the local pore pressure values by accounting for both vertical infiltration in the unsaturated soil and lateral flow in the saturated zone.

A procedure to assess shallow landslide susceptibility was presented by coupling the proposed shallow landslide model with Intensity-Duration-Frequency (IDF) relationships of extreme rainfall events. This procedure is based on the idea that lateral flow occurs when a

connectivity time for lateral subsurface flow initiation is achieved. This connectivity time represents the time-lag (from the onset of rainfall) required from a location in the basin to become hydrologically connected with its own upslope contributing area. For time less than the connectivity time, vertical infiltration is simulated by using the concept of drainable porosity under the assumption of quasi-steady state hydraulic equilibrium. For time greater than the threshold time, a dynamic topographic index allows to describe the transient lateral flow dynamics. Therefore, unlike the traditional, lateral flow-dominated, topographic index-based models, the proposed model is able to account for the effects of partially saturated soil suction stress on slope stability.

Model performance was evaluated over three catchments located in the central Italian Alps, where detailed inventories of shallow landslides are available. The model provides a reasonably correct surrogate for failure initiation probability in all case studies.

Once the capability of the model to assess the shallow landslide propensity at the investigated sites was verified, the model itself was used to define a local relationship on rainfall intensity-duration thresholds for shallow landslide initiation. These thresholds may be useful for forecasting landslide occurrence in the study sites. The proposed procedure may be adopted in the other catchments of the region affected by shallow landsliding phenomena to produce ad-hoc intensity-duration thresholds. This will help decision makers to efficiently allocate resources and personnel in emergency-response situations, and will allow (a) alerting the general public to the potential landslide activity, (b) limiting the alert signal to specific areas.

Appendix 5.A: Simplified unsaturated vertical infiltration model vs one-dimensional Richards' equation solver

To assess the error associated with the use of a simplified method to estimate the time t_{wt} (needed to build up a perched zone of positive pore pressure at the soil-bedrock interface), results from the unsaturated infiltration model proposed in Section 5.2.1 were compared with those from a one-dimensional Richards' equation solver (HYDRUS-1D, Simunek et al. 2008). 50 numerical simulations were performed on a colluvial soil layer overlying impermeable bedrock. We explored the interplay between three factors: soil depth (four values: 0.25 m, 0.5 m, 0.75 m, and 1.0 m), rainfall intensity (three values: 10 mmh⁻¹, 20 mmh⁻¹, and 30 mmh⁻¹), and initial condition (hydrostatic pore pressure profile with seven values of suction head at the soil-bedrock interface ψ_b : 0.05 m, 0.15 m, 0.25 m, 0.40 m, and 0.50 m). The systematic parameter exploration is useful in illustrating differences in t_{wt} estimation across the reasonable range of soil depth, initial condition and rainfall intensity values.

The same material properties of the soil reported in Table 5.1 were assumed for this

comparison. Relations between pressure head and hydraulic conductivity and soil-water content were described using the Mualem-van Genuchten model (van Genuchten, 1980). The domain was discretized using a uniform node spacing of 0.02 m in the vertical direction. Differences between t_{wt} computed with HYDRUS-1D and t_{wt} computed with the simplified infiltration model for the 50 investigated scenarios are shown in the three dimensional plot of Figure 5.A1. In general, differences are small and the highest differences are associated with high soil depth and initial suction head at the soil/bedrock interface, and low rainfall intensity.

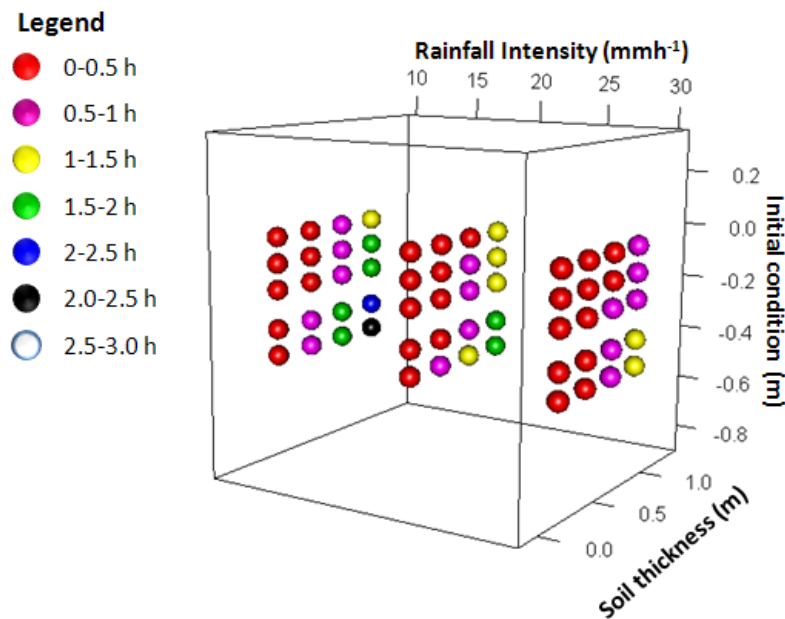


Figure 5.A1. The balls in the three dimensional space represent the differences between t_{wt} computed with HYDRUS-1D and t_{wt} computed with the simplified infiltration model (presented in Section 5.2.1) for 50 scenarios obtained by combining different values of soil thickness, rainfall intensity, and initial pore pressure profile

Appendix 5B: Computation of the connectivity time as a time of subsurface hydrological connectivity

The connectivity time t_{wt}^{up} for each point (x,y) in the basin is calculated as follows: starting at each point in the basin, each flow path is traced downslope, recording the highest value of the water table time t_{wt} encountered along this flow path. This highest value is assigned to each new cell encountered downslope until a higher value is encountered. This can be done because of the use of the D8 flow algorithm which assumes that each cell has a unique downslope flow direction. Therefore, when a flow path P2 converge in a pre-processed path P1, P2 is terminated if it contains a water table time lower than the encountered water table

time in P1. On the other hand, P2 continues downslope to modify P1 with the highest upslope water table time.

Thus each grid cell in the basin has both a t_{wt} value, which indicates the local time for the development of a perched water table, and a connectivity time t_{wt}^{up} , which defines when a cell is hydrologically connected with its own upslope contributing area.

Chapter 6

Conclusions and Future directions

6.1 Conclusions and future directions

This research tried to fill a gap between two very different scales of enquiry: the *local* (i.e. hillslope) scale, where detailed investigations are possible but difficult to generalize over large areas, and the *landscape* (i.e., catchment) scale, where representation of the physics is minimised, the resolution in space and time is maximised, and the focus is upon predicting emergent properties rather than system details. Specifically, this Thesis focused on an aspect of the geosciences that is of critical current concern: the representation of the interface between hydrological response and geomorphic processes, notable mass movements. At present there remains a great difficulty at this interface: detailed geotechnical and hydrological studies of mass movements reveal exceptionally complex interlinkages between water and the surface sediment mass, notably dynamically at the onset and during mass release; but these kinds of studies are only possible with a very detailed description of the three-dimensional structure of the porous media and its hydrological and mechanical response during (and after) rainfall events. Such analyses are feasible but tend to result in analyses that are restricted in terms of geographical generalisation. On the other hand, approaches that apply to larger spatial scales tend to over-simplify the representation of critical failure processes, such as in the assumptions that infinite slope stability analysis can be applied to failures that are finite in their slope length, or that upslope contributing area can always act as a surrogate for the hydrologic response at a point in the watershed.

Analyses at the hillslope scale (Chapter 4) showed that subsurface topography has a strong impact in controlling the connectivity of saturated areas at the soil-bedrock interface. Subsurface flow paths that link source areas to a generic point in the hillslope control the development of pore-water pressures at that point and the local value of the factor of safety, FS (i.e., the ratio of driving to resisting forces within the slope). These subsurface flow paths are spatially variable and temporally dynamic. Even if two locations have the same mechanical (i.e., cohesion and frictional angle) and geomorphological (i.e., upslope source area, local slope, aspect, curvature, etc.) attributes there may be a substantial difference between them in terms of shallow landslide propensity, depending on whether the point

hydrologically connects with its own upslope source area. Despite its noted importance, hydrological connectivity is poorly defined in landslide modelling. Although research has begun at the basin scale (Jensco et al., 2009) and certain aspects of hydrological connectivity have been incorporated into models (e.g., Lane et al., 2009), the literature review (Chapter 2) highlighted that the most used approaches for the assessment of shallow landslide initiation at the landscape scale have no real treatment of connectivity at all. Topographic index-based models remain strongly influenced by the variable source area concept of Hewlett and Hibbert (1967) and Dunne and Black (1970) by simplifying the process complexity into simple mathematical assumptions like the steady-state water table response, and topographically defined water flow paths. Physically-based numerical models should be intrinsically able to describe subsurface hydrological connectivity. However, numerical models commonly sacrifice spatial resolution (and hence spatial details) at the expense of increased scale. This is particularly problematic in relation to hydrological connectivity as it is variable over spatial scales of the order of a few meters.

Thus, there is a serious scale gap between the current ability to represent pore-water pressure dynamics into our catchment-scale shallow landslide models, and the actual nature of the mechanisms that drive the spatio-temporal evolution of subsurface flow paths.

This scale gap has motivated the development of a subsurface connectivity index (the connectivity time in Chapter 5) that allows for large-scale representation of hydrological connectivity, whilst maintaining the high spatial discretization needed to efficiently describe connectivity. Subsurface hydrological connectivity has been conceptualized starting from the hypothesis that connectivity of patches of transient saturation from a location to another on the hillslope depends upon the balance between processes that encourage lateral connection along a flow path and those that disconnect a flow path. Specifically, the spatial arrangement of the pore-water pressure (i.e., soil-water content) at the soil/bedrock interface was used as a connectivity metric, as locally dry (i.e., unsaturated) conditions reduce the propensity to lateral flow and prevent connectivity of isolated areas of saturation. Thus, this Thesis described the connectivity time for a point as the highest local time for the development of a perched water table along the flow path most likely to link the point with its own upslope contributing area.

The observation that soil depth heterogeneity and subsurface hydrological connectivity is important has provided an additional conceptual constraint (beyond the topographic effect taken into account through the topographic wetness index) that yielded significantly better predictions of those locations that are likely to slide at the investigated catchments. However, the reduction in complexity adopted in this work may not necessarily hold for other locations as a result of the implicit contextualisation of the model that limits its spatial relevance. Therefore, the model needs to be further generalized in order to include other factors controlling near-surface hydrological processes.

Specifically, there are at least three concerns regarding the approach used in this Thesis to represent subsurface hydrological connectivity. First, reflecting the nature of the study catchments, it has been assumed that the connectivity time was exclusively controlled by geomorphological attributes such as soil depth and subsurface drainage directions. Whilst this may be an acceptable assumption for small catchments with relatively homogenous soil type, it is unlikely to be suitable for larger watershed due to the effects of spatial heterogeneity in landscape properties and the inherent nonlinearity of many hydrological processes (e.g., Tetzlaff et al., 2007; McDonnell et al., 2007). Second, the proposed conceptualization of hydrological connectivity ignores the rapid throughflow through cracks, pipes, and macropores in the soil. Preferential flows may contribute to rapid pore pressures development (Uchida, 2004), and can have major impacts upon the ease of subsurface hydrological connection. Third, the model requires detailed description of soil thickness that is still one of the least understood and difficult to measure physical variables of the hillslope system at catchment scale (Catani et al., 2010). Soil thickness determines the degree of hydrological connectivity (and therefore shallow landslide patterns) in a catchment and is fundamental to estimate the actual landslide volume (e.g., Ho et al., 2011) in order to realistically map shallow landslide susceptibility and hazard.

Given these three issues, additional research is required to improve our understanding on the key factors (beyond soil depth heterogeneity) controlling subsurface hydrological connectivity and to include these additional factors in the formulation of the connectivity time. Moreover, it is worth pointing out that at the watershed scale connection can never be fully knowable because of uncertainties, particular those linked to data (e.g., initial soil moisture patterns). This is particularly the case for the connectivity time approach where the necessary information are inferred from localized data (i.e., the local time for the development of a perched water table) and are used directly, rather than being aggregate (as, for example, in the analysis of the topographic index using TOPMODEL, Beven and Kirkby, 1979). If localized data are used to determine the connectivity time, we need to understand how the assumption behind these analyses propagate into inference of subsurface hydrological connectivity.

Therefore, future research will focus on conceptualization and reformulation of the connectivity time to include:

1. Correction to the basic connectivity time approach to account for non-geomorphological influences (e.g., soil hydrological properties and bedrock leakage) upon the subsurface flow dynamics.
2. Further corrections to take into account situations where there is tangible evidence of preferential flow paths.
3. Analysis and propagation of the uncertainty in static descriptions of connectivity

Another aspect of this thesis was concerned with the method to assessing slope stability. At the catchment scale, the infinite slope model is commonly used to estimate the factor of safety for each cell of a digitalized landscape. It is implicitly assumed that the (downslope) length (L) and (across slope) width (B) of these cells represent the dimensions of the predicted landslide (Dietrich et al., 2007) and that these dimensions are large enough relative to the failure plane (Z) that the infinite slope assumption is valid (Ray et al., 2010). Milledge et al. (2012) argued that the infinite slope assumption can be valid if the ratio L/Z is greater than $\sim 18 \div 22$. For model with fine cell size, edge effects become relevant and violate the infinite slope model hypothesis at the cell scale. On the other hand, the coarser cell size may result in error because it smoothes out small steep areas that are indeed captured at the finer resolution. Moreover, as the pixel becomes coarse detection of small shallow landslides becomes more difficult. For example, at 20 m pixel resolution, a shallow landslide of 10 m or less is obliterated from a DEM.

Therefore, there is a need to improve our capability to describe shallow landslide triggering with high-resolution DEMs.

This Thesis has started to develop a model that is sufficiently mechanistic that it has meaningful parameters and can be tested to some degree, but not so deeply mechanistic that their application across large landscapes is impractical. The proposed model represents a first attempt to capture abruptness (i.e., the release of large soil masses at once with no apparent indicators for the imminence of mass release - Lehmann and Or, 2012) characterizing hazardous rainfall-induced shallow landslides. Specifically, a hillslope is described as a system of interconnected soil columns. When driving forces F_d exceed resisting forces F_r at a soil column base, failure occurs at that location and F_d affect, via a chain-interaction, the stability of the eight neighboring cells so that the failure may propagate and destabilize a larger hillslope area.

The cellular automata (CA) model presented in this Thesis represents a first step into describing system criticality in terms of standard physical hydro-mechanical variables. However, further development is needed to realistically quantify the failure propagation rate λ (i.e., the percentage of driving forces redistributed to the neighbors when driving forces exceed resisting forces within a soil column) and the actual mass release after landslide initiation.

6.2 Final considerations

Large-scale assessment of landslide and debris flow hazard is increasingly required in land use planning in mountain environments. Hazard assessment has the aim to: (1) determine the spatial distribution of debris flow and landslides; (2) predicting their occurrence and impact; and (3) minimizing the impact. This study presented a model for assessing the spatial and temporal occurrence of shallow landslides over large areas. The integration of this model

with (a) an empirical (DEM-based) model for systematic prediction of distributed soil thickness maps (e.g., the model proposed by Catani et al, 2010), and (b) a post-failure propagation model to compute the amount of detached soil and its possible path downslope will provide a tool that may be used predictively to explore the effects of possible future land management activities. The model is therefore relevant to aims (1) and (2) above, through this relevancy, can contribute to meeting aim (3).

Appendix

A combined laboratory and numerical study to assess the role of hillslope boundary conditions on pore-water pressure dynamics.

A.1 Introduction

In attempting to understand the mechanisms controlling stream flow generation processes, hydrologists have largely used trenches and troughs to collect hillslope discharges. Since from the classic experiments of Hewlett and Hibbert (1963) and Dunne and Black (1970), there have been a number of experiments based on the collection of near-surface downslope flows in troughs (e.g., Mosley, 1979; McDonnell, 1990; Turton et al., 1992; Tsuboyama et al., 1994; Woods and Rowe, 1996; Buttle and Turcotte, 1999; Hutchinson and Moore, 2000; Tromp-van Meerveld and McDonnell 2006a). These experiments have produced tangible evidence that subsurface flow processes are important in controlling hillslope runoff (McDonnell, 2003) and have often demonstrated specific triggers for the occurrence of subsurface stormflow. For example, Tromp-van Meerveld and McDonnell (2006b) showed evidence of threshold behaviour in which subsurface stormflow occurs only after perched water tables develop in bedrock depressions at the soil-bedrock interface then connect laterally and feed downslope flow; Woods and Rowe (1996) found that the threshold for rapid stormflow generation was considerably affected by antecedent conditions and rainstorm characteristics; Uchida et al. (2005) argued that the rapid lateral flow is highly threshold dependent and largely via soil pipes located within the transient saturated zone or via discontinuities at the soil–bedrock interface.

However, all of these works have ignored the effect that a trench may produce in terms of subsurface flow direction and runoff generation. Atkinson (1978) is probably the only one who has pointed out the impacts of trenches on the flowlines and pathways. He argued that trenches can involve the variability in contributing areas due to flowline changes at the margins of the trench.

Numerical modelling offers a way to visualise and quantify this effect and provides an

attractive method for exploring different types of boundary conditions in order to understand how the presence of a trench affects hillslope pore pressure dynamics.

Here, a study which combines laboratory and numerical analyses is presented to assess the influence of hillslope boundary conditions on pore-water pressure dynamics. Specifically, the influence of (a) the geometry of the bedrock topography and (b) the boundary condition at the footslope are examined by collecting pore-water pressure data at the soil/bedrock interface of a laboratory hillslope model. Laboratory experiments are then simulated with HYDRUS-3D (Simunek et al., 2006), a three-dimensional Richards' equation solver for variably saturated soil water movement, to obtain a model that behaves consistently with experimental data. Once verified that the results from HYDRUS-3D are in good agreement with laboratory results, HYDRUS-3D itself can be used to investigate pore-water pressure dynamics for different hillslope boundary conditions.

A.2 Material and methods

A.2.1 Little Panola: the experimental laboratory hillslope

The bedrock topographic surface of the experimental Panola hillslope located in Georgia (USA) was found to control routing of subsurface flow (as discussed in Chapter 4 of this Thesis). This hillslope is well known from the study of Freer et al. (2002) and Tromp-van Meerveld and McDonnell (2006b) that measured the surface topography of the hillslope on a 2 meters grid with laser and the depth of the bedrock with a soil corer on the same survey grid.

The importance of the bedrock topography led to the creation of Little Panola, a scaled model of the 46 m-long by 20 m-wide original Panola hillslope. Based on a fixed angle (13° as the real Panola hillslope), Little Panola was built on a table of 3.9 by 1.7 meters with a scale factor of 11.76 to 1 (Figure A.1). The small-scale topography of the bedrock elevation was calculated and designed on the table with a mesh resolution of 0.17 by 0.17 m. This mesh grid was filled with stack of 0.17x0.17 m plywood panels by forming blocks of the calculated heights of the bedrock topography, and was covered with cement and plaster to make the construction impermeable.

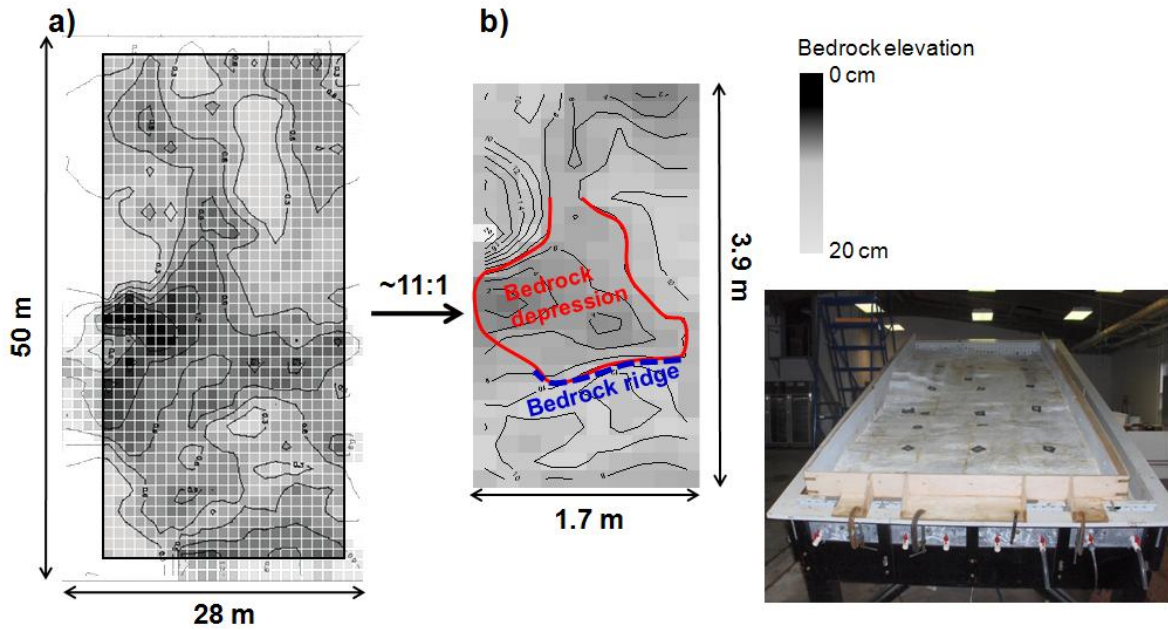


Figure A.1. (a) The geometry of the real Panola hillslope, (b) the topography of Little Panola, and (c) the 11:1 scale model of the Panola hillslope

Figure A.1 shows that in the midslope of Little Panola there is a large depression in the bedrock. This area of deep soils will be called “bedrock depression” in the remainder of this work. Directly downslope of the bedrock depression is a “bedrock ridge” approximately 1 m upslope from the downslope boundary. The downslope boundary of Little Panola is formed by a vertical free face where subsurface flow can drain from Little Panola. Perforated steel with wire mesh was used in the downslope boundary of Little Panola to allow the free movement of water from the laboratory hillslope without washing out soil grains. This boundary condition reproduces the 20 m wide trench excavated at the lower boundary of the real Panola hillslope (Tromp van Meerveld and McDonnell, 2006b).

The soil used in Little Panola was a medium sand. This soil was physically and hydrologically characterized to transfer the experimental results into numerical models. The grading curve of this sand was derived from sieve analysis, while the soil-water retention curve (SWRC) of the soil was inferred by using the automated soil moisture release curve apparatus presented in Vaché et al. (2008). The van Genuchten model (1980) was fitted to measured soil-water retention data using least squares optimization. The saturated hydraulic conductivity of the soil K_{sat} was evaluated in the laboratory with the traditional constant-head test method. Table A.1 summarizes the estimated physical and hydrological parameters of the sandy soil used in Little Panola.

Table A.1: Physical and hydrological parameters of the sandy soil used in Little Panola

Properties	symbol	unit	value
Soil density	ρ	(gcm^{-3})	1.62
Mean grain size	D_{50}	(mm)	0.43
Uniformity coefficient	D_{60}/D_{10}	[-]	2.13
Saturated water content	θ_{sat}	($\text{cm}^3\text{cm}^{-3}$)	0.47
Residual water content	θ_r	($\text{cm}^3\text{cm}^{-3}$)	0.215
α van Genuchten	α	(m^{-1})	4.02
n van Genuchten	n	[-]	4.73
Saturated hydraulic conductivity	K_{sat}	(ms^{-1})	$1.1 \cdot 10^{-4}$

A.2.2 Laboratory instrumentation and data collection

Two independent rainfall simulators (System 1 and System 2) were mounted on Little Panola (Figure A.2a). System 1 consists of 8 nozzles (blue point in Figure A.2b), and is capable of producing a constant 22 mmh^{-1} rainfall intensity. System 2 (dark points in Figure A.2b) is a 15-nozzles rainfall simulator that allow to reproduce a rainfall event with a constant 25 mmh^{-1} rainfall intensity. Therefore, the simultaneous operation of System 1 and System 2 allows to reproduce a 47 mmh^{-1} rainfall intensity (Figure A.2b).

The nozzles were installed at a height of 2.0 m above the surface of the table on a wooden frame (Figure A.2a). Water supply and pressure was by filtered municipal water supplied in combination with a pressure regulator to maintain 2.75 bar (40 psi) at the nozzles. Water was supplied to the nozzles via a flexible hose while a pressure gauge mounted on the line allowed monitoring of water pressure.

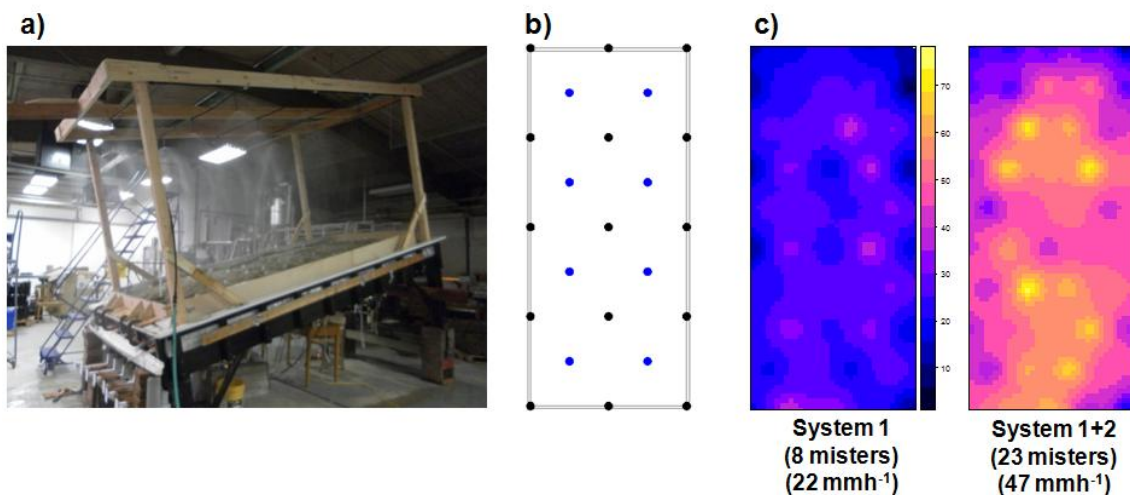


Figure A.2. The rainfall simulator mounted on Little Panola (a). Two independent rainfall systems (b) allowed to reproduce a 22 mmh^{-1} and a 47 mmh^{-1} constant rainfall intensity event

Sixteen electric pore-water pressure transducers were installed on the table (i.e., at the soil/bedrock interface of Little Panola) to measure positive pore water pressure changes in response to rainfall infiltration (Figure A.3). Nine instruments were installed inside the bedrock depression. In particular, sensors 9 and 10 (Pt9 and Pt10 in Figure A.3) were installed in the deepest points of the bedrock surface, and sensor 6 (Pt6 in Figure A.3) was just upslope from the bedrock ridge.

Each pore-water pressure transducer consists of a rust-proof and acid-resistant ceramic filter. Behind the filter is a small water chamber. The water pressure in this chamber is measured by a piezoelectric pressure sensor. Pore-water pressure transducers were connected with cables to three data-loggers located below the table (Figure A.2a). The cables were utilized to transfer measurement data and supply power sources. The three data-loggers allowed recording one pore-water pressure value every 0.5 seconds.

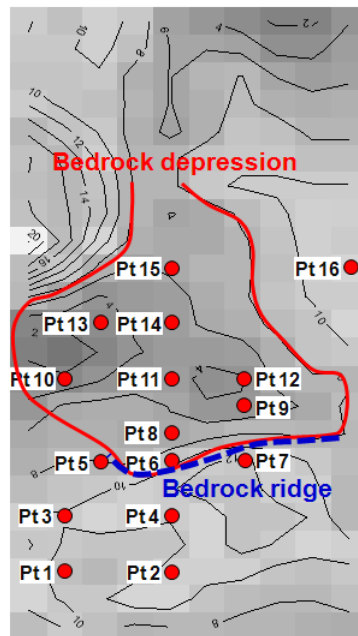


Figure A.3. Location of pore-water pressure transducers at the “soil/bedrock interface” of Little Panola

A.2.3 Set-up of Experiments

Six laboratory experiments that included three slope angles β (6° , 13° , and 23°) and two rainfall events were conducted on Little Panola to investigate the effect of subsurface topography and hillslope angle on pore pressure dynamics during rainfall infiltration. A summary of experiments is shown in Table A.2.

Table A.2: Laboratory experimental conditions

Exp.	Date	Slope angle $\beta(^{\circ})$	Rainfall duration (min)			Total rainfall volume (mm)
			System 1 (22mmh ⁻¹)	System 1 + System 2 (47mmh ⁻¹)	Total	
1	01-03-11	6	75	15	90	39
2	03-03-11	6		50	50	39
3	04-03-11	13	75	15	90	39
4	06-03-11	13		50	50	39
5	11-03-11	23	75	15	90	39
6	14-03-11	23		50	50	39

Different hillslope angles were analyzed as it affected the roughness in the bedrock (Figure A.4). In fact, while the 6°-configuration showed deep depressions in the bedrock surface of Little Panola (Figure A.4a) with a pronounced bedrock ridge (Figure A.3), the 23°-configuration presented a more or less planar bedrock surface, even though a small bedrock ridge was still visible (Figure A.4c).

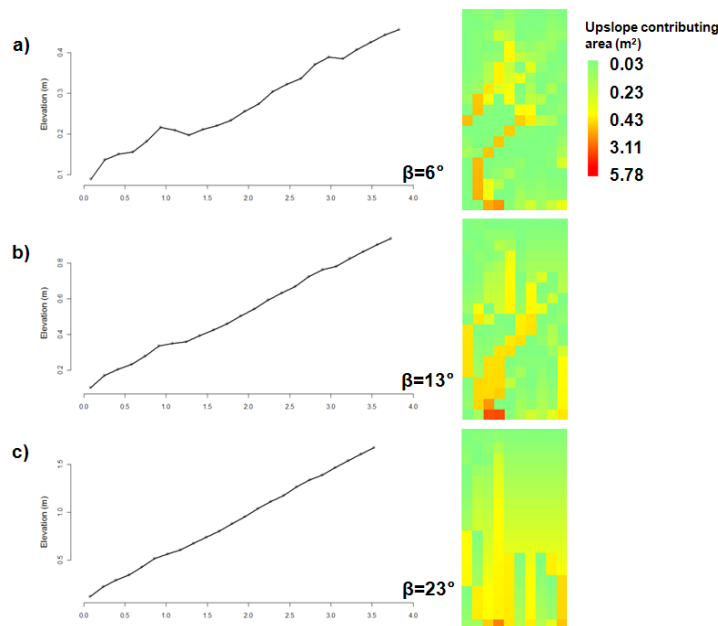


Figure A.4. Bedrock topography at different slope inclination on a representative upslope transect across the hillslope (left). Map of contributing area based on bedrock topography for the three slope angle analyzed (right)

The two simulated rainfall events were characterized by the same cumulative rainfall (39 mm), but different distribution in time (i.e., different values of rainfall intensity and duration). In particular, the first rainfall event was a 90 min-long rainfall event obtained by combining System 1 (22 mmh⁻¹ during the first 75 min) and System 1+ System 2 (47 mmh⁻¹ during the

last 15 min). The second event was a 50 min-long rainfall event with a constant rainfall intensity of 47 mmh^{-1} (System 1+ System 2).

Prior to each experiment, the slope was slowly saturated from below and subsequently drained with a 12 hour drainage period. The pre-saturation stage (and the subsequent drainage) was necessary to avoid development of an unstable wetting front (i.e., fingered flow) during the vertical rain infiltration in dry soil (Selker et al., 1992).

A.3 Results

A few selected results from laboratory measurements are presented here to show the effect of the subsurface topography and hillslope angle on the generation of positive pore pressure at the soil/bedrock interface of Little Panola.

Furthermore, Experiment #5 (in Table A.2) was simulated with HYDRUS-3D to test the numerical model's ability to replicate laboratory experiments. HYDRUS-3D was then used to run a number of virtual experiments investigating the sensitivity of laboratory results to the hillslope boundary conditions, notably to the shape of the bedrock topography and the type of boundary condition at the downslope boundary.

A.3.1 Laboratory results

All the experimental results showed that development of positive pore-water pressure at the soil/bedrock interface was determined largely by the extent of a wedge of saturation from the free face boundary at the base of the slope.

Figure A.5 shows maps of pore-water pressure developed at the soil-bedrock interface of the 6° -slope configuration after 5, 20, 60, 75, and 90 min from the onset of the 90 min-long rainfall experiment (Experiments #1 in Table A.2). At time $t=5$ min only sensors Pt9 and Pt10 (located in the deepest bedrock depression) and sensor Pt6 (located just upslope from the bedrock ridge) indicated development of positive pore-water pressure. After 20 min from the beginning of rainfall sensors Pt1 and Pt2 indicated development of a narrow strip of subsurface saturation at the base of the slope. Subsequently, a wedge of saturated soil extended upslope as indicated in the longitudinal sections A-A' (reported on the right column of Figure A.5). At the end of rainfall ($t=90$ min) this wedge of saturation covered approximately $3/4$ of the bedrock area.

Sensors Pt6 (near the bedrock ridge) and sensor Pt2 (close to the vertical free face boundary) responded simultaneously at the 13° -slope configuration (Experiments #3 in Table A.2 not shown here), while at the steepest (23°) hillslope configuration (Experiment #5 in Table A.2) the first sensor to indicate development of a perched water table were those near the base of the slope (Pt1 and Pt2 in Figure A.6). Sensors Pt6, Pt9, and Pt10 responded only after the

wedge of saturation was extended into the bedrock depression.

Figures A.5 and A.6 show that an increase in slope angle from 6° to 23° lead to a general decrease in the extension of the saturated wedge from $3/4$ to less than $1/2$ of the bedrock area.

Experiments with the 50 min-long rainfall event (Experiments #2, Experiments #4, and Experiments #6 in Table A.2) exhibited the same qualitative behavior as those described for the 90 min-long rainfall event.

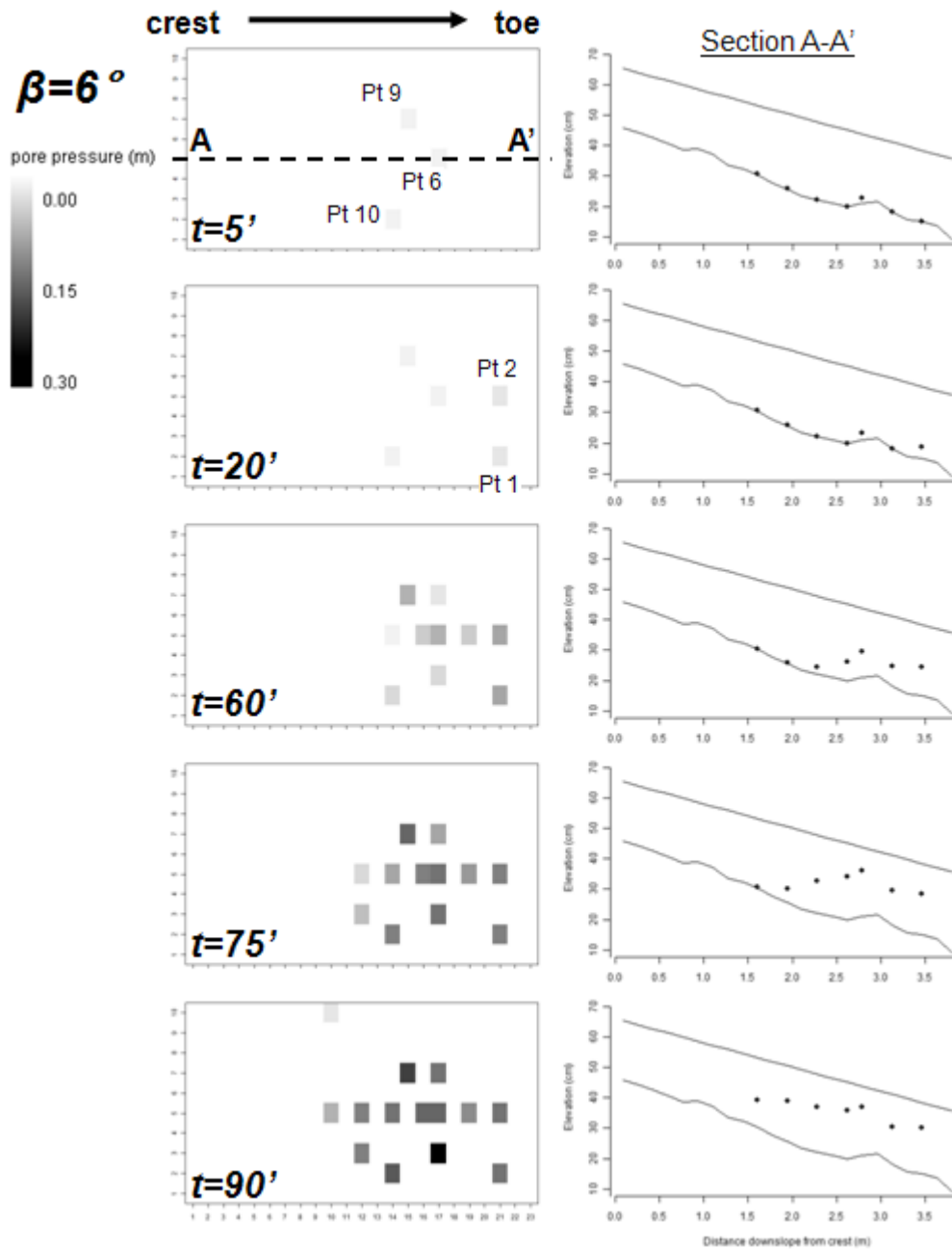


Figure A.5. Experimental pore-water pressure measurements at the soil-bedrock interface of the 6° -configuration of Little Panola

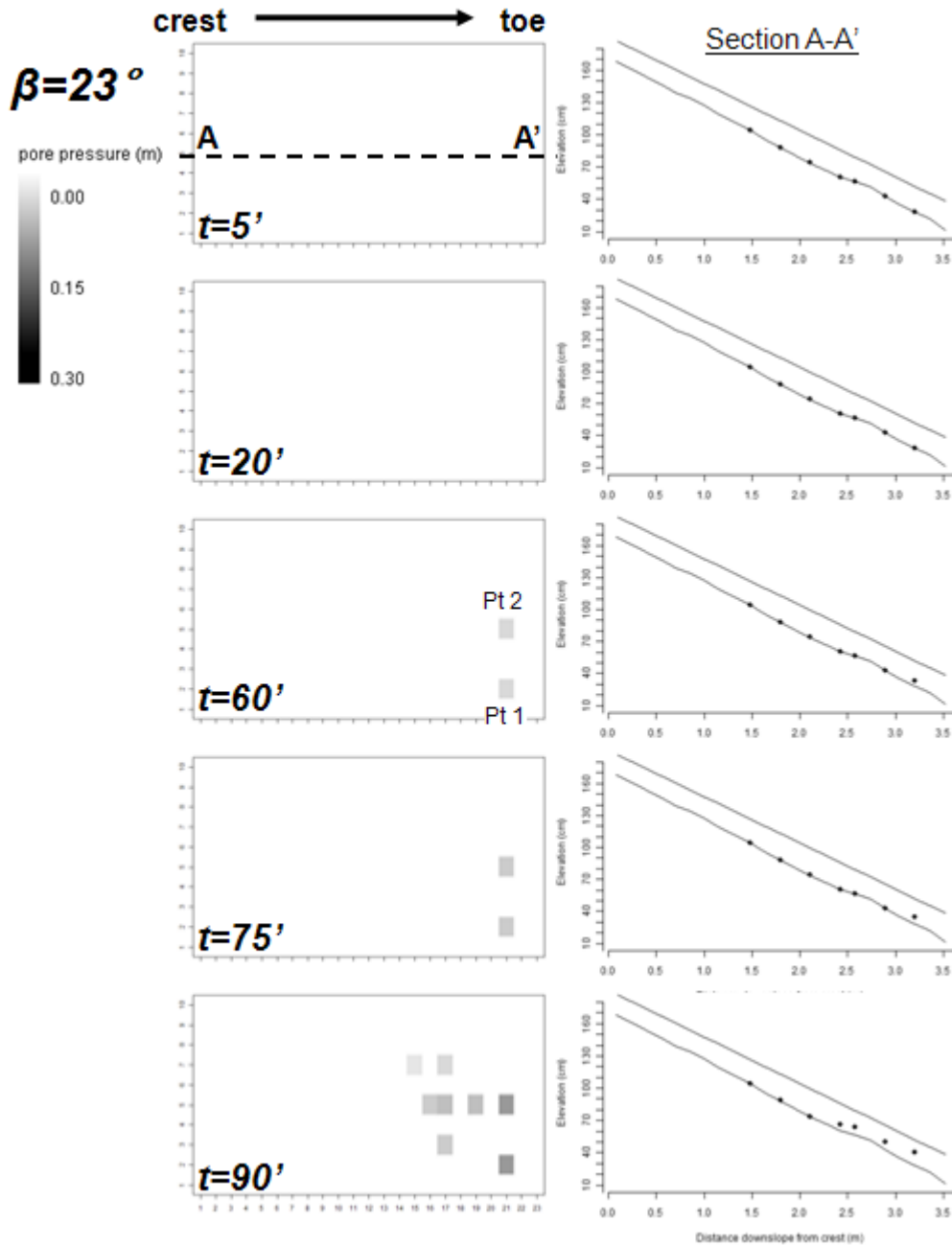


Figure A.6. Experimental pore-water pressure measurements at the soil-bedrock interface of the 23°-configuration of Little Panola

A.3.2 Virtual experiments

The well known finite element model HYDRUS-3D (Simunek et al., 2006) was used to run a number of virtual experiments on Little Panola. HYDRUS-3D model numerically solves the Richards' equation for water flow in variably saturated porous media, and can use the van Genuchten-Mulaem relationships (van Genuchten, 1980) to describe the SWRC and the hydraulic conductivity function (HCF).

A.3.2.1 Base case scenario

The first step was that to verify whether HYDRUS-3D was capable of reproducing experimental results. The objective behind this was to obtain a model that behaved in a realistic way – consistent with experimental data – and not to exactly replicate the laboratory results.

The model domain was generated by importing the 23°-Little Panola DEM (digital elevation model; x, y, z-coordinates of the surface and bedrock topography) into HYDRUS-3D. The finite element mesh for the base case scenario contained 17,100 nodes, arranged in twenty mesh layers and resulting in 90,288 3D elements in the form of triangular prisms. The spacing between nodes in horizontal direction within one mesh layer was 0.17 m (i.e., the grid resolution). The thickness of the entire model domain ranged from 0.09 to 0.31 m (with a mean value of 0.22 m), depending on the topography of the bedrock surface.

Hydraulic properties of soil were described with the van Genuchten–Mualem soil hydraulic model (van Genuchten, 1980) by using the laboratory results presented in Section A.2.1 and Table A.1.

Boundary conditions were assigned to reproduce the laboratory conditions: an atmospheric boundary (i.e., rainfall rate) was assumed at the soil surface (i.e., upper boundary of the numerical domain), a potential seepage face boundary was assumed at the downslope end of the hillslope (the face was treated as a prescribed pressure head boundary with $\psi=0$, while the unsaturated part was treated as a no-flux boundary), and no-flux boundaries were assumed at the soil/bedrock interface and at the upslope and side boundaries. Initial conditions were defined by assuming a fully saturated soil profile, followed by a 12 hour drainage period without atmospheric input prior to the start of the actual 90 min-long rainfall event (22 mmh⁻¹ for the first 75 min, and 47 mmh⁻¹ for the last 15 min). This corresponded to actual laboratory conditions. The total simulation time was 18 hours (12 hours of pre-drainage, 1.5 h of rainfall, and 4.5 h of post-drainage) and numerical results were printed each 15 min.

Time series of pressure heads at the locations within the model domain that corresponded approximately to the location of the laboratory pore pressure transducers were compared to laboratory observations. Laboratory instrumentations only recorded positive pore pressure, while HYDRUS-3D simulates both negative and positive pore-water pressure. Figure A.7 shows the results of the testing of the numerical model against instrumentation readings for the instrumented points located along the transect A-A'. When tested against the experiments, the numerical model performed reasonably well in all cases. Although model performance evaluation was not possible in the negative pore pressure zone, the comparison showed that the numerical model was able to reproduce the exact time of development of positive pore pressure at Points 4, 6, and 8. The model did not match the observations very well at Point 2, where development of positive pore pressure was delayed with respect to

experimental data and the peak of pore pressure (at $t=90$ min) was less pronounced. Furthermore, numerical results simulated a slower drainage after rains than experimental data. Consistently with laboratory data, model results did not show development of positive pore pressure at Points 14 and 15 that, in fact, remained unsaturated during the whole rainfall period.

Even if the comparison of absolute values showed some disagreement in some cases, the model reproduced experimental data of pore pressure dynamics in general very well, confirming that the base case scenario captured the major internal flow behavior. Numerical simulations were consistent with the experimental mechanistic behavior and reproduced the pressure wave advance form the hillslope toe (Figures A.8b, c, d, e), and the subsequent subsurface drainage (Figures A.8f, g, h) that were observed in the laboratory.

Thus, the numerical model was assumed to be a solid foundation for exploration different hillslope boundary conditions than those used in the laboratory experiments.

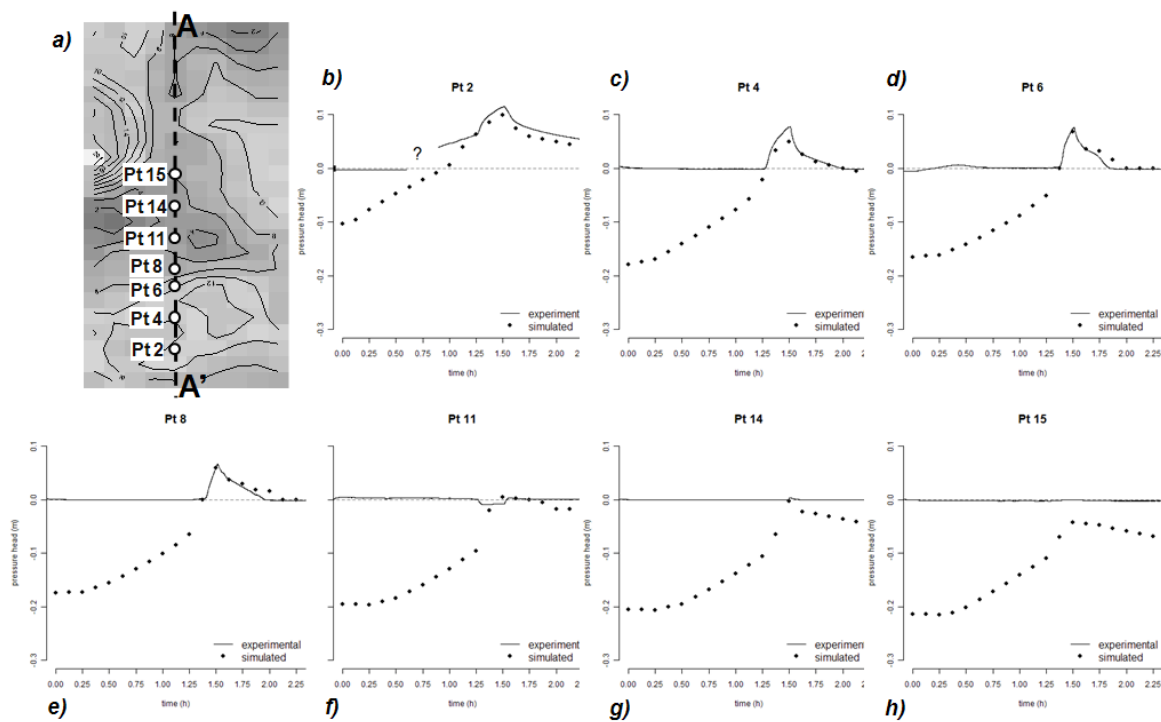


Figure A.7. Temporal evolution of experimental versus simulated values of pore-water pressure at different points. Pore-water pressures are measured at the soil/bedrock interface of Little Panola

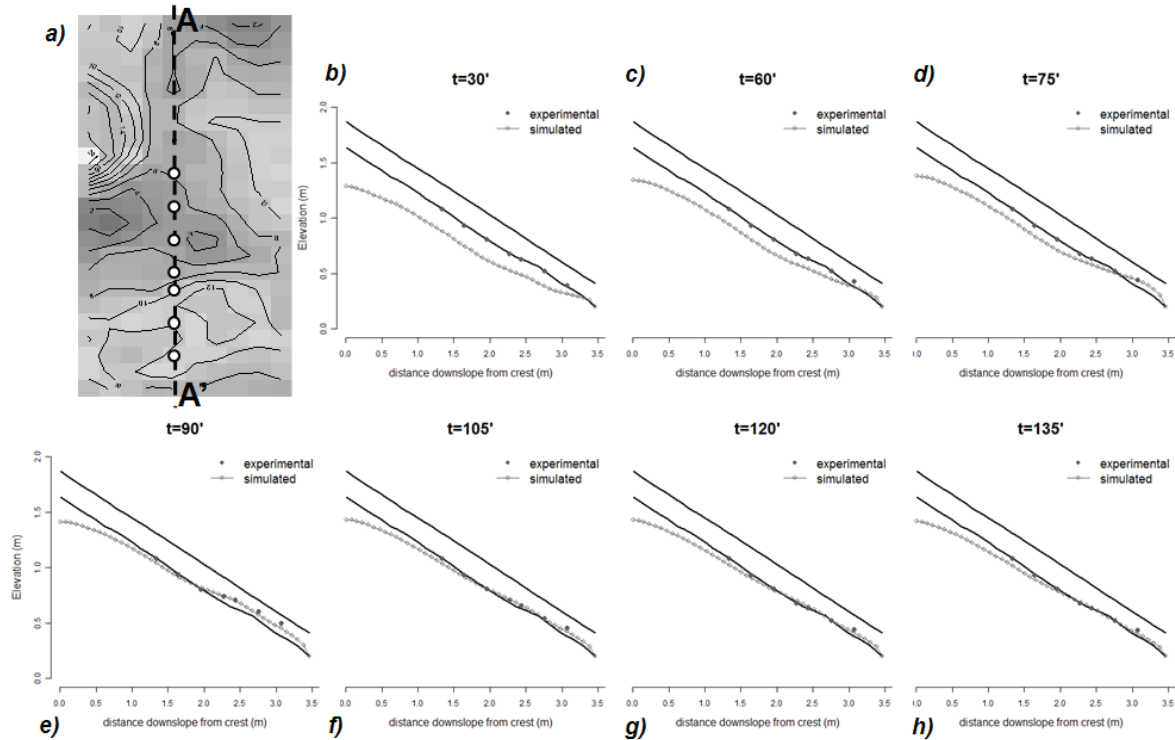


Figure A.8. Experimental and simulated values of pore-water pressure at different locations and at different times from the onset of rainfall along the transect A-A'. Pore-water pressures are measured at the soil/bedrock interface

A.3.2.2 Variation of boundary conditions

Using the base case described above, HYDRUS-3D was used to explore the dynamics of pore pressure under different hillslope boundary conditions.

In particular, the numerical experiments explored:

- (a) the role of the shape of the bedrock topography, by comparing the base case scenario (irregular bedrock shape) to a “regularized” (i.e., planar) bedrock topography. This allowed to assess the role played by the bedrock depression on the pore pressure dynamics;
- (b) the role of the free-face downslope boundary condition, by investigating the hydrological behavior of the upper 1/3 part of a three times longer hillslope (hereafter called long-hillslope) than the original Little Panola. This reproduces the condition without the presence of a trench at downslope boundary and, therefore, allowed to understand whether the free-face at the downslope boundary of Little Panola affected the upslope pore pressure dynamics.

Figure A.9 shows simulated patterns of pore pressure at the soil/bedrock interface for the base case scenario (irregular bedrock topography and free-face downslope boundary condition in Figure A.9a), and the modified settings (Figures A.9b, c, d). Maps of pore

pressure in each subfigure refer at different times during the simulated rainfall event (60 min, 75 min, and 90 min from the onset of rainfall). Specifically, maps in Figures A.9c and A.9d only focus on the upper 1/3 part of the hillslope corresponding to the length of Little Panola.

The numerical results show that the free face at the downslope boundary of the 23°-Little Panola induced a wedge of saturation that hid the effect of the bedrock depression in the midslope (Figure A.9a versus Figure A.9c). In fact, the numerical experiments performed on the long-hillslope (Figure A.9c) showed that the bedrock ridge, by preventing the free downslope drainage, induced development of positive pore pressures into the bedrock depression. Moreover, the region downslope from the bedrock ridge of the long-hillslope (Figure A.9c) exhibited unsaturated conditions, indicating that the bedrock depressions acted to collect the soil-water from upslope area.

Equipotential lines at the planar bedrock topography were orthogonal to the slope direction (Figures A.9b and A.9d), while the bedrock depression induced complex pore pressure patterns with high pore pressure values in the midslope (Figures A.9a and A.9c).

The zone of positive pore pressure indicated in Figure A.9d (long-hillslope with planar topography) at time $t=90$ min was induced by incoming subsurface flow from upslope positions. This differs from results obtained with the free-face downslope boundary condition (Figure A.9b) where back water effects due to development of a wedge of saturated soil distorted the net of hydraulic potential on the slope.

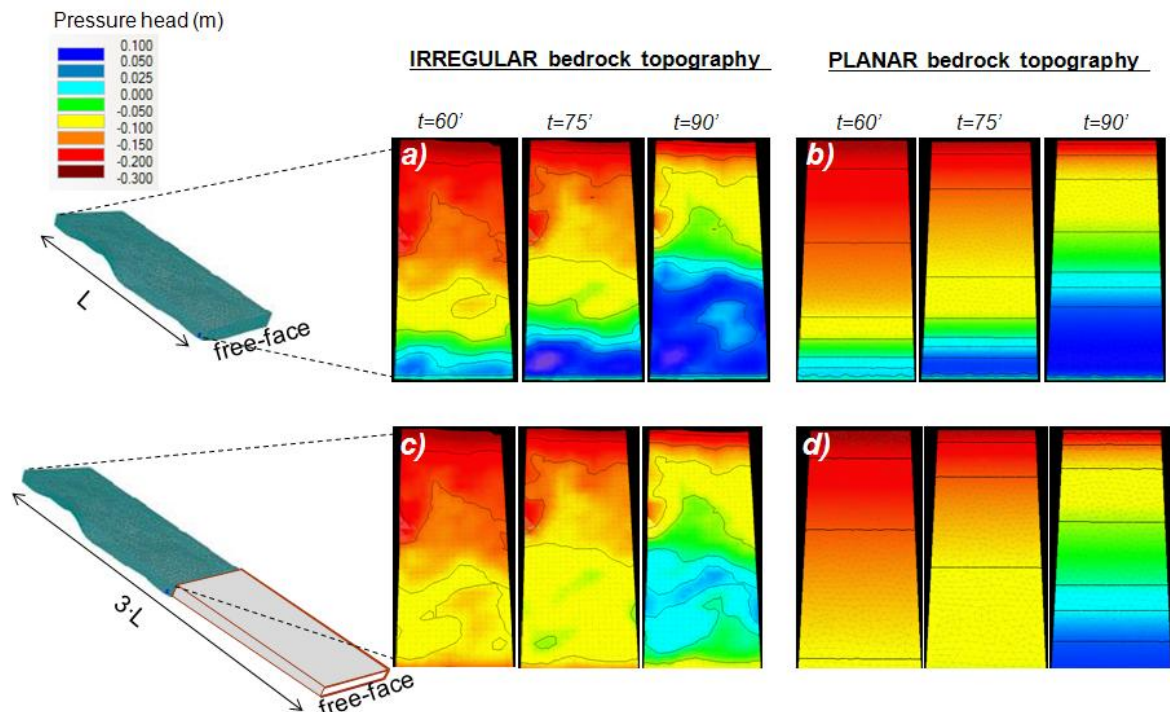


Figure A.9. Numerical experiments exploring the effect of the downslope boundary condition and the shape of the subsurface topography on pore-water pressure dynamics at the soil/bedrock interface of Little Panola

A.4 Discussion

The free-face at the downslope boundary of Little Panola has the same effect as a trench at the footslope. This exposed free-face of soil distorts the net of hydraulic potential by involving the formation of a wedge of saturated soil upslope of the face.

Figure A.10 shows a simplified sketch of a slope profile with and without a trench. With the presence of a trench, water is unable to leave the free-face until sufficient flow from upslope has accumulated to saturate the soil (Figure A.10a). This is because soil-water at the free face must be at atmospheric pressure (i.e., saturated conditions) in order to leave the pore space of the soil and flow away (Atkinson, 1978). Inevitably, if the soil at the face itself is saturated, a wedge of saturated soil will extend upslope, perhaps into soil which would not normally be saturated had an artificial free face not been constructed (Figure A.10b). The extent and the thickness of the saturated wedge is dependent upon the flux from upslope and changes as the hillslope inclination changes (Figures A.5 and A.6).

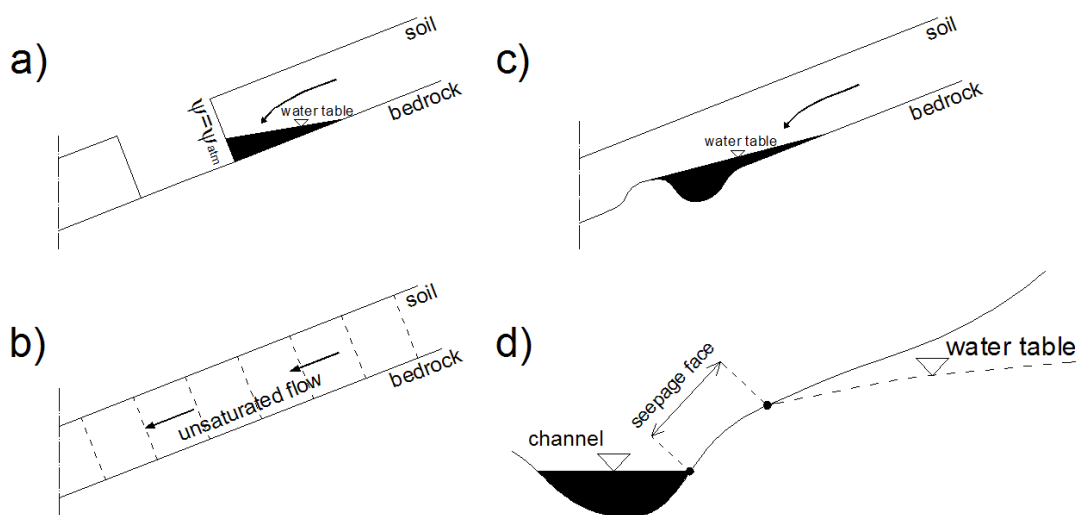


Figure A.10. Effect of a free-face at the footslope in distorting unsaturated downslope flow (a and b). Influence of depressions in the bedrock surface (c), and the backwater effect at the bank of a stream (d)

Backwater effect can also generate from micro-topographic reliefs in the bedrock topographic surface (Figure A.10c). Depressions in the bedrock act as impedances for the downslope drainage of perched water and induce localized increase of positive pore-water pressure. However, despite the fact that bedrock topography and soil depth variability are important controls on subsurface hydrological processes, few models have conceptualized and implemented this into simulation models. Weiler and McDonnell (2004) incorporated soil depth variability into a subsurface flow model and simulated subsurface stormflow for the Panola hillslope. They could show that soil depth variations not only have a large

influence on the spatial variation of subsurface flow but control largely the total subsurface flow volume produced. Lanni et al. (2012) used the same Panola hillslope to show how the micro-topographic depressions in the bedrock surface may control the abrupt triggering of landslide processes. Thus, our results are consistent with previous studies in showing that the shape of the bedrock topography is important for determining the hydrological and geomorphologic response of hillslopes to storm events.

Wedge of saturation may occur in nature at the bank of a stream (Figure A.10d) causing a backwater effect that distorts the net of hydraulic potential on the hillslope. This mechanism is intimately related to the hydrological connectivity between the channels network and the surrounding hillslopes but even though it is not considered at all in most of the catchment-scale rainfall-runoff models. For example, topographic wetness index-based rainfall-runoff models (e.g., TOPMODEL by Beven and Kirkby, 1979) make the assumption that local drainage is not affected by downslope topography constraints. More generally, all models based on the kinematic wave approach cannot reproduce backwater effect.

Physically-based numerical models can be used successfully for examining the role of the conditions at the model boundaries, but only under conditions of ‘comprehensive data availability’ (Brontstert, 1999) where all relevant processes are accounted for and where there are sufficient knowledge of the real (i.e., field) conditions at the model boundaries (Cloke et al., 2003). Correct selection of boundary conditions is a critical step in model design (Anderson and Woessner, 1992): if a system is simulated based upon incorrect configuration decisions, then the numerical simulation is solving the wrong problem and, by definition, will provide the wrong solution (Franke and Reilly, 1987). The choice of a “wrong” boundary conditions can alters hydrological processes dynamics, and different side slope boundary conditions yield different pore pressure regimes, as demonstrated by the numerical experiments in Figure A.9.

A.5 Conclusions

This study has combined laboratory and numerical analyses to assess the role of hillslope boundary conditions, notably at the bottom boundary (i.e., soil/bedrock interface) and at the downslope boundary, on pore-water pressure dynamics.

The results have shown that the presence of a trench at the foot of a slope may distort the net of hydraulic potential by involving the formation of a wedge of saturated soil upslope of the face. This, in turn, may results in distorted hydrographs compared to conditions without a trench in the middle of a slope profile. Bedrock depressions in the subsurface topographic surface play an important role on pore-water pressure dynamics, acting as impedance for the downslope drainage of perched water. This result has confirmed findings from previous field (e.g., Freer et al., 2002; Tromp van Meerveld and McDonnell, 2006b) and numerical (e.g.,

Hopp and McDonnell, 2009; Lanni et al., 2012) studies that the spatial distribution of soil depth is a strong control on local pore pressure dynamics.

The combined laboratory/numerical approach in this study revealed a powerful tool to extend laboratory experiments to others settings that are not possible (for economic or practical reasons) to explore in the laboratory. This approach also allows understanding of results and limitations of laboratory (and field) settings.

However, on its own, numerical models' results are strongly conditioned by internal model configuration decisions (e.g., boundary conditions). The discussions presented in this work emphasize the importance of selecting appropriate internal model configurations for the numerical representation of hillslope pore pressure dynamics. Decisions on the architecture of the model need to be explored fully prior to numerical hillslope models being used for process inference. The dialogue between the experimentalist (who has some understanding of how the system 'works') and the modeler (who understands how the code 'works') is a necessary step for a correct model conceptualization and configuration.

Bibliography

- Acharya G, Smedt F, Long, NT. 2006. Assessing landslide hazard in GIS: a case study from Rasuwa, Nepal. *Bulletin of Engineering Geology and the Environment* 65, 99-107.
- Ahrendt A, Zuquette L. 2003. Triggering factors of landslides in Campos do Jordão city, Brazil.
- Aleotti P, Chowdhury R, 1999. Landslide hazard assessment: summary review and new perspectives. *Bulletin of Engineering Geology and the Environment* 58, 21-44.
- Aleotti P. 2004. A warning system for rainfall-induced shallow failures. *Engineering Geology* 73: 247-265
- Ali GA, Roy AG. 2010. Shopping for Hydrologically Representative Connectivity Metrics in a Humid Temperate Forested Catchment. *Water Resour. Res.* 46. W12544. doi:10.1029/2010WR009442.
- Amore E, Modica C, Nearing MA, Santoro VC. 2004. Scale effect in USLE and WEPP application for soil erosion computation from three Sicilian basins. *Journal of Hydrology* 293, 100–114.
- Anderson SA, Sitar N. 1995. Analysis of rainfall-induced debris flows. *Journal of Geotechnical Engineering* 121 (7): 544-552.
- Anderson MP, Woessner WW. 1992 The role of the postaudit in model validation. *Advances in Water Resources* 15(3): 167-173.
- Antoine M, Javaux M, Biielders C. 2009. What indicators can capture runoff relevant connectivity properties of the micro-topography at the plot scale?. *Adv. Water Resour.* 32, 1297–1310. doi:10.1016/j.advwatres.2009.05.006.
- Arnone E, Noto LV, Lepore C, Bras RL. 2011. Physically-based and distributed approach to analyze rainfall-triggered landslides at watershed scale. *Geomorphology* 133: 121–131.
- Atkinson TC. Techniques for measuring subsurface flow on hillslopes. In *Hillslope Hydrology*, edited by M. J. Kirkby, pp. 73– 120, John Wiley, New York, 1978.
- Avolio MV, Di Gregorio S, Mantovani F, Pasuto A, Rongo R, Silvano S, Spataro W. 2000. Simulation of the 1992 Tessina landslide by a cellular automata model and future hazard scenarios. *JAG* 2:41–50.
- Bak P, Tang C, Wiesenfeld K. 1987. Self-organized criticality: an explanation of 1/f noise. *Phys. Rev. Lett.* 147: 297-300.
- Barling RD, Moore ID, Grayson RB. 1994. A quasi-dynamic wetness index for characterizing the spatial distribution of zones of surface saturation and soil water content. *Water Resour. Res.* 30(4).
- Baum R, Coe J, Godt J, Harp E, Reid M, Savage W, Schulz W, Brien D, Chleborad A, McKenna J, Michael J. 2005. Regional landslide-hazard assessment for Seattle, Washington, USA. *Landslides* 2(4): 266-279.
- Baum RL, Godt JW, Savage, WZ. 2010. Estimating the timing and location of shallow

- rainfall-induced landslides using a model for transient, unsaturated infiltration. *J. Geophys. Res.* 115. Doi:10.1029/2009JF001321
- Baum RL, Savage WZ, Godt JW. 2008. TRIGRS—A FORTRAN program for transient rainfall infiltration and grid based regional slope stability analysis, version 2.0, U.S. Geol. Surv. Open File Rep. 2008 1159, 74 p.
- Berti M, Simoni A. 2005. Experimental evidences and numerical modelling of debris flow initiated by channel runoff. *Landslides* 2(3): 171-182
- Beven KJ, Kirkby MJ. 1979. A physically based variable contributing area model of basin hydrology. *Hydrology Science Bulletin* 24(1), 43–69.
- Beven K, Freer J. 2001. A dynamic TOPMODEL. *Hydrological Processes* 15, 1993–2011. DOI: 10.1002/hyp.252.
- Beven KJ, Moore ID. 1993. Terrain analysis and distributed modelling in hydrology. John Wiley & Sons, New York, 249 pp.
- Bierkens M. 1998. Modeling water table fluctuations by means of a stochastic differential equation. *Water Resources Research* 34: 2485-2499.
- Birkel C, Tetzlaff D, Dunn SM, Soulsby C. 2010. Towards simple dynamic process conceptualization in rainfall runoff models using multi-criteria calibration and tracers in temperate, upland catchments. *Hydrological Processes* 24: 260-275.
- Birkel C, Tetzlaff D, Dunn SM, Soulsby C. 2011. Using time domain and geographic source tracers to conceptualise streamflow generation processes in lumped rainfall-runoff models. *Water Resources Research*. 47. W02515. Doi:10.1029/2010WR009547.
- Bishop AW. 1959. The principle of effective stress. *Tek. Ukebl.* 106(39), 859–863.
- Borga M, Dalla Fontana G, Cazorzi F. 2002. Analysis of topographic and climatologic control on rainfall-triggered shallow landsliding using a quasi-dynamic wetness index. *Journal of Hydrology* 268, 56–71.
- Borga M, Dalla Fontana G, Vezzani C. 2005. Regional rainfall depth-duration-frequency equations for an alpine region. *Natural Hazards* 36: 221-235.
- Borja RI, White JA. 2010. Continuum deformation and stability analyses of a steep hillside slope under rainfall infiltration. *Acta Geotechnica* 5:1–14. DOI 10.1007/s11440-009-0108-1.
- Bracken LJ, Croke JC. 2007. The concept of hydrological connectivity and its contribution to understanding runoff-dominated geomorphic systems. *Hydrol. Processes* 21, 1749– 1763. doi:10.1002/hyp.6313.
- Brontstert A. 1999. Capabilities and limitations of detailed hillslope hydrological modelling. *Hydrological Processes* 13(1): 21–48.
- Brugnano L, Casulli V. 2009. Iterative Solution of Piecewise Linear Systems and Applications to Flows in Porous Media. *SIAM J. on Scientific Computing* 31: 1858–1873.
- Brooks KN, Ffolliott PF, Gregersen HM, DeBano LF. 1991. Hydrology and the management of watersheds. Iowa State University Press, Ames, Iowa, USA, 392 pp.
- Buckingham E. 1907. Studies on the movement of soil moisture. US Department of Agriculture Bureau of Soils, Government Printing Office, Bulletin 38 (1907) Washington, DC.

- Burlando P, Rosso R. 1996. Scaling and multiscaling models of depth–duration–frequency curves from storm precipitation. *Journal of Hydrology* 187: 45–64.
- Burt TP, Butcher DP. 1986. Development of topographic indices for use in semi-distributed hillslope runoff models. *Zeitschrift für Geomorphologie* 58, 1–19.
- Burt TP, Butcher DP. 1985. Topographic controls of soil moisture distributions. *J. Soil Sci.* 36: 469 – 486.
- Buttle JM, Dillon PJ, Eerkes GR. 2004. Hydrologic coupling of slopes, riparian zones and streams: an example from the Canadian Shield. *Journal of Hydrology* 287: 161–177.
- Buttle JM, Turcotte DS. 1999. Runoff processes on a forested slope on the Canadian shield. *Nord. Hydrol.* 30: 1 – 20.
- Caine N. 1980. The rainfall intensity-duration control of shallow landslides and debris flows. *Geogr Ann* 62:23–27.
- de Campos TM, Andrade MHN, Gerscovich DMS, Vargas JR. 1994. Analysis of the Failure of an Unsaturated Gneissic Residual Soil Slope in Rio de Janeiro, Brazil. 1st. Pan American Symposium of Landslides - Guayaquil, Ecuador, vol.I, pp.201-213.
- Capparelli G, Versace P. 2010. FLAIR and SUSHI: two mathematical models for early warning of landslides induced by rainfall. *Landslides* 8, 67–79.
- Carson MA, Kirkby MJ. 1972. Hillslope form and process. University Press: Cambridge, England; 475.
- Casadei M, Dietrich WE, Miller NL. 2003. Testing a model for predicting the timing and location of shallow landslide initiation in soil-mantled landscapes. *Earth Surface Processes and Landforms* 28, 925–950. doi: 10.1002/esp.470.
- Catani F, Segoni S, Falorni G. 2010. An empirical geomorphology-based approach to the spatial prediction of soil thickness at catchment scale. *Water Resour. Res.* 46(5). Doi: 10.1029/2008WR007450.
- Cernica JN, 1995. Geotechnical engineering: soil mechanics. John Wiley & Sons New York, 453 pp.
- Cochrane and Flanagan, 1999
- Claessens L. 2007. Modelling the location of shallow landslides and their effects on landscape dynamics in large watersheds: An application for Northern New Zealand. *Geomorphology* 87:16-27
- Clerici A, Perego S. 2000. Simulation of the Parma River blockage by the Corniglio landslide (Northern Italy). *Geomorphology* 33:1–23.
- Cloke HL, Renaud J-P, Claxton AJ, McDonnell JJ, Andersona MG, Blake JR, Bates PD. 2003. The effect of model configuration on modelled hillslope–riparian interactions. *Journal of Hydrology* 279: 167–181.
- Cohen J. 1960. A coefficient of agreement for nominal scales. *Educational and Psychological Measurement* 20: 37- 46.
- Collins BD, Znidarcic D (2004) Stability analyses of rainfall induced landslides. *J Geotech Geoenviron Eng* 130(4):362–372.
- Cordano E, Rigon R. A mass-conservative method for the integration of the two-dimensional

- groundwater (Boussinesq) equation. Submitted Water Resour. Res.
- Crave A, Gascuel-Oudoux C. 1997. The influence of topography on time and space distribution of soil surface water content. *Hydrological Processes* 11, 203–210.
- Crosta GB, Frattini P. 2003. Distributed modeling of shallow landslides triggered by intense rainfall. *Nat Hazards Earth Syst Sci* 3:81–93.
- Cruden DM. 1991. A simple definition of a landslide. *Bulletin of the International Association of Engineering Geology* 43, 27–29.
- Corominas J. 2000. Landslides and climate. 8th International Symposium on Landslides. Cardiff, Wales, UK. 33 pp. Keynote Lecturers, 2001.CD-Rom.
- Crozier MJ. 2005. Multiple occurrence regional landslide events in New Zealand: hazard management issues. *Landslides* 2: 247–256.
- D’Ambrosio D, Di Gregorio S, Iovine G, Lupiano V, Rongo R, Spataro W. 2003. First simulations of the Sarno debris flows through cellular automata modeling. *Geomorphology* 54:91–117.
- Del Prete M, Guadagno FM, Hawkins AB. 1998. Preliminary report on the landslides of 5 May 1998, Campania, southern Italy. *Bulletin of Engineering Geology and the Environment* 57(2): 1435-9529.
- Dietrich WE, Bellugi D, Real de Asua R. 2001. Validation of the shallow landslide model SHALSTAB for forest management. In: Wigmosta, M.S., Burges, S.J. (Eds.), *Land Use and Watersheds: Human influence on hydrology and geomorphology in urban and forest areas: American Geophysical Union Water Science and Application*, 2, pp. 195–227.
- Dietrich WE, McKean J, Bellugi D, Perron T. 2007. The prediction of shallow landslide location and size using a multidimensional landslide analysis in a digital terrain model. *Proceedings of the Fourth International Conference on Debris-Flow Hazards Mitigation: Mechanics, Prediction, and Assessment (DFHM-4)*; Chengdu, China.
- D’Odorico P, Fagherazzi S, Rigon R. 2005. Potential for landsliding: Dependence on hyetograph characteristics. *Journal of Geophysical Research* 110. DOI: 10.1029/2004JF000127.
- Dunne T, Black RD. 1970. An experimental investigation of runoff production in permeable soil. *Water Resources Research* 6: 478-490.
- Dutton A, Loague K, Wemple BC. 2005. Simulated effect of a forest road on near-surface hydrologic response and slope stability. *Earth Surface Processes and Landforms* 30: 325–338.
- Ebel BA, Loague K, VanderKwaak JE, Dietrich WE, Montgomery DR, Torres R, Anderson SP. 2007. Near-surface hydrologic response for a steep, unchanneled catchment near Coos Bay, Oregon: 2 physics-based simulations. *Am J Sci* 307:709–748. doi:102475/04200703
- Escario D, Juca J. 1989. Strength and Deformation of partly saturated soils. *Proceedings of the 12th ICSMFE, Rio de Janeiro*, vol.3: 43-46.
- Fenicia F, McDonnell JJ, Savenije HHG. 2008. Learning from model improvement: On the contribution of complementary data to process understanding. *Water Resour. Res.* 44. W06419. Doi:10.1029/2007WR006386.
- Franke OK, Reilly TE. 1987. The effects of boundary conditions on the steady-state response of three hypothetical groundwater systems—results and implications of numerical experiments. *US*

- Geological Survey Water Supply Paper 2315, 19.
- Fredlund DG, Rahardjo H. 1993. *Soil Mechanics for Unsaturated Soils*, John Wiley & Sons, New York, 517 pp.
- Fredlund D, Morgenstern NR, Widger RA. 1978. Shear state variables of unsaturated soil. *ASCE J. Geotech. J.* 15 (13): 447-466.
- Fredlund DG, Xing A. 1994. Equations for the soil-water characteristic curve. *Can Geotech. J.* 31: 521-532.
- Freeman TG. 1991. Calculating catchment area with divergent flow based on regular grid. *Computers and Geosciences* 17: 413-422.
- Freer J, McDonnell JJ, Beven KJ, Peters NE, Burns DA, Hooper RP, Aulenbach B, Kendall C. 2002. The role of bedrock topography on subsurface storm flow, *Water Resources Research* 38: 1269.
- Gallant JC, Hutchinson MF. 2011. A differential equation for specific catchment area. *Water Resour. Res.* 47. Doi:10.1029/2009WR008540.
- Gan JKM, Fredlund DG. 1988. Multistage direct shear testing of unsaturated soils. *American Society for Testing Materials, Geotechnical Testing Journal* 11(2): 132-138.
- Gardner WR. 1958. Some steady state solutions of unsaturated moisture flow equations with applications to evaporation from a water table. *Soil Sci.* 85(4): 228-232.
- Glade T. 1998. Establishing the frequency and magnitude of landslide-triggering rainstorm events in New Zealand. *Environmental Geology* 35: 2-3.
- Godt JW, Baum RL, Savage WZ, Salciarini D, Schulz WH, Harp EL. 2008. Transient deterministic shallow landslide modeling: Requirements for susceptibility and hazard assessments in a GIS framework. *Engineering Geology* 102: 214-226.
- Godt JW, Baum RL, Lu N. 2009. Landsliding in partially saturated materials. *Geophys Res Lett* 36.
- Grabs T, Seibert J, Bishop K, Laudon H. 2009. Modeling spatial patterns of saturated areas: A comparison of the topographic wetness index and a dynamic distributed model. *Journal of Hydrology* 373(1-2), 15-23.
- Graham CB, Woods RA, McDonnell JJ. 2010. Hillslope threshold response to rainfall: (1) A field based forensic approach. *Journal of Hydrology* 393(1-2): 65-76. DOI: 10.1016/j.jhydrol.2009.12.015.
- Graham J. 1984. Methods of stability analysis. In: D. Brunsten and D.B. Prior (Editors), *Slope Instability*. Wiley & Sons, New York, pp. 171-215.
- Grayson RB, Western AW, Chiew FHS, Blöschl G. 1997. Preferred states in spatial soil moisture patterns: local and nonlocal controls. *Water Resour. Res.* 33(12), 2897-2908. Doi:10.1029/97WR02174.
- Gregoretti C, dalla Fontana GD. 2008. The triggering of debris flow due to channel-bed failure in some alpine headwater basins of the Dolomites: analyses of critical runoff. *Hydrological Processes* 22: 2248-2263. doi: 10.1002/hyp.6821.
- Green WH, Ampt GA. 1911. Studies on soil physics: 1. the flow of air and water through soil. *Journal of Agricultural Science* 4, 1-24.
- Güntner A, Seibert J, Uhlenbrook S. 2004. Modeling spatial patterns of saturated areas: An evaluation

- of different terrain indices. *Water Resour. Res.* 40. DOI:10.1029/2003WR002864.
- Guthrie RH, Deadman PJ, Cabrera AR, Evans SG. 2007. Exploring the magnitude–frequency distribution: a cellular automata model for landslides. *Landslides* 5:151–159. DOI: 10.1007/s10346-007-0104-1.
- Guzzetti F, Ardizzone F, Cardinali M, Galli M, Reichenbach P, Rossi M. 2008. Distribution of landslides in the Upper Tiber River basin, central Italy. *Geomorphology* 96: 105–122.
- Haitjema HM, Mitchell-Bruker S. 2005. Are water tables a subdued replica of the topography? *Ground Water* 43 (6):781–786.
- Hawke R, McConchie J, 2009. In situ measurement of soil moisture and pore-water pressures in an 'incipient' landslide: Lake Tutira, New Zealand. *Journal of Environmental Management* 92(2).
- Heppner CS, Loague K, VanderKwaak JE. 2007. Long-term InHM simulations of hydrologic response and sediment transport for the R-5 catchment. *Earth Surface Processes and Landforms* 32: 1273–1292.
- Hewlett JD, Hibbert AR. 1963. Moisture and energy conditions within a sloping soil mass during drainage. *J. Geophys. Res.* 68, 1081 – 1087.
- Hewlett JD, Hibbert AR. 1967. Factors affecting the response of small watersheds to precipitation in humid areas, *Forest Hydrology*, edited by Sopper WE. and Lull HW., New York: Pergamon Press: 275-290.
- Hilberts A, Van Loon EE, Troch PA, Paniconi C. 2004. The hillslope-storage Boussinesq model for non-constant bedrock slope. *Journal of Hydrology* 291: 160 –173.
- Hilberts A, Troch P, Paniconi C. 2005. Storage-dependent drainable porosity for complex hillslopes. *Water Resour. Res.* 41. W06001.
- Hilberts, A.G.J. Low-dimensional modeling of hillslope subsurface flow processes Developing and testing the hillslope-storage Boussinesq model. Dissertation Wageningen Universiteit, Wageningen, 2006. ISBN 90-8504-516-9
- Hutchinson DG, Moore RD. 2000. Throughflow variability on a forested hillslope underlain by compacted glacial till. *Hydrol. Processes* 14: 1751– 1766.
- Hjerdt KN, McDonnell JJ, Seibert J, Rodhe A. 2004. A new topographic index to quantify downslope controls on local drainage. *Water Resour. Res.* 40, W05602. DOI:10.1029/2004WR003130.
- Ho J-Y, Lee KT, Chang TC, Wang ZY, Liao Y-H. 2011. Influences of spatial distribution of soil thickness on shallow landslide prediction. *Engineering Geology* 124: 38-46.
- Hopp L, McDonnell JJ. 2009. Connectivity at the hillslope scale: Identifying interactions between storm size, bedrock permeability, slope angle and soil depth. *Journal of Hydrology* 376(3-4): 378-391. DOI: 10.1016/j.jhydrol.2009.07.047.
- Hornbaker DJ, Albert R, Albert I, Barabasi A.-L., Schiffer P. 1997. What keeps sandcastles standing? *Nature*, 387, 765.
- Hoshen J, Berry MW, Minser KS. 1997. Percolation and cluster structure parameters: The enhanced Hoshen-Kopelman algorithm. *Physical Review E* 56 (2): 1455-1460.
- Iida T. 1999. A stochastic hydro-geomorphological model for shallow landsliding due to rainstorm. *Catena* 34: 293–313.

- Iorgulescu, I, Jordan JP. 1994. Validation of TOPMODEL on a small Swiss catchment. *Journal of Hydrology* 159 (1-4):255-273. DOI: 10.1016/0022-1694(94)90260-7.
- Iovine G, Di Gregorio S, Lupiano V. 2003. Debris-flow susceptibility assessment through cellular automata modeling: an example from 15–16 December 1999 disaster at Cervinara and San Martino Valle Caudina (Campania, southern Italy). *Nat Hazards Earth Syst Sci* 3:457–468.
- Iverson RM, Reid ME, LaHusen RG. 1997. Debris-flow mobilization from landslides. *Annu. Rev. Earth Planet. Sci.* 25: 85– 138.
- Iverson RM. 2000. Landslide triggering by rain infiltration. *Water Resources Research* 36: 1897-1910.
- Jencso KG, McGlynn BL, Gooseff MN, Wondzell SM, Bencala KE, Marshall LA. 2009. Hydrologic connectivity between landscapes and streams: transferring reach- and plot-scale understanding to the catchment scale. *Water Resources Research* 45: W04428, doi: 10.1029/2008WR007225.
- Jensen JH. 1998. *Self-Organized Criticality*. Cambridge University Press, Cambridge.
- Jordan, JP. 1994. Spatial and temporal variability of stormflow generation processes on a Swiss catchment. *Journal of Hydrology* 153 (1-4): 357-382. DOI: 10.1016/0022-1694(94)90199-6.
- Johnes PJ, Heathwaite AL. 1997. Modelling the impact on water quality of land use change in agricultural catchments. *Hydrol. Processes* 11, 269– 286.
- Keefer DA, Larsen MC. 2007. Assessing landslide hazards. *Science*, 316, 1136–1138.
- Khallili N, Khabbaz MH. 1998. A unique relationship for the determination of the shear strength of unsaturated soils. *Geotechnique* 48(5): 681-687.
- Kirkby M. 1975. Hydrograph modelling strategies, in *Processes in Physical and Human Geography*, edited by R. Peel et al. 69 – 90, Heinemann, London.
- Koutsoyiannis D., Kozonis D., Manetas A. 1998. A mathematical framework for studying rainfall intensity–duration–frequency relationships. *Journal of Hydrology* 206: 118–135.
- Lamb R, Beven KJ, Myrabø S. 1998. Use of spatially distributed water table observations to constrain uncertainty in a rainfall-runoff model. *Advances in Water Resources* 22(4), 305–317.
- Lambe TW, Whitman RV. 1979. *Soil mechanics, SI version*. John Wiley & Sons, Chichester, 553 pp.
- Lane SN, Brookes CJ, Kirkby MJ, Holden J. 2004. A network-index-based version of TOPMODEL for use with high-resolution digital topographic data. *Hydrological Processes* 18, 191–201. DOI: 10.1002/hyp.5208.
- Lane SN, Reaney SM, Heathwaite AL. 2009. Representation of landscape hydrological connectivity using a topographically driven surface flow index. *Water Resource Research* 45. W08423. Doi:10.1029/2008WR007336.
- Lanni C, McDonnell JJ, Rigon R. 2011. On the relative role of upslope and downslope topography for describing water flowpath and storage dynamics: a theoretical analysis. *Hydrological Processes* DOI: 10.1002/hyp.8263.
- Lanni C, McDonnell JJ, Hopp L, Rigon R. 2012. Hydrological controls on shallow landslide triggering: the role of soil depth and bedrock topography. Preliminary accepted for publication in *Earth Surface processes and landforms*.
- Lehmann P, Or D. 2012. Hydro-Mechanical Triggering of Landslides: From Progressive Local

- Failures to Mass Release. *Water Resources Research*, submitted.
- Loague K, Heppner CS, Abrams RH, VanderKwaak JE, Carr AE, Ebel BA. 2005. Further testing of the Integrated Hydrology Model (InHM): event-based simulations for a small rangeland catchment located near Chickasha, Oklahoma. *Hydrological Processes* 19: 1373–1398.
- Loague K, Heppner CS, Mirus BB, Ebel BA, Ran Q, Carr AE, BeVile SH, VanderKwaak JE. 2006. Physics-based hydrologic-response simulation: Foundation for hydroecology and hydrogeomorphology. *Hydrological Processes* 20: 1231–1237.
- Lu N, Godt JW. 2008. Infinite-slope stability under steady unsaturated conditions. *Water Resour. Res.* 44. W11404. doi:10.1029/2008WR006976.
- Lu N, Likos WJ. 2006. Suction stress characteristic curve for unsaturated soil. *J. Geotech. Geoenviron. Eng.* 123: 131–142.
- Malet J-P, Van Asch TWJ, Van Beek R, Maquaire O. 2005. Forecasting the behaviour of complex landslides with a spatially distributed hydrological model. *Natural Hazards and Earth System Science* 5(1): 71-85.
- Matsushi Y, Hattanji T, Matsukura Y. 2006. Mechanisms of shallow landslides on soil-mantled hillslopes with permeable and impermeable bedrocks in the Boso Peninsula, Japan. *Geomorphology* 76: 92–108.
- McDonnell JJ. 1990. A rationale for old water discharge through macropores in a steep, humid catchment. *Water Resour. Res.* 26: 2821–2832.
- McDonnell JJ. 2003. Where does water go when it rains? Moving beyond the variable source area concept of rainfall-runoff response. *Hydrological Processes* 17: 1869–1875. Doi: 10.1002/hyp.5132.
- McDonnell JJ, Sivapalan M, Vache' K, Dunn SM, Grant G, Haggerty R, Hinz C, Hooper R, Kirchner J, Roderick ML, Selker J, Weiler M. 2007. Moving beyond heterogeneity and process complexity: A new vision for watershed hydrology. *Water Resources Research* 43: W07301.
- McGuire KJ, McDonnell JJ, Weiler M, Kendall C, McGlynn BL, Welker JM, Seibert J. 2005. The role of topography on catchment-scale water residence time. *Water Resour. Res.* 41. W05002. Doi:10.1029/2004WR003657.
- McNamara J.P., Chandler D., Seyfried M., Achet S. 2005. Soil moisture states, lateral flow, and streamflow generation in a semi-arid, snowmelt-driven catchment. *Hydrological Processes* 19(20): 4023-4038.
- Merritt WS, Letcher RA, Jakeman AJ. 2003. A review of erosion and sediment transport models. *Environ. Modell. Software* 18: 761 – 799.
- Milledge D, Griffiths D, Lane S, Warburton J. 2012. Limits on the validity of infinite length assumptions for modelling shallow landslides. submitted to *Earth Surface Processes and Landforms*
- Mirus BB, Ebel BA, Loague K, Wemple BC. 2007. Simulated effect of a forest road on near surface hydrologic response. *Earth Surf. Processes Landforms* 32: 126–142. doi:10.1002/esp.1387.
- Mitarai N, Nori F. 2006. Wet granular materials. *Adv. Phys.* 55: 1–45.
- Mitasova H, Hofierka J, Zlocha M, Iverson LR. 1996. Modelling topographic potential for erosion

- and deposition using GIS. *International Journal of Geographical Information Systems* 10(5): 629–641.
- Montgomery, DR, Dietrich, WE. 1994. A physically based model for the topographic control on shallow landsliding. *Water Resour. Res.* 30(4), 1153–1171. DOI: 10.1029/93WR02979.
- Morgenstern NR, de Matos MM. 1975. Stability of slopes in residual soils. In *Proceedings of the 5th Pan-American Conference on Soil Mechanics and Foundation Engineering*, pp. 367–383, A. A. Balkema, Rotterdam, Netherlands.
- Mosley M. 1979. Streamflow generation in a forested watershed, New Zealand. *Water Resour. Res.* 15: 795–806.
- Mualem Y. 1976. A new model for predicting the hydraulic conductivity of unsaturated porous media, *Water Resour. Res.* 12(3): 513–52.
- Munafo M, Cecchi G, Baiocco F, Mancini L. 2005. River pollution from non-point sources: A new simplified method of assessment. *J. Environ. Manage* 77, 93–98.
- Ng CWW, Shi Q. 1998. Influence of rainfall intensity and duration of slope stability in unsaturated soil. *Quarterly Journal of Engineering Geology* 31, 105–113.
- O'Callaghan JF, Mark DM. 1984. The extraction of drainage networks from digital elevation data. *Computer Vision, Graphics, and Image Processing* 28(3), 323–344. DOI: 10.1016/S0734-189X(84)80011-0.
- Ocampo CJ, Sivapalan M, Oldham C. 2006. Hydrological connectivity of upland riparian zones in agricultural catchments: Implications for runoff generation and nitrate transport. *J. Hydrol. Amsterdam* 331, 643–658. doi:10.1016/j.jhydrol.2006.06.010.
- Okimura T, Ichikawa R. 1985. A prediction method for surface failures by movements of infiltrated water in a surface soil layer. *Nat Disaster Sci* 7 :41–51
- O'Loughlin EM. 1986. Prediction of surface saturation zones in natural catchments by topographic analysis. *Water Resources Research* 22, 794–804.
- Olshansky RB. 1990. *Landslide hazard in the united states: case studies in planning and policy development*. Garland Publishing, New York, 176 pp.
- Orlandini, S, Moretti, G. 2009. Determination of surface flow paths from gridded elevation data. *Water Resour. Res.* 45(3). DOI: 10.1029/2008WR007099.
- Orlandini S, Moretti G, Franchini M, Aldighieri B, Testa B. 2003. Path-based methods for the determination of nondispersive drainage directions in grid-based digital elevation models. *Water Resour. Res.* 39(6), 1144. DOI:10.1029/2002WR001639.
- Pack RT, Tarboton DG, Goodwin CN. 1998. The SINMAP approach to terrain stability mapping. In: Moore DP, Hungr O (eds) *Proceedings—international congress of the International Association for Engineering Geology and the Environment* 8, v. 2, A.A. Balkema, Rotterdam, Netherlands, 1157–1165.
- Paniconi C, Troch PA, Van Loon EE, Hilberts A. 2003. Hillslope-storage Boussinesq model for subsurface flow and variable source areas along complex hillslopes: 2. Intercomparison with a three-dimensional Richards equation model. *Water Resources Research* 39(11).
- Pathak S, Nilsen B. 2004. Probabilistic rock slope stability analysis for Himalayan condition. *Bulletin*

- of Engineering Geology and the Environment 63: 25–32.
- Pellenq J, Kalma J, Boulet G, Saulnier G-M, Wooldridge S, Kerr Y, Chehbouni A. 2003. A disaggregation scheme for soil moisture based on topography and soil depth. *Journal of Hydrology* 276, 112–127.
- Pelletier JD, Malamud BD, Blodgett T, Turcotte DL. 1997. Scale-invariance of soil moisture variability and its implications for the frequency-size distribution of landslides. *Engineering Geology* 48(3-4): 255-268.
- Philip JR. 1954. An infiltration equation with physical significance. *Soil Sci.* 77, 153-157.
- Piegari E, Di Maio R, Milano, L. 2009. Characteristic scales in landslide modeling. *Nonlin. Processes Geophys.* 16: 515-523. doi:10.5194/npg-16-515-2009.
- Pradel D, Raad G. 1993. Effect of permeability on surficial stability of homogeneous slopes. *J Geotech Eng ASCE* 119: 315–332.
- Quinn PF, Beven KJ, Chevallier P., Planchon O. 1991. The prediction of hillslope flowpaths for distributed modelling using digital terrain models. *Hydrological Processes* 5, 59– 80.
- Rahardjo H, Chang MF, Lim TT. 1996. Stability of residual soil slopes as affected by rainfalls. In *Proceedings of the 7th International Symposium on Landslides*, vol. 1, edited by K. Senneset, pp. 33– 56, A. A. Balkema, Rotterdam, Netherlands.
- Rahardjo H, Lee TT, Leong EC, Rezaur RB. 2005. Response of a residual soil slope to rainfall. *Canadian Geotechnical Journal* 42(2): 340-351. doi:10.1139/t04-101.
- Rahardjo H, Lim TT, Chang MF, Fredlund DG. 1995. Shear Strength Characteristics of a Residual Soil. *Canadian Geotechnical Journal* 32: 60-77.
- Ray RL, Jacobs JM, de Alba P. 2010. Impacts of Unsaturated Zone Soil Moisture and Groundwater Table on Slope Instability. *Journal of Geotechnical and Geoenvironmental Engineering* 136: 1448-1458.
- Reichenbach P, Guzzetti F, Cardinali M. 1998. Map of sites historically affected by landslides and floods. The AVI Project, 2nd edn. CNRGNDCI Publication Number 2116, map at 1:1200000 scale.
- Reid, SC, Lane SN, Montgomery DR, Brookes CJ. 2007. Does hydrological connectivity improve identification of coarse sediment delivery in upland environments? *Geomorphology* 90: 263–282.
- Richards LA. 1931. Capillary conduction of liquids in porous mediums. *Physics* 1, 318–333.
- Rigon R, Bertoldi G, Over TM. 2006. GEOTop: A distributed hydrological model with coupled water and energy budgets. *Jour. of Hydromet.* 7(3): 371- 388.
- Rodhe A, Seibert J. 1999. Wetland occurrence in relation to topography - a test of topographic indices as moisture indicators. *Agricultural and Forest Meteorology* 98-99: 325-340.
- Rodriguez-Iturbe I, Rinaldo A. 1997. *Fractal River Networks: Chance and Self-Organization*. Cambridge University Press, New York.
- Rosso R, Rulli MC, Vannucchi G. 2006. A physically based model for the hydrologic control on shallow landsliding. *Water Resources Research* 42: W06410. DOI: 10.1029/2005WR004369.
- Rulli MC, Menduni G, Rosso R. 1999. A distributed slope stability model to study shallow landslides initiation in catchment characterized by low permeable soil. paper presented at Symposium on

- River, Coastal and Estuarine Morphodynamics, Int. Assoc. for Hydraul. Res., Genoa, Italy, 9–13 Sept.
- Salvucci GD, Entekabi D. 1994. Explicit expressions for Green-Ampt (Delta function diffusivity) infiltration rate and cumulative storage. *Water Resour Res* 30: 2661–2663.
- Saulnier, GM, Beven K, Obled C. 1997. Including spatially variable effective soil depths in TOPMODEL. *J. Hydrol.* 202: 158–172. doi:10.1016/S0022-1694(97)00059-0.
- Savage WZ, Godt JW, Baum RL. 2004. Modeling time-dependent areal slope stability. In *Landslides: Evaluation and Stabilization*, Lacerda WA, Ehrlich M, Fontoura SAB, Sayao ASF (eds). Taylor and Francis Group: London; 23–36.
- Schuster RL. 1996. Socio-economic significance of landslides. In: Turner, Shuster (eds) “Landslides: investigation and mitigation”. Transportation Research Board – National Research Council, Special Report 247, pp 12–35.
- Scull P, Franklin J, Chadwick OA, McArthur D. 2003. Predictive soil mapping: a review. *Progress in Physical Geography*, 27(2): 171-197.
- Seibert J. 1999. On TOPMODEL’s ability to simulate groundwater level dynamics. In *Regionalization in Hydrology*. Dickkrüger B, Kirkby MJ U. Schröder (eds.). Proc. Conf. at Braunschweig, March 1997. IAHS Publication.
- Seibert J, Bishop KH, Nyberg L. 1997. A test of TOPMODEL's ability to predict spatially distributed groundwater levels. *Hydrological Processes* 11, 1131–1144.
- Seibert J, McGlynn BL. 2007. A new triangular multiple flow-direction algorithm for computing upslope areas from gridded digital elevation models. *Water Resour. Res.* 43. W04501, Doi:10.1029/2006WR005128.
- Selker J, Parlange J-Y, Steenhuis T. 1992. Fingered flow in two dimensions: 2. Predicting finger moisture profile. *Water Resour. Res.* 28(9): 2523–2528. Doi:10.1029/92WR00962.
- Sidle RC, Ochiai H. 2006. *Landslides: processes, prediction, and land use*. American Geophysical Union, Washington DC, 312 pp.
- Sidle RC, Onda Y. 2004. Hydrogeomorphology: overview of an emerging science. *Hydrological Processes*, 18: 597–602. doi: 10.1002/hyp.1360
- Simoni S, Zanotti F, Bertoldi G, Rigon R. 2008. Modelling the probability of occurrence of shallow landslides and channelized debris flows using GEOTop-FS. *Hydrological Processes* 22(4), 532-545.
- Simunek J, van Genuchten MT, Sejna M. 2006. *The HYDRUS Software Package for Simulating Two- and Three-dimensional Movement of Water, Heat, and Multiple Solutes in Variably-Saturated Media: Technical Manual. Version 1.0*. PC-Progress, Prague, Czech Republic.
- Simunek J, van Genuchten MTh, Šejna M. 2008. *The HYDRUS-1D software package for simulating the one-dimensional movement of water, heat, and multiple solutes in variably-saturated media. Version 4.0*. HYDRUS Software Ser. 3. Dep. of Environmental Sciences, Univ. of California, Riverside.
- Skidmore AK, Ryan PJ, Dawes W, Short D, O’Loughlin EM. 1991. Use of an expert system to map

- forest soils from a geographical information system. *International Journal of Geographical Information Science* 5, 431-445.
- Sørensen R, Seibert J. 2007. Effects of DEM resolution on the calculation of topographical indices: TWI and its components. *Journal of Hydrology* 347: 79-89.
- Spearman C. 1904. The proof and measurement of association between two things. *Amer. J. Psychol.* 15:72–101.
- Speight JG. 1980. The role of topography in controlling throughflow generation: A discussion. *Earth Surf. Processes* 5: 187 – 191.
- Spence C. 2010. A Paradigm Shift in Hydrology: Storage Thresholds Across Scales Influence Catchment Runoff Generation. *Geography Compass* 4, 819–833. doi: 10.1111/j.1749-8198.2010.00341.x
- Spence C, Woo Ming-ko. 2003. Hydrology of subarctic Canadian shield: soil-filled valleys. *Journal of Hydrology* 279(1-4):151-166. DOI: 10.1016/S0022-1694(03)00175-6.
- Stieglitz M, Shaman J, McNamara J, Engel V, Shanley J, Kling GW. 2003. An approach to understanding hydrologic connectivity on the hillslope and the implications for nutrient transport. *Global Biogeochemical Cycles* 17(4), 1105. Doi:10.1029/2003GB002041.
- Sudhakar MR. 1996. Role of apparent cohesion in the stability of Dominican allophone soil slopes. *Eng. Geol.* 43:265–279.
- Talebi A, Troch PA, Uijlenhoet R. 2008. A steady-state analytical slope stability model for complex hillslopes. *Hydrol. Processes* 22, 546–553. doi:10.1002/hyp.6881.
- Tarantino A, Tombolato S. 2005. Coupling of hydraulic and mechanical behaviour in unsaturated compacted clay. *Géotechnique* 55(4): 307-317.
- Tarboton DG. 1997. A new method for the determination of flow directions and upslope areas in grid digital elevation models. *Water Resour. Res.* 33(2), 309– 319.
- Terlien MTJ. 1998. The determination of statistical and deterministic hydrological landslide-triggering thresholds. *Environmental Geology* 35(2-3): 124-130.
- Tesfa TK, Tarboton DG, Chandler DG, McNamara JP. 2009. Modeling soil depth from topographic and land cover attributes, *Water Resour. Res.* 45. W10438. doi:10.1029/2008WR007474.
- Tarolli P, Borga M, Chang K-T, Chiang S-H. 2011. Modeling shallow landsliding susceptibility by incorporating heavy rainfall statistical properties. *Geomorphology* 133: 199–211.
- Tarolli P, Borga M, Dalla Fontana G. Analysing the influence of upslope bedrock outcrops on shallow landsliding. 2008. *Geomorphology* 93(3-4): 186-200.
- Tarolli P, Tarboton DG. 2006. A new method for determination of most likely landslide initiation points and the evaluation of digital terrain model scale in terrain stability mapping. *Hydrology and Earth System Sciences* 10, 663–677.
- Terzaghi K. 1943. *Theoretical Soil Mechanics*. John Wiley and Sons, New York.
- Tetzlaff D, Seibert J, McGuire KJ, Laudon H, Burns DA, Dunn SM, Soulsby C. 2009a. How does landscape structure influence catchment transit times across different geomorphic provinces?. *Hydrological Processes* 23: 945 – 953.
- Tetzlaff D, Seibert J, Soulsby C. 2009b, Inter-catchment comparison to assess the influence of

- topography and soils on catchment transit times in a geomorphic province; the Cairngorm mountains, Scotland. *Hydrological Processes* 23, 1874–1886. Doi: 10.1002/hyp.7318
- Tetzlaff D, Soulsby C, Waldron S, Malcolm IA, Bacon PJ, Dunn SM, Lilly A, Youngson AF. 2007. Conceptualization of runoff processes using a geographical information system and tracers in a nested mesoscale catchment. *Hydrological Processes* 21: 1289–1307. Doi: 10.1002/hyp.6309.
- Thompson JA, Bell JC, Butler CA, 2001. Digital elevation model resolution: effects on terrain attribute calculation and quantitative soil-landscape modelling. *Geoderma* 100(1-2), 67-89.
- Torres R, Dietrich WE, Montgomery DR, Anderson SP, Loague KM. 1998. Unsaturated zone processes and the hydrologic response of a steep, unchanneled catchment. *Water Resources Research* 34(8): 1865–1879.
- Troch PA, Paniconi C, Van Loon EE. 2003. Hillslope-storage Boussinesq model for subsurface flow and variable source areas along complex hillslopes: 1. Formulation and characteristic response. *Water Resources Research* 39(11): 1316.
- Troch P, van Loon E, Hilberts A. 2002. Analytical solutions to a hillslope-storage kinematic wave equation for subsurface flow, *Adv. Water Resour.* 25: 637– 649.
- Tromp-van Meerveld HJ, Peters NE, McDonnell JJ. 2007. Effect of bedrock permeability on subsurface stormflow and the water balance of a trenched hillslope at the Panola Mountain Research Watershed, Georgia, USA. *Hydrological Processes* 21: 750–769.
- Tromp van Meerveld I, McDonnell JJ. 2005. Comment to “Spatial correlation of soil moisture in small catchments and its relationship to dominant spatial hydrological processes, *Journal of Hydrology* 286: 113 134”. *Journal of Hydrology* 303 (1-4): 307-312.
- Tromp-vanMeerveld HJ, McDonnell JJ, 2006a. Threshold relations in subsurface stormflow: 1. A 147-storm analysis of the Panola hillslope. *Water Resour. Res.* 42, W02410, doi:10.1029/2004WR003778.
- Tromp-van Meerveld HJ, McDonnell JJ. 2006b. Threshold relations in subsurface stormflow: 2. The fill and spill hypothesis. *Water Resources Research* 42. W02411. doi:10.1029/2004WR003800.
- Tsuboyama Y, Sidle RC, Noguchi S, Hosoda I. 1994. Flow and solute transport through the soil matrix and macropores of a hillslope segment. *Water Resour. Res.* 30: 879– 890.
- Turcotte DL, Malamud BD, Guzzetti F, Reichenbach P. 2002. Self-organization, the cascade model, and natural hazards. *Proc Natl Acad Sci USA* 19:2530–2537.
- Turton DJ, Haan CT, Miller EL. 1992. Subsurface flow response of a small forested catchment in the Ouachita mountains. *Hydrol. Processes* 6: 111 – 125.
- Uchida T, Tromp-van Meerveld I, McDonnell JJ. 2005. The role of lateral pipe flow in hillslope runoff response: an intercomparison of non-linear hillslope response. *Journal of Hydrology* 311: 117-133.
- Van Asch ThWJ, Buma J, Van Beek LH. 1999. A view on some hydrological triggering systems in landslides. *Geomorphology* 30 (25–32).
- Van Asch ThWJ, Hendriks MR, Hessel R, Rappange FE. 1996. Hydrological triggering conditions of landslides in varved clays in the French Alps. *Eng. Geol.* 42: 239–251.
- Vanacker, V., Vanderschaeghe, M., Govers, G., Willems, E., Poesen, J., Deckers, J., De Bievère, B.,

2003. Linking hydrological, infinite slope stability and land-use change models through GIS for assessing the impact of deforestation on slope stability in high Andean watersheds. *Geomorphology*, 52: 299–315.
- Vanapalli SK, Fredlund DG, Pufahl DE, Clifton AW. 1996. Model for the prediction of shear strength with respect to soil suction. *Canadian Geotechnical Journal*. 33(3): 379-392. DOI:10.1139/t96-060.
- Van Beek R. 2002. Assessment of the influence of changes in climate and land use on landslide activity in a Mediterranean environment. *Netherlands Geographical Studies* no. 294, KNAG, Faculty of Geosciences, Utrecht University, p 366
- VanderKwaak JE. 1999. Numerical simulation of flow and chemical transport in integrated surface-subsurface hydrologic systems. PhD dissertation, University of Waterloo, Ontario, Canada.
- van Genuchten MT. 1980. A closed-form equation for predicting the hydraulic conductivity of unsaturated soils. *Soil Science Society of America Journal* 44, 892–898.
- Van Nieuwenhuysen BHJ, Michael A, Wyseure G, Govers G. 2011. Pattern-process relationships in surface hydrology: hydrological connectivity expressed in landscape metrics. *Hydrological Processes* 25: 3760–3773.
- Van Westen CJ. 2000. The modelling of landslide hazards using GIS. *Surveys in Geophysics* 21: 241-155.
- Varnes DJ. 1978. Slope movement types and process. In: R.L. Schuster and R.J. Krizek (Editors), *Landslides: Analysis and Control-Transportation Research Board, Special Report*. National Research Council, Washington D.C., pp. 11–33.
- Verburg PH, Soepboer W, Veldkamp A, Limpiada R, Espaldon V, Mastura SSA. 2002. Modeling the spatial dynamics of regional land use: the CLUE-S model. *Environmental Management* 30(3): 391–405.
- Vilar OM. 2006. A simplified procedure to estimate the shear strength envelope of unsaturated soils. *Canadian Geotechnical Journal* 43(10): 1088-1095.
- Weiler M, McDonnell JJ. 2004. Virtual experiments: a new approach for improving process conceptualization in hillslope hydrology. *Journal of Hydrology* 285: 3–18.
- Weiler M, McDonnell JJ, Tromp-van Meerveld I, Uchida T. 2005. *Subsurface stormflow*, Encyclopedia of Hydrological Sciences, Wiley and Sons.
- Western AW, Grayson RB, Blöschl G, Willgoose GR, McMahon TA. 1999. Observed spatial organization of soil moisture and its relation to terrain indices. *Water Resour. Res.* 35(3). DOI: 10.1029/1998WR900065.
- Western, AW, Blöschl G, Grayson RB. 2001. Toward capturing hydrologically significant connectivity in spatial patterns. *Water Resour. Res.* 37, 83-97. doi:10.1029/2000WR900241.
- Western AW, Zhou SL, Grayson RB, McMahon TA, Blöschl G, Wilson DJ, 2004. Spatial correlation of soil moisture in small catchments and its relationship to dominant spatial hydrological processes. *Journal of Hydrology* 286 (1-4): 113-134. Doi: 10.1016/j.jhydrol.2003.09.014.
- Western AW, Zhou S, Grayson RB, McMahon T, Blöschl G, Wilson DJ. 2005. Reply to comment by Tromp van Meerveld and McDonnell on Spatial correlation of soil moisture in small catchments

- and its relationship to dominant spatial hydrological processes. *J. Hydrol.* 303, 313 -315. doi:10.1016/j.jhydrol.2004.09.001.
- Weyman DR. 1973. Measurements of the downslope flow of water in a soil. *Journal of Hydrology* 20(3):267-288. DOI: 10.1016/0022-1694(73)90065-6.
- Weyman DR. 1974. Runoff processes, contributing area and streamflow in a small upland catchment. In *Fluvial Processes in Instrumented Watersheds*, GregoryKJ, WallingDE (eds). Institute of British Geographers: London; 33–43.
- Wieczorek GF, Glade T. 2005. Climatic factors influencing occurrence of debris flows. In: *Debris flow hazards and related phenomena* (Jakob M, Hungr O, eds). Berlin Heidelberg: Springer, pp 325–362.
- Wilson RC, Wieczorek GF. 1995. Rainfall thresholds for the initiation of debris flows at La Honda, California, *Environ. Eng. Geosci.* 1: 11– 27.
- Wolle MC, Hachich W. 1989. Rain-induced landslides in southeastern Brazil. *12th Int. Conf. on Soil Mech. and Found. Eng.*. Balkema, Rio de Janeiro, Brasil, pp. 1639– 1642.
- Wolock, DM, Price CV. 1994. Effects of digital elevation model map scale and data resolution on a topography-based watershed model. *Water Resour. Res.* 30 (11). Doi: 10.1029/94WR01971.
- Woods R, Rowe L. 1996. The changing spatial variability of subsurface flow across a hillside. *J. Hydrol.* 35: 51–86.
- Wu W, Sidle R. 1995. A distributed slope stability model for steep forested basins. *Water Resources Research* 31, 2097– 2110.